JGERI
Journal of Green Energy Research and Innovation
ISSN: 3041-9018

Journal of Green Energy Research and Innovation

Volume 1, Issue 2, Spring 2024

PUBLISHER
Arak University

Journal of Green Energy Research and Innovation (JGERI)

Publisher: **Arak University**

Director-in-Charge: **Dr. Ali Asghar Ghadimi**

Editor-in-Chief: **Prof. Gevork B. Gharehpetian**

Deputy Editor: **Dr. Abolghasem Daeichian**

Executive Editor**: Dr. Mahyar Abasi**

Coverage area: **International**

Journal Type: **Scientific and technical**

Language: **English**

Frequency: **Quarterly**

Review Time: **4-8 Weeks**

Publication Type: **Electronic, Print**

Open Access: **Yes**

Licensed by: **CC BY-NC 4.0**

Policy: **Peer-Reviewed**

DOI**: 10.61186/jgeri**

E-mails: **jgeri@araku.ac.ir**

Website: **https://jgeri.araku.ac.ir/**

Address: **Department of Electrical Engineering, Faculty of Engineering, Arak University, Arak, Iran.**

P.O. Box: **38156-8-8349**

Tel: **086-32625099**

Editorial Board

About Journal

JGERI is interested in the results of research in the field of green and renewable energies. The scope of publications of this journal in the field of green energy is extensive and it welcomes novel and innovative studies. Due to the increasing influence of renewable energy in power systems, studies, research, and reports resulting from scientific achievements in this specific area have risen compared to previous decades. This journal is ready to publish specialized articles in all fields related to green energy and interdisciplinary topics related to this scientific branch in the form of open access, which is published annually in four issues as free and open access by Arak University, Iran. **JGERI** is ready to receive the latest research results ranging from analytical methods, numerical simulation, experimental research, and development studies concerning the knowledge and application of green energy.

The following articles are acceptable:

- **Research articles** are expected to present innovative solutions, new concepts, or creative ideas that can help solve existing or emerging technical challenges in the field of green and renewable energy.
- **Review articles** are expected to provide enlightening and specialized reviews, trainings, or case studies on an important topic, timely and widely in the field of green and renewable energies.
- **Applied articles** are expected to share the results of the industry's valuable experiences in dealing with challenging technical issues, developing/adopting new standards, applying new technologies or solving complex problems in the field of green and renewable energies. These articles can have a significant impact on the strategic plans of the industry in the coming years.

Aims and Scope

JGERI is interested on the qualified international multidisciplinary research results related to all aspects of green energy. The scope of **JGERI** is very broad, and welcomes original, novel fundamental and engineering research. We also publish reviews and industrial reports of green energy and its impact on the eco-environment.

We welcome research papers that focus on, but are not limited to, the following areas:

- Policies and Strategies for Green Energy Systems
- Fundamental And Industrial Applications for Green Energy Systems
- Energy Conversion, Control Techniques, and Grid Interactive Systems for Green Energy Systems
- Environmental Impacts of Energy Technologies and Pollution Control
- Materials And Catalysis for Green Energy Systems
- Green Energy Consumption
- Artificial Intelligence, Machine Learning, and Computational Methods in Green Energy Systems
- Public Awareness and Education for Green Energy Systems
- Solar Energy and Photovoltaic
- Wind Energy
- Hydrogen Energy and Energy Storage
- Biofuel and Bioenergy

Each manuscript will go through a rigors peer-review process. you can visit our Instructions for Authors page for information on preparing your manuscript.

Guide for Authors

1. Important points and rules for manuscript submission and publication

-Submitting a manuscript to a journal means that the manuscript is not under review or has not been published anywhere in any other language before.
-The submission of the manuscript for publication by the author, implicitly or explicitly, implies the approval of the organization or body where the author works and has used its affiliation.
-By submitting the manuscript, all authors officially declare their agreement to grant the copyright of the manuscript in case of acceptance to Arak University and **JGERI**. However, the authors are responsible for all the contents published in the manuscript, and the journal is only a reviewer and publisher.
- All authors are required to declare any actual or potential conflicts of interest, including financial, personal, or relationships with individuals or organizations that could affect their work.
- Each of the authors must declare their contribution and role in the manuscript on the Title Page to the journal. The statement of approval of all authors and their role in the manuscript is the responsibility of the corresponding author.
- Authors should note that all manuscripts sent to **JGERI** are checked with Authenticate's CrossCheck software to analyze the authenticity of the content. In this analysis, the overlap and similar texts presented in the submitted manuscripts will be determined.
- **JGERI** makes its manuscripts open to access after publication and there is no charge (APC) for reviewing and publication of manuscripts, and readers can download and use the articles for free.
- All authors, if they had financial support in conducting research related to this manuscript, should briefly state their role. If financial source(s) have no role in the results of the research published by the article, this should also be mentioned by the authors.
- Acknowledgments to individuals and institutions can be mentioned in a separate section at the end of the manuscript before References, and they must not be included as footnotes or in any other form. In this section, it is recommended to mention the names of those who have collaborated during the research (such as those helping in the language correctness aspect of the manuscript, assisting in writing the manuscript or proofreading it, and other cases).
- Non-commercial use of the manuscript will be governed by the Creative Commons Attribution-NonCommercial 4.0 International License, which is currently available at the link (https://creativecommons.org/licenses/by-nc/4.0/). This certificate allows others to use the authors' work in a non-commercial way and utilize it in their research work, although in the new work, they need to acknowledge the authors and mention its non-commercial nature.

2. Initial submission of the manuscript

Submission to this journal is online and you will be accompanied in all the steps of creating a user account and uploading files. All correspondence, including notification of the editor's decision and request for revision, will be made via email. To submit your manuscript, just click on the **Submit Manuscript** option on the journal page. Then, click on **Register** to create an author account. A message will be sent to your email containing your username and password. Then, log in to the manuscript submission system on the Users login page, where you need to enter the username and password and submit your new manuscript. Once you are logged in, you can change your password by clicking on My Home in the top menu. For the next time, just log in to your account. Please include the names, addresses, and email addresses of at least three potential academic reviewers with the paper. Please include reviewers' names and their academic rank, affiliation, and contact information (mail address is mandatory). However, only the editor has the right to decide on the use of suggested reviewers. All the submitted manuscripts undergo the process of plagiarism check with IThenticate software and the review process begins. According to the journal policy, there is a difference between the requirements for initial and revised submission files. Required files for initial submission include three files: **JGERI_Main_Manuscript**, **JGERI_Form_for_Copyright_Transfer_Statement and Conflict_ of_ Interest_ Disclosure** and **JGERI_Cover_Letter**, all three of which must be sent to the journal in PDF format. You can use the links below to download the requirements and suggestions files of these three files.

- JGERI_Guideline_for_Main_Manuscript
- JGERI_Guideline_for_Cover_Letter
- JGERI_Form_for_Copyright_Transfer_Statement and Conflict_ of_ Interest_ Disclosure

3. Submission of the revised manuscript

If the submitted manuscript, after going through the initial review process, is evaluated by the officials and reviewers of the journal and a decision is made to make corrections and revisions in the form of minor or major, the authors are obliged to make the corrections and prepare the response letter to the reviewers within the time specified by the journal. Three files must be sent to the journal at this stage: WORD and PDF files of the revised manuscript (changes should be highlighted), PDF file of the response to the reviewers (including the comments and responses of each of the reviewers separately), Title Page and Authorship file in WORD format (containing two main forms: Title Page and Authorship). The link to download the necessary files along with their requirements and instructions is given below. Points raised in the file **JGERI_Revised_Manuscript** must be followed for compiling the revised manuscript. The authors are obliged to submit the revised file in PDF and WORD format to the journal. Also, different parts of the file **JGERI_Form_for_Title_Page_ and_ Authorship** needs to be completed and signed by the corresponding author, but **JGERI_Response_to_the_Reviewers_Comments** is suggested by the journal and it is not necessary to follow all the points of that file. It should be noted that all the stages of page layout and editing in the form of final publication are the responsibility of the journal. In the completion stages of this process, the cooperation of the authors is needed, and we will inform you at each stage. Thus, the minimum requirements for file compilation are provided in the template file.

- JGERI_Guideline_for_Revised_Manuscript
- JGERI_Form_for_Title_Page_ and_ Authorship
- JGERI_Guideline_for_Response_to_the_Reviewers_Comments

4. **After the final acceptance of the manuscript**

After announcing the final acceptance of the manuscript (reviews may happen several times), the files **JGERI_Revised_Manuscript** and **JGERI_Form_for_Title_Page_ and_ Authorship** will be sent to the paging unit for page layout and final editing. After the final acceptance announcement, the authors will be asked to send a graphic abstract included in a single file. Then, the process of compilation of the manuscript will be completed by the journal and finally, the proof version of the manuscript will be sent to the authors. The authors are obliged to check the proof file completely and report to the journal if they find any ambiguity or error in the final file. In some cases, along with the final proof file of the manuscript, there may be a series of errors and ambiguities in the manuscript, which are sent to the author in the form of comments along with the proof version of the manuscript. The corresponding author is obliged to clarify and resolve these problems and ambiguities in the specified time.

5. **After publication on the journal's website**

After announcing the initial acceptance, the information of the article without its content will be indexed in the Articles in the Press section of the website. After including the article in the issue selected by the journal, the desired article will be indexed in the Current Issue unit along with Vol, No, and pp. Also, the electronic file of the article can be introduced in all scientific references through the DOI link. The important point is that, after acceptance and indexing, the names of the authors cannot be changed, that is, it will not be possible to add, delete, or change the order of the names of the authors and their organizational affiliations.

Cooperative Publication Organization

Renewable Energy Research Institute of Arak University
http://araku.ac.ir/web/riren

Iranian Wind Energy Association
https://www.irwea.org/fa/

Indexing Databases and Social Networks

Google Scholar: https://scholar.google.com/citations?user=47bsJFoAAAAJ&hl=en

Linkedin: https://www.linkedin.com/in/jgeri-arak-university-0818872b9

Academia:https://independent.academia.edu/JournalofGreenEnergyResearchandInnovationJGERI

PaperHive: https://paperhive.org/users/jgeri

GrowKudos: https://www.growkudos.com/profile/j._green_energy_res._innov._jgeri

MyScineceWork: https://www.mysciencework.com/profile/j.green.energy.res.innov.jgeri

SciExplore: https://sciexplore.ir/profiles/author/987-081-740

Magiran: https://www.magiran.com/magazine/8484

Contents

Journal of Green Energy Research and Innovation

Percentage of Islanding and Peninsulating Detection in Large Microgrids with Renewable Energy Resources with Multiple Connection Points to Different Grids

Saman Darvish Kermani, Mohammad Fayazi, Jamshid Barati, Mahmood Joorabian

Highlight

- Presenting a new method for islanding and peninsulating detection in large microgrids
- Presenting of two concepts "percentage of islanding" and "peninsulating" in the study of islanding issues
- Considering the impact of renewable energy resources in the presented islanding detection method
- High usability of the proposed method due to the simplicity of its algorithm

Graphical Abstract

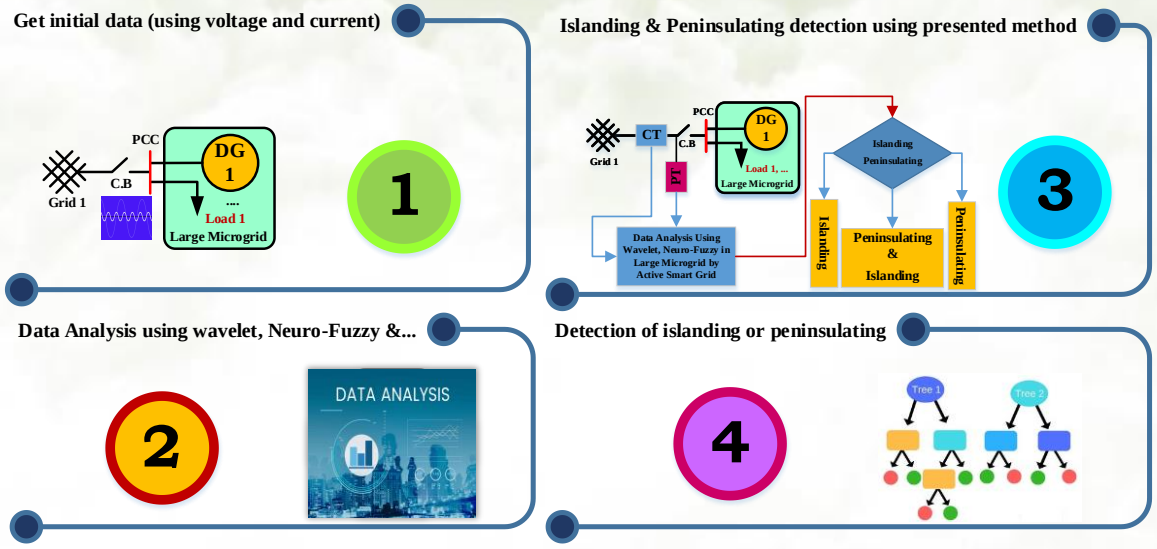

Use your device to scan and read the article online

Citation

S. Darvish Kermani, M. Fayazi, J. Barati, and M. Joorabian, "Percentage of Islanding and Peninsulating Detection in Large Microgrids with Renewable Energy Resources with Multiple Connection Points to Different Grids," *Journal of Green Energy Research and Innovation*, vol. 1, no. 2, pp. 1-14, 2024.

https://doi.org/10.61186/jgeri.1.2.1

Online ISSN: 3041-9018

Journal of Green Energy Research and Innovation

Journal Homepage: www.jgeri.araku.ac.ir

Percentage of Islanding and Peninsulating Detection in Large Microgrids with Renewable Energy Resources with Multiple Connection Points to Different Grids

Saman Darvish Kermani [1], Mohammad Fayazi [2], Jamshid Barati [3], Mahmood Joorabian[4,*]

[1] *GHD Advisory, Melbourne VIC 3000, Australia.*
[2] *Dam and power plant department, Khuzestan Water and Power Authority (KWPA), Ahvaz 61348-13956, Iran.*
[3] *Department of Electrical Engineering, Ramhormoz Branch, Islamic Azad University, Ramhormoz, Iran.*
[4] *Department of Electrical Engineering, Faculty of Engineering, Shahid Chamran University of Ahvaz, Ahvaz, Iran.*

* ***Corresponding Author:*** *mjoorabian@scu.ac.ir*

ARTICLE INFO

Keywords:
Islanding,
Peninsulating,
Microgrid,
Smart grid,
Distributed generation.

Article history:
Received: 14 December 2023;
Revised: 28 January 2024;
Accepted: 07 March 2024;

Article type:
Research Article

ABSTRACT

This paper presents the islanding and peninsulating of distributed generators (DGs), such as wind and solar power plants, that feed microgrid systems. However, the paper does not focus on just an ordinary microgrid but large microgrids that have several sub-microgrids with renewable energy resources and multiple connection points (MCPs) to different grids. When islanding happens, the main microgrid disconnects some connection points from grids whereas some connection points to other grids could be connected and divided into some sub-microgrids for better stability. Two new definitions are proposed for large microgrid islanding: percentage of islanding and peninsulating. The former means how much it is possible that an islanding happens before it happens, and the latter means that: "after separating from some connection points to grids in a large microgrid with MCPs to different grids, remained large microgrid network is an island or a peninsula that is connected in some connection points to other grids? So, peninsulating a large microgrid depends on the number of connection points, at least two points, to different grids. This paper describes these two new definitions. The method involves the measurement of utility currents, voltages, and other signals through a bidirectional communications system in smart grids. These signals are used to calculate the percentage of islanding and decide on microgrid islanding or peninsulating.

1. Introduction

Nowadays, distributed generation (DG), solar, and wind units are growingly used in power networks as a means to satisfy the rising electricity demand and encourage the use of renewable energy sources. The higher penetration of DG amplifies the complexity of the distribution system and gives rise to multiple challenges. Presently, load demand has increased the number and variety of microgrids, resulting in the development of larger regroup systems. Large microgrids, which have several sub-microgrids with multiple connection points (MCPs) to different grids, are one of the system complexities. Islanding

is one of the most significant challenges in these systems. It refers to a situation where a section of the distribution system consists of DG and local loads. During islanding, these loads stay powered even though they are mistakenly disconnected from the rest of the system. The isolation may be attributed to a fault event on the primary distribution feeder. The re-closer will, in this situation, restore the connection to the isolated section of the system after a specific period, as determined by the system operator. This phenomenon is undesirable as it can be harmful to the distribution system. Therefore, the identification of islanding (also known as anti-islanding) has become a crucial necessity for protecting DG systems.

When islanding happens in a large microgrid with some sub-microgrids equipped with MCPs to different grids, the main microgrid separates from some connection points to grids whereas some connection points to other grids could be connected and divided to some sub-microgrids for better stability. This new state is not islanding because the microgrid is connected to other grids, so this new state is named "peninsulating" in this paper. After separating from some connection points to grids in a large microgrid with MCPs to different grids, the remaining large microgrid network constitutes an island or a peninsula connected in some connection points to other grids. So, peninsulating a large microgrid depends on the number of connection points, necessarily at least two points, to different grids. Islanding often occurs when the power generated by the DGs matches the power used by the load, resulting in the load being completely supplied by the DGs. Currently, if there is a disruption or failure in the utility, the fluctuations in voltage and frequency of the DGs cannot be identified according to the standards of UL1741 or IEEE1547 [1, 2]. This paper addresses large microgrids with some sub-microgrids, which are very complicated. In brief, if a microgrid connects to two grids and disconnects from one of them, it will be peninsulating not islanding because the microgrid connects to another grid. If the microgrid connected to two grids disconnects completely from the two grids, islanding may happen. An imminent and significant problem lies in the full assimilation of wind and solar power generation units into electric power systems, particularly within distribution networks operating at medium and low voltage levels. Indeed, such integration would enable optimal utilization of the renewable sources (RS) present in the area, which would otherwise remain untapped. This necessitates a comprehensive reconsideration of the administration and regulation of energy networks, transitioning from passive systems to innovative and dynamic "smart grids" [3]. The current passive systems are distinguished by one-way energy flows and a restricted range of intelligent and automated functions. In contrast, the concept of the smart grid involves energy flows that move in both directions. To support this, smart metering technologies and capabilities are required, along with a bidirectional communication system and various intelligent field devices. These devices enable monitoring, automation, protection, and control actions [4]. This technology involves the utilization of a bidirectional communication system in smart grids to measure utility currents, voltages, and other signals. These signals are used for islanding or peninsulating. The central microgrid decision system determines the islanding or peninsulating state, as well as other possible

states, by measuring currents, voltages, and other signals at the point before the main circuit breaker instead of the point of common coupling (PCC), as explained in reference [5]. There are abundant renewable energy resources (RESs) available on islands, such as wind, sun, biomass, ocean current energy, wave energy, tidal energy, ocean thermal energy, ocean salinity gradient energy, and geothermal energy. These resources have the potential to greatly contribute to developing electricity on islands [3]. Nowadays, microgrids are more complicated than before and some of these RESs in a microgrid connected to some grids can create a large microgrid. Nevertheless, the output power of these DGs can vary significantly and prove challenging to regulate due to factors such as weather conditions, geographical location, and other variables, which contribute to their intermittent and unpredictable nature. In recent years, microgrid technology has emerged as a promising solution for addressing the intermittent issues associated with the integration of distributed generators [6, 7]. This technology offers decentralization and localization, allowing for the maximum utilization of distributed energy resources to enhance system stability and reliability, improve power quality, reduce transmission losses, and enable intelligent and flexible control. A large microgrid with MCPs to different grids can be very complicated. Besides all these points, such microgrids need to be subjected to further research. The literature offers several ways for the detection of islanding, which can be categorized into passive, active, and communications-based techniques [4-21]. Ref. [22] presented a real-time analysis of an islanding detection scheme for AC microgrids, and Ref. [23] presented a communication-less islanding detection scheme for hybrid distributed generation systems using recurrent neural networks. Ref. [15] presented another classification for island detection methods, which includes local and remote methods. Active and passive methods are subsets of local methods. Ref. [19] proposed a passive islanding detection scheme using a phase angle of positive sequence voltage. Communications-based solutions encompass a wide range of communication technologies that can be utilized to establish smart grid infrastructures. Each technology possesses its distinct advantages and disadvantages [2, 15, 17, 18, 20, 24]. Hybrid techniques have a small Non-Detection Zone (NDZ) and perturbation is introduced only when islanding is suspected [19]. Large microgrids have complicated and hybrid techniques in which small NDZ should be used. This paper suggests hybrid techniques for the detection of not only islanding but also peninsulating. In addition to the tiny NDZ, the detection time is crucial. Therefore, this paper employs the percentage of islanding and/or peninsulating, as well as a modification in the measurement point of signals from the PCC in conventional approaches, to occur before the primary circuit breaker.

The paper is composed of the following sections. Section 2 presents the proposed islanding and/or peninsulating detection method. Sections 3 and 4 discuss the islanding detection methods and the percentage of islanding, respectively. The concept of peninsulating is presented in Section 5. Sections 6 and 7 describe large microgrids' formulation and an example of a large microgrid, respectively. The paper comes to an end with some concluding points in Section 8.

2. The Proposed Islanding and/or Peninsulating Detection Method

When a defect occurs in a power network, it is necessary to promptly identify and isolate the fault location in the power system using a circuit breaker. The duration required for fault clearing is equal to the combined time taken for the relay to operate and for the circuit breaker to interrupt the fault current. Even in the immediate operating mode of a relay, it takes around 0.5 to 1 cycle to transmit the open signal to the circuit breaker. The operational duration of a circuit breaker is determined by the number of times it has been activated and its specific kind, typically falling within a range of 3 to 5 cycles. This study focuses on measuring the utility current, voltage, and other signals on the side of the utility circuit breaker connected to DGs. Hence, the detection time for islanding is unaffected by the duration of the circuit breaker operation. By eliminating the circuit breaker operation time, the detection of the islanding state is expedited compared to local approaches. Figure 1 displays the suggested location for the measuring point.

The identification of islanding situations in the local technique commences upon the disconnection or opening of the circuit breaker. The local approach is used to measure system parameters, such as voltage, current, and frequency. The occurrence of islanding is recognized by sensing these variations after it occurs. Islanding situations can be detected by relocating the measuring point from the PCC to a position after the utility circuit breaker, prior to its opening. The suggested method utilizes wavelet transform in a neuro-fuzzy network to detect islanding and/or peninsulating. The suggested approach successfully reduces the islanding detection time. The basic model of the hybrid islanding and/or peninsulating detection method proposed in this paper is illustrated in Figure 1. The transient waveforms of currents, voltages, and other signals in a power network include distinct characteristics that can be used to identify the underlying source of the transient occurrence. The proposed method for detecting islanding and/or peninsulating occurrences is based on the assumption that the transients produced during these events possess a distinct characteristic. By developing a classifier, it is possible to differentiate islanding and/or peninsulating events from other disruptions.

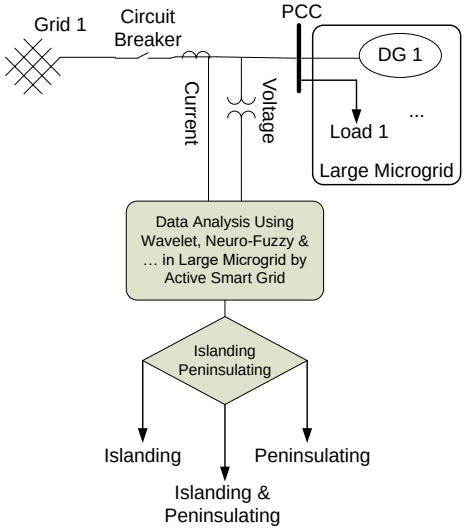

Figure 1. The location of current and voltage measuring point in the proposed model using the transient-based islanding detection method.

In this paper, NDZ is eliminated by identifying the conditions that lead to islanding and/or peninsulating through wavelet transform analysis before the circuit breaker opens. NDZ is created as a result of the disparity between active and reactive power during the occurrence of islanding and/or peninsulating in the local method. The proposed method does not experience any power quality issues as there is no insertion of disturbances. Thus, this strategy is devoid of the issues present in both passive and active procedures. So, a hybrid method is suggested which can detect disturbances and decide on an islanding and/or peninsulating state.

3. Islanding Detection Methods

Several methodologies have been devised to identify the occurrence of islanding. The strategies can be categorized into central (remote), local, and hybrid techniques, as depicted in Figure 2. The boxes in Figure 2 show some methods. These methods are used not only for islanding detection but also for peninsulating detection in this paper. Peninsulating is a decision made by a central smart microgrid unit. So, various combinations of remote and local (passive and active) methods are used for this decision in different microgrids based on their conditions.

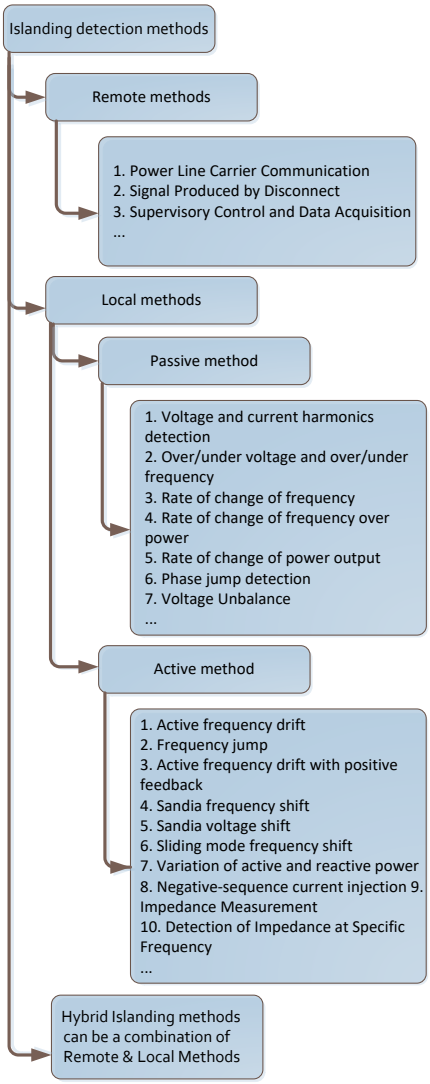

Figure 2. The classification of islanding detection methods.

4. Percentage of Islanding

This paper uses "percentage of islanding" in a new definition. It is the answer to this question, "Before islanding, how much is it possible for islanding to happen?"

For example, a failed network happens and some voltages and current characteristics are changed such that calculation in the central smart microgrid unit shows that this state will probably be islanding, so the active detection method starts to work with amplitude current proportion to probably calculation (for example in increasing current amplitude active method). Beforehand, the active detection method did not work, and this method can be useful for power quality in microgrids. If the calculation in the central smart microgrid unit shows that the probability of islanding is increased, the current amplitude will increase. This method influences power quality in a short time and if islanding does not happen in a definite time, the current amplitude will gently decrease to zero and only other detection methods like passive and remote detection methods will work in the microgrid. In brief, the percentage of islanding is a method for conditionally using active methods combined with passive and remote methods. The percentage of islanding is used for peninsulating, too. The central smart microgrid unit decides that a large microgrid should separate from some connection points to grids and the remaining large microgrid network is an island or a peninsula. So, the percentage of islanding is a general concept for explaining the probability of the shift from normal to island and/or peninsula state in a large microgrid.

5. Peninsulating

An island refers to a landmass that is smaller than a continent and is surrounded by water. A peninsula is a landmass that is surrounded by water on three sides and is attached to a larger landmass. A microgrid without any connection to other grids is an island, but a microgrid that is connected to other grids can be named a peninsula. This paper uses "peninsulating" in a new definition. In a large microgrid with MCPs to different grids, if a failure happens after separating from some connection points, the remaining large microgrid network will be an island or a peninsula connected in some connection points to other grids. Peninsulating a large microgrid depends on the number of connection points to different grids, which should be at least two connection points. A microgrid in normal condition with a connection point to a grid is a peninsula itself.

5.1. Concept of Islanding and Peninsulating in Large Microgrids

The concept of islanding in large microgrids with MCPs to different grids differs from islanding in microgrids. A large microgrid can be a microgrid that is connected to different grids. Figure 3 displays a power island after islanding. In this figure, breaker B1 separates the microgrid from the main grid, so this state is islanding. A large microgrid is illustrated in Figure 4 with two connection points to different grids via two main breakers (B1 and B3). When these two breakers (B1 and B3) separate a large microgrid from these two grids (grid 1 and grid 2), islanding happens again, but all main grids should separate from a large microgrid which can be an islanding state.

Figure 5 depicts a large microgrid with two connection points to different grids via two main breakers (B1 and B3). When breaker B1 separates main grid 1 from a large microgrid, peninsulating happens. If grid 1 and grid 2 connect via breakers B1 and B3 shown in Figure 6, peninsulating will occur again. So, a normal state in a large microgrid with different points to grids can be a peninsula.

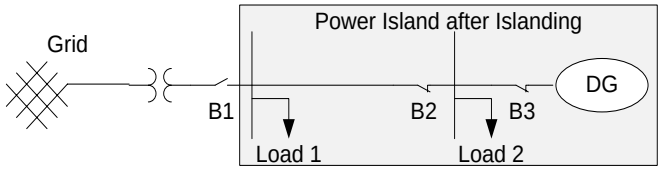

Figure 3. Islanding a microgrid with a main breaker (B1).

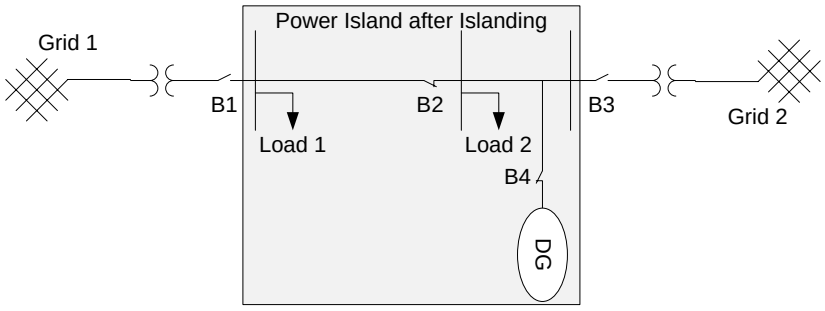

Figure 4. Islanding a large microgrid with two connections points to different grids via two main breakers (B1 and B3).

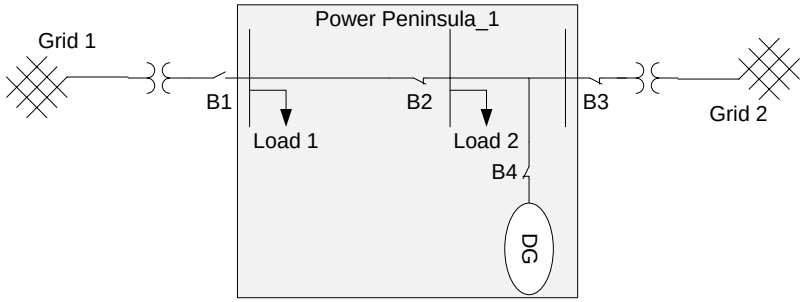

Figure 5. Peninsulating a large microgrid with two connections points to different grids via two main breakers (B1 and B3). Breaker B1 separates main grid 1 but, grid 2 is connected via Breaker B3.

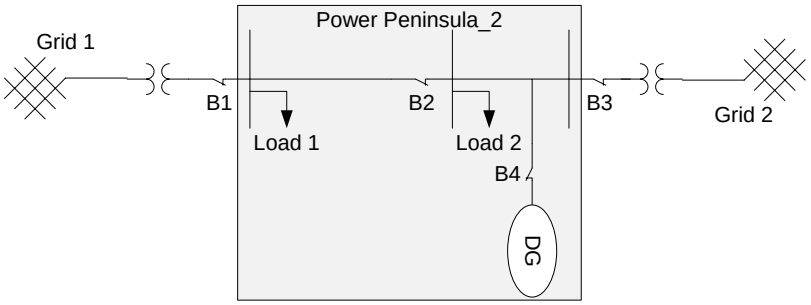

Figure 6. Peninsulating a large microgrid with two connections points to different grids via two main breakers (B1 and B3). Grid 1 and grid 2 are connected via breakers (B1 & B3).

5.2. Power Island and Peninsula in Large Microgrids

A power peninsula is illustrated in Figure 7 with two connection points to different grids via two main breakers (B1 and B3). When breaker B2 separates two DGs from each other, as shown in Figure 8, a large microgrid changes to two power peninsulas because one of them is connected to grid 1 via breaker B1 and the other is connected to grid 2 via breaker B3 and these are not power islands. Another state is illustrated in Figure 9. Grid 1 is connected via breaker B1, and grid 2 is separated via breaker B3. So, one of them is a power peninsula and the other one is a power island. Another state is illustrated in Figure 10. Grid 1 and grid 2 are separated via breakers B1 and B3 from a large microgrid. So, this is a power island. If breaker B2 separates two power islands, they will be two separate power islands as shown in Figure 11.

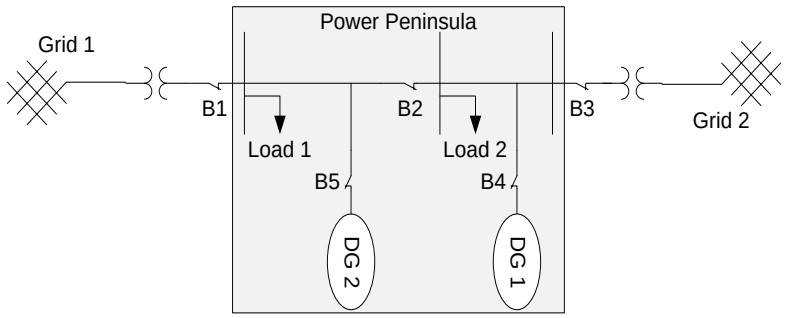

Figure 7. A power peninsula with two connections points to different grids via two main breakers (B1 and B3). Grid 1 and grid 2 are connected via breakers (B1 & B3).

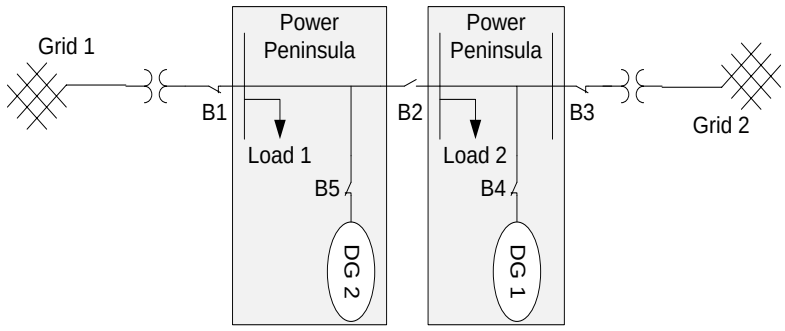

Figure 8. Grid 1 is connected via breaker B1 and grid 2 is connected via breaker B3 to two separate microgrids. These are power peninsulas.

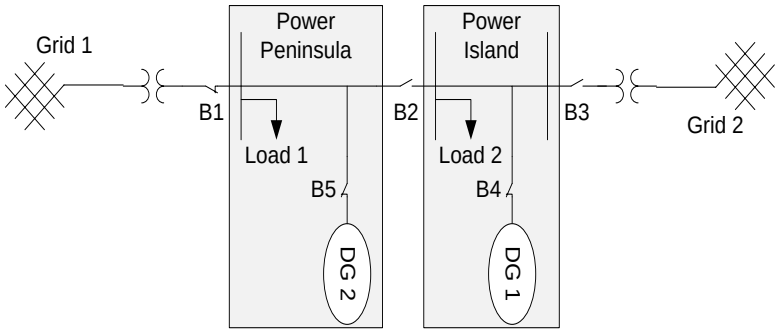

Figure 9. Grid 1 is connected via breaker B1 and grid 2 is separated via breaker B3. So, one of them is a power peninsula and the other one is a power island.

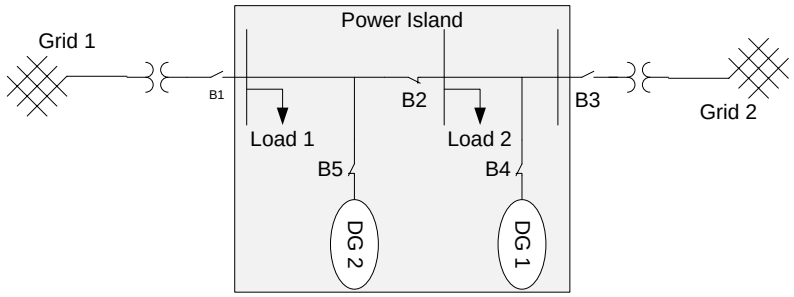

Figure 10. Grid 1 and grid 2 are separated via breakers B1 and B3 from a large microgrid. So, this is a power island.

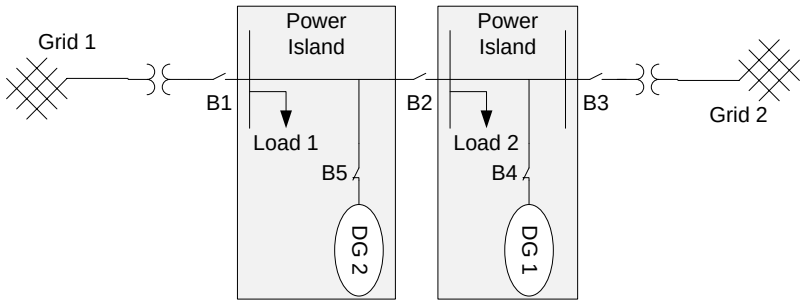

Figure 11. Grid 1 and grid 2 are separated via breakers B1 and B3 from a large microgrid and breaker B2 separates two power islands.

5.3. Changing Power Island to Power Peninsula and Vice Versa

A power peninsula and a power island are illustrated in Figure 12. The power peninsula is connected to grid 1 via breaker B1, but the power island is created by breakers B2, B3, and B7 that separate DG 1 and DG 3 from other networks.

In Figure 13, another peninsula and island create different situations. In this figure, the power peninsula contains DG 2 and DG 3. Power island only contains one DG (DG 1), but it is not important how many DGs there are in sub-microgrids. What is important is the stability of sub-microgrids and situations that will happen in microgrids, grids, and the connection between them.

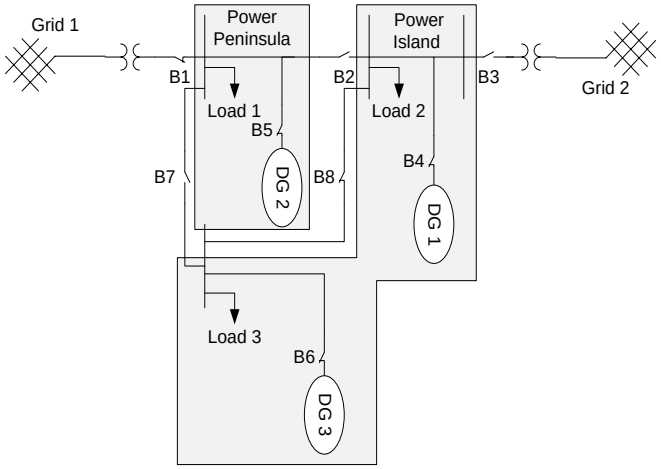

Figure 12. A power peninsula and a power island. The power peninsula is connected to grid 1 via breaker B1.

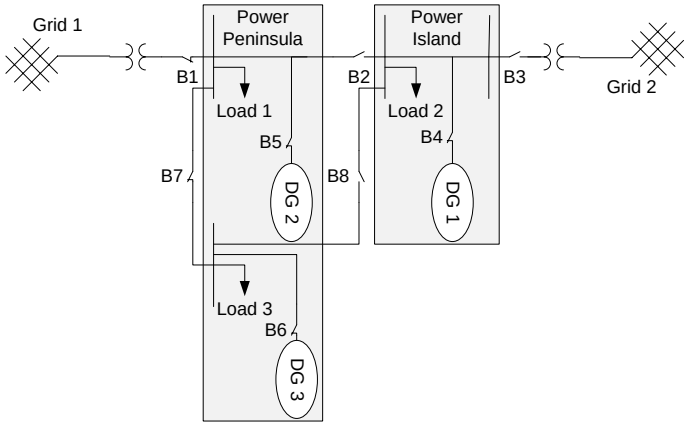

Figure 13. A power peninsula and a power island. The power peninsula is connected to grid 1 via breaker B1, but it contains DG 2 and DG 3.

6. Large microgrids' Formulation

Some possible formations of large microgrids which are shown in previous figures confirm that there are so many states of islanding and peninsulating in large microgrids. So, there should be a method that mathematically formulates connections between large microgrids, grids, sub-microgrids, loads, and other network components.

In a large microgrid, m_D is a matrix that shows the connection between DGs and loads, and m_D is a matrix of microgrid design that describes the connection between DGs and loads in normal utilization of it. In matrix m_D, value 1 shows that a DG is connected to a load or other DGs and 0 shows that it is not connected. As with matrix m_D, M_D is a matrix that shows the connection between grids, DGs, and loads. M_D is a matrix of the main grid design that describes the connection between grids and DGs and also grids and loads in the normal utilization of it. In matrix M_D, 1 shows that a grid is connected to a DG or load and 0 shows that it is not connected.

Another matrix $Grid_D$ is a matrix that shows the connection between grids themselves. $Grid_D$ is a matrix of grid design that describes the connection between main grids in the normal utilization of it. In matrix $Grid_D$, 1 shows that a grid is connected to another grid, and 0 shows that it is not connected.

Finally, matrix Mm_D is a matrix of the main grid and microgrid design that describes all connections in the network in normal utilization.

$$Mm_D = \begin{bmatrix} [m_D]_{i\times i} & [M_D]_{i\times j} \\ [M'_D]_{j\times i} & [Grid_D]_{j\times j} \end{bmatrix}_{(i+j)\times(i+j)} \quad (1)$$

in which i is the number of DGs + loads and j is the number of main grids. This matrix completely describes the connection between grids, DGs, and loads in the network and the large microgrid.

7. A Large Microgrid Example

A large microgrid is illustrated in Figure 14 with four DGs that are connected to three grids and two loads.

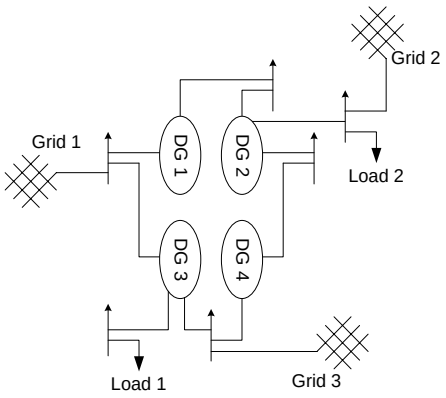

Figure 14. A large microgrid with four DGs that are connected to three grids.

In this example, matrix m_D is:

$$m_D = \begin{array}{c} \\ DG1 \\ DG2 \\ DG3 \\ DG4 \\ Load1 \\ Load2 \end{array} \begin{bmatrix} DG1 & DG2 & DG3 & DG4 & Load1 & Load2 \\ 1 & 1 & 1 & 0 & 0 & 0 \\ 1 & 1 & 0 & 1 & 0 & 1 \\ 1 & 0 & 1 & 1 & 1 & 0 \\ 0 & 1 & 1 & 1 & 0 & 0 \\ 0 & 0 & 1 & 0 & 0 & 0 \\ 0 & 1 & 0 & 0 & 0 & 0 \end{bmatrix} \quad (2)$$

and matrix M_D is:

$$M_D = \begin{array}{c} \\ DG1 \\ DG2 \\ DG3 \\ DG4 \\ Load1 \\ Load2 \end{array} \begin{bmatrix} Grid1 & Grid2 & Grid3 \\ 1 & 0 & 0 \\ 0 & 1 & 0 \\ 1 & 0 & 1 \\ 0 & 0 & 1 \\ 0 & 0 & 0 \\ 0 & 1 & 0 \end{bmatrix}_{6\times3} \quad (3)$$

and matrix $Grid_D$ is:

$$Grid_D = \begin{array}{c} \\ Grid1 \\ Grid2 \\ Grid3 \end{array} \begin{bmatrix} Grid1 & Grid2 & Grid3 \\ 1 & 0 & 0 \\ 0 & 1 & 0 \\ 0 & 0 & 1 \end{bmatrix}_{3\times3} \quad (4)$$

So, matrix Mm_D can be written from Equation (1):

$$Mm_D = \begin{bmatrix} [m_D]_{6\times6} & [M_D]_{6\times3} \\ [M'_D]_{3\times6} & [Grid_D]_{3\times3} \end{bmatrix}_{9\times9} \quad (5)$$

In detail, matrix Mm_D is:

$$Mm_D = \begin{array}{c} \\ DG1 \\ DG2 \\ DG3 \\ DG4 \\ Load1 \\ Load2 \\ Grid1 \\ Grid2 \\ Grid3 \end{array} \begin{array}{c} \begin{array}{ccccccccc} DG1 & DG2 & DG3 & DG4 & Load1 & Load2 & Grid1 & Grid2 & Grid3 \end{array} \\ \begin{bmatrix} 1 & 1 & 1 & 0 & 0 & 0 & 1 & 0 & 0 \\ 1 & 1 & 0 & 1 & 0 & 1 & 0 & 1 & 0 \\ 1 & 0 & 1 & 1 & 1 & 0 & 1 & 0 & 1 \\ 0 & 1 & 1 & 1 & 0 & 0 & 0 & 0 & 1 \\ 0 & 0 & 1 & 0 & 0 & 0 & 0 & 0 & 0 \\ 0 & 1 & 0 & 0 & 0 & 0 & 0 & 1 & 0 \\ 1 & 0 & 1 & 0 & 0 & 0 & 1 & 0 & 0 \\ 0 & 1 & 0 & 0 & 0 & 1 & 0 & 1 & 0 \\ 0 & 0 & 1 & 1 & 0 & 0 & 0 & 0 & 1 \end{bmatrix}_{9\times 9} \end{array} \tag{6}$$

In this example, matrix Mm_D is used to describe large microgrid states. Islanding and peninsulating can be shown by changing connection states. In this example, if a failure happens in the connection of grid 1, and grid 1 is separated from the large microgrid, all connection numbers in matrix Mm_D will change from 1 to 0 (in this example, the connection state between grid 1 to DG 1 and DG 2 will change from 1 to 0).

Using this method, all the states that happen unintentionally or are decided for better performance can be controlled by central microgrid decisions. A large smart microgrid is a system that should control stability, power quality, and other network parameters. The central microgrid decision system controls all islanding and peninsulating states for enhancing the process of the large microgrid and/or sub-microgrids created.

8. Conclusions

This paper presents the detection of islanding and peninsulating in large microgrids which constitute some sub-microgrids with MCPs to different grids. Two new definitions are proposed for large microgrids: “percentage of islanding” and “peninsulating”. These new definitions necessitate a comprehensive reconsideration of the administration and regulation of energy networks, transitioning them from passive systems to innovative and dynamic "smart grids". In the proposed method, the measured utility current and voltage signals and other signals received through a bidirectional communication system in smart grids are used to determine the islanding percentage and decide whether to island or peninsula the microgrid. The shift in the location of measuring currents, voltages, and other signals from the PCC to before the main circuit breaker has resulted in the central microgrid decision system determining whether to isolate, create a peninsula, or enter into other potential states. Peninsulating is a decision made by a central smart microgrid unit, and all unwanted states or decisions for better working can be controlled by central microgrid decisions. So, various hybrid methods are used for this decision in different microgrids based on their conditions. Some possible formations of large microgrids confirm that there are many states of islanding and peninsulating in large microgrids. Therefore, a mathematical formulation is needed to explain the connection between large microgrids, grids, sub-microgrids, loads, and other network components. These new definitions and formulations are used for control stability, power quality, and other network parameters in large smart microgrids. Central microgrid decision system controls all islanding and peninsulating states and creates sub-microgrids, power islands, and power peninsulas for better usage of networks.

References

[1] I. Varjasi, Attila Balogh, and S. Halasz, "Sensorless Control of a Grid-Connected PV Converter." *12th International Power Electronics and Motion Control Conference. IEEE*, 2006.

[2] Photovoltaics, D.G. and Storage, E., "IEEE Application Guide for IEEE Std 1547™, IEEE Standard for Interconnecting Distributed Resources with Electric Power Systems," *IEEE*, 2009.

[3] S. Krishnamurthy, and E. I. Ogunwole, "Microgrid System Design, Modeling, and Simulation," *in Modelling and Control Dynamics in Microgrid Systems with Renewable Energy Resources: Elsevier*, pp. 345-376, 2024.

[4] M. E. Ropp, K. Aaker, J. Haigh, and N. Sabbah, "Using Power Line Carrier Communications to Prevent Islanding [of PV Power Systems]," *Conference Record of the Twenty-Eighth IEEE Photovoltaic Specialists Conference*, pp. 1675-1678, 2000.

[5] I. Pvps, "Evaluation of Islanding Detection Methods for Photovoltaic Utility-Interactive Power Systems," *Report IEA PVPS T5-09*, vol. 180, 2002.

[6] R. Benato, R. Caldon, and F. Cesena, "Carrier Signal-Based Protection to Prevent Dispersed Generation Islanding on MV Systems," 2003.

[7] F. De Mango, M. Liserre, and A. Dell'Aquila, "Overview of Anti-Islanding Algorithms for PV Systems. Part II: Active Methods," *12th International Power Electronics and Motion Control Conference*, pp. 1884-1889, 2006.

[8] V. Menon, and M. H. Nehrir, "A Hybrid Islanding Detection Technique Using Voltage Unbalance and Frequency Set Point," *IEEE Transactions on Power Systems*, vol. 22, no. 1, pp. 442-448, 2007.

[9] W. Xu, and G. Zhang et al., "A Power Line Signaling Based Technique for Anti-Islanding Protection of Distributed Generators-Part I: Scheme and Analysis," *IEEE Transactions on Power Delivery*, vol. 22, no. 3, pp. 1758-1766, 2007.

[10] O. Abarrategui, I. Zamora, D. Larruskain, and A. Iturregi, "Power Line Carrier Communications and Its Interest in the Current Power Grid Scenario," *ICREPQ*, 2008.

[11] I. J. Balaguer, H.-G. Kim, F. Z. Peng, and E. I. Ortiz, "Survey of Photovoltaic Power Systems Islanding Detection Methods," *34th Annual Conference of IEEE Industrial Electronics*, pp. 2247-2252, 2008.

[12] M. G. M. Abdolrasol, and S. Mekhilef, "Robust Hybrid Anti-Islanding Method for Inverter-Based Distributed Generation," *TENCON 2010-2010 IEEE Region 10 Conference*, pp. 13-18, 2010.

[13] A. Timbus, A. Oudalov, and C. N. M. Ho, "Islanding Detection in Smart Grids," *IEEE Energy Conversion Congress and Exposition*, pp. 3631-3637, 2010.

[14] A. Etxegarai, P. Eguía, and I. Zamora, "Analysis of Remote Islanding Detection Methods for Distributed Resources," *International Conference on Renewable Energies and Power Quality*, vol. 1, no. 9, 2011.

[15] C. Li, and C. Cao et al., "A Review of Islanding Detection Methods for Microgrid," *Renewable and Sustainable Energy Reviews*, vol. 35, pp. 211-220, 2014.

[16] A. Pouryekta, V. K. Ramachandaramurthy, N. Mithulananthan, and A. Arulampalam, "Islanding Detection and Enhancement of Microgrid Performance," *IEEE Systems Journal*, vol. 12, no. 4, pp. 3131-3141, 2017.

[17] M.S. Kim, and R. Haider et al., "Comprehensive Review of Islanding Detection Methods for Distributed Generation Systems," *Energies*, vol. 12, no. 5, p. 837, 2019.

[18] B. Chaitanya, A. Yadav, M. Pazoki, and A. Y. Abdelaziz, "A Comprehensive Review of Islanding Detection Methods," *Uncertainties in Modern Power Systems*, pp. 211-256, 2021.

[19] K. V. Ashwin, V. S. R. Kosuru, S. Sridhar, and P. Rajesh, "A Passive Islanding Detection Technique Based on Susceptible Power Indices With Zero Non-Detection Zone Using a Hybrid Technique," *International Journal of Intelligent Systems and Applications in Engineering*, vol. 11, no. 2, pp. 635-647, 2023.

[20] F. Barkat, and A. Cheknane et al., "Review, Analysis, and Performance Evaluation of the Most Common Four Active Methods for Islanding Detection in Grid-Connected Photovoltaic Systems," *Electric Power Systems Research*, vol. 214, 108909, 2023.

[21] F. Mumtaz, K. Imran, A. Abusorrah, and S. B. A. Bukhari, "An Extensive Overview of Islanding Detection Strategies of Active Distributed Generations in Sustainable Microgrids," *Sustainability*, vol. 15, no. 5, p. 4456, 2023.

[22] R. Nale, and M. Biswal et al., "Real-Time Analysis of Islanding Detection Scheme Developed for AC Microgrid System," *Electric Power Systems Research*, vol. 226, 109926, 2024.

[23] A. Hussain, A. Mehdi, and C.-H. Kim, "A Communication-Less Islanding Detection Scheme for Hybrid Distributed Generation Systems Using Recurrent Neural Network," *International Journal of Electrical Power & Energy Systems*, vol. 155, 109659, 2024.

[24] P. P. Parikh, M. G. Kanabar, and T. S. Sidhu, "Opportunities and Challenges of Wireless Communication Technologies for Smart Grid Applications," *IEEE PES General Meeting*, pp. 1-7, 2010.

Acknowledgments
The authors would like to thank Khuzestan water and power authority (KWPA) and management of the office of applied and research for support for this research.

Declaration of Competing Interest
The authors declare that they have no known competing financial interests or personal relationships that could have appeared to influence the work reported in this paper. The ethical issues, including plagiarism, informed consent, misconduct, data fabrication and/or falsification, double publication and/or submission, redundancy, have been completely observed by the authors.

Credit Authorship Contribution Statement
Saman Darvish Kermani: Conceptualization, Data curation, Formal analysis, Methodology, Resources, Software, Validation, Roles/Writing - original draft. **Mohammad Fayazi**: Conceptualization, Resources, Software, Validation, Visualization, Roles/Writing - original draft, Writing-review & editing. **Jamshid Barati**: Methodology, Project administration, Resources, Validation, Visualization, Roles/Writing - original draft. **Mahmood Joorabian**: Conceptualization, Project administration, Supervision, Validation, Visualization, Roles/Writing - original draft.

Bibliography


Saman Darvish Kermani received his PhD degree in 2016 from Shahid Chamran University of Ahvaz, Ahvaz, Iran in the field of electrical engineering. He is currently working at GHD Advisory Melbourne VIC 3000 Australia in the field of renewable energy. His main research interests include optimization, nature-inspired metaheuristic algorithms, islanding, microgrid, smart grid, power quality, modeling of electrical networks, and distributed renewable resources.

Mohammad Fayazi was born in Iran in 1990. He graduated with a Ph.D. in Electrical Power Engineering from the Shahid Chamran University of Ahvaz, Ahvaz, Iran, in 2023. He currently works as a Hydropower plant (HPP) Operation expert at Khuzestan Water & Power Authority (KWPA). He has published more than 7 journal and conference papers. His research interests are fault protection, detection, classification, and location in power systems (Hydro power plants synchronous generators and HVAC, HVDC and hybrid parallel AC/DC transmission lines), Artificial Intelligence (AI), renewable power generation and power quality.

Jamshid Barati was born in 1983 in Iran. He received his bachelor's, master's and doctorate degrees in the field of electrical engineering in 2006, 2009 and 2022, respectively, from Shahid Chamran University of Ahvaz, Ahvaz, Iran. He is currently an assistant professor in the electrical engineering department of Islamic Azad University, Ramhormoz branch. His special interests are power system protection, power system dynamics and FACTS tools.

Mahmood Joorabian was born in Iran, in 1961. He received his B.E.E degree from University of New Haven, CT, USA, M.Sc. degree in Electrical Power Engineering from Rensselaer Polytechnic Institute, NY, USA and Ph.D. degree in Electrical Engineering from University of Bath, Bath, UK in 1983, 1985 and 1996, respectively. He has been with the Department of Electrical Engineering at Shahid Chamran University of Ahvaz, Ahvaz, Iran as Senior Lecturer (1985), Assistant Professor (1996), Associate Professor (2004) and Professor (2009). His main research interests are fault location, FACTS devices, power system protection, power quality, and applications of intelligence technique in power systems.

Journal of Green Energy Research and Innovation

Improving Low Voltage Ride-Through Capability of Doubly-Fed Induction Generator Wind Farms Using Superconducting Fault Current Limiter

Seyed Ehsan Aminoroayaye yamani, Mohammad Amin Bahramian and Ali Asghar Ghadimi

Highlight

- Enhancing DFIG Wind Turbines with SFCL for better Low Voltage Ride-Through
- Tuning SFCL Coil Inductance for Optimal Current Control
- Assessing SFCL-DFIG Performance in Grid Faults via Simulation
- Boosting Wind Energy Integration with Advanced LVRT and Stability

Graphical Abstract

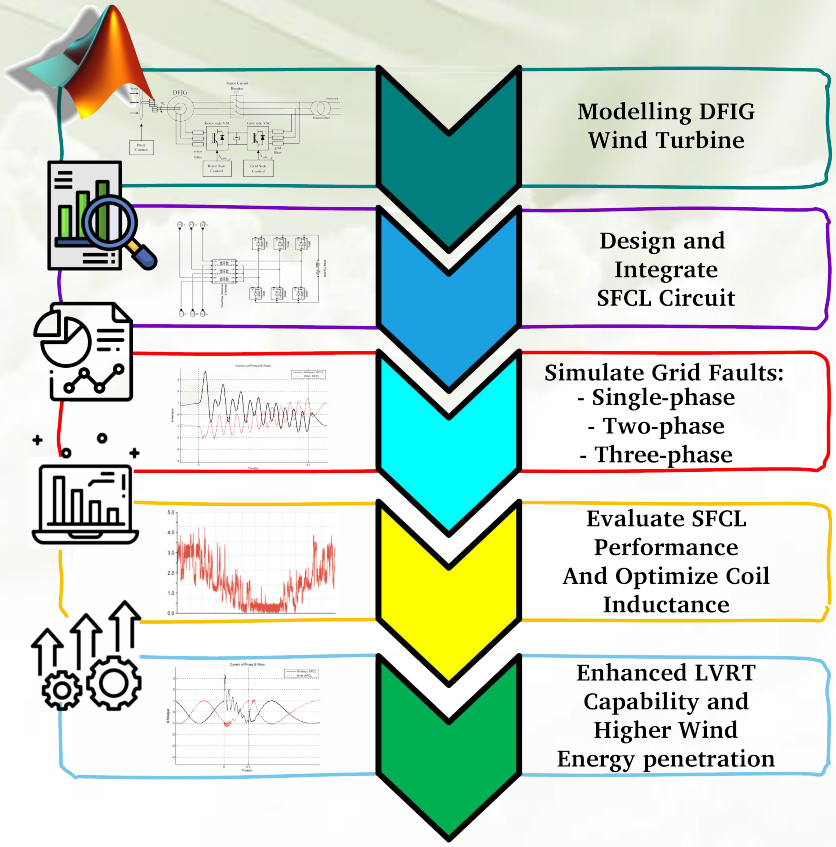

Use your device to scan and read the article online

Citation

S. E. Aminoroayaye yamani, M. A. Bahramian and, A. A. Ghadimi, "Improving Low Voltage Ride-Through Capability of Doubly-Fed Induction Generator Wind Farms Using Superconducting Fault Current Limiter," *Journal of Green Energy Research and Innovation*, vol. 1, no. 2, pp. 15-30, 2024.

https://doi.org/10.61186/jgeri.1.2.15

Online ISSN: 3041-9018

Journal of Green Energy Research and Innovation

Journal Homepage: www.jgeri.araku.ac.ir

Improving Low Voltage Ride-Through Capability of Doubly-Fed Induction Generator Wind Farms Using Superconducting Fault Current Limiter

Seyed Ehsan Aminoroayaye yamani [1], Mohammad Amin Bahramian [2,3], Ali Asghar Ghadimi [2, 3]*

[1] *Department of Electrical Engineering, Payam Golpayegan Institute of Higher Education, Golpayegan, Iran.*
[2] *Department of Electrical Engineering, Faculty of Engineering, Arak University, Arak 38156-8-8349, Iran.*
[3] *Research Institute of Renewable Energy, Arak University, Arak 38156-8-8349, Iran.*

* ***Corresponding Author:*** *a-ghadimi@araku.ac.ir*

ARTICLE INFO

Keywords:
Doubly-fed induction generator,
Low voltage ride-through,
Superconducting fault current limiter,
Wind power plant.

Article history:
Received: 30 December 2023;
Revised: 02 February 2024;
Accepted: 01 March 2024;

Article type:
Research Article

ABSTRACT

Doubly-fed induction generators (DFIGs) are crucial in wind turbines due to their advanced control features and efficient power conversion, but they're vulnerable to grid issues like voltage dips and short circuits. This study explores enhancing DFIGs' low voltage ride-through (LVRT) capabilities using a superconducting fault current limiter (SFCL) system. The SFCL's superconducting coil plays a key role by limiting fault current to stabilize power output, reducing excessive currents during faults, and mitigating voltage fluctuations, protecting the rotor-side converter and gearbox. The research focuses on optimizing the coil's inductance to improve SFCL performance, showing through MATLAB/Simulink simulations that adjusting inductance can lessen rotor current oscillations during short circuits. The results indicate significant enhancements in LVRT capabilities, reducing electrical and mechanical stress on generators and converters, preventing severe voltage drops, and maintaining torque levels. Incorporating an SFCL into DFIG systems greatly increases stability, reliability, and fault tolerance, supporting more wind energy integration.

Nomenclature

Variable	Description	Variable	Description
V_s, V_r	Stator and Rotor voltage	T_e	Torque electromagnetic axis
i_s, i_r	Stator and Rotor current	w_s	Synchronous speed
i_{sc}	The fault current	w_r	Rotor speed
i_{ms}	Magnetizing component of stator current	w_{slip}	Slip speed
i_{rqref}	Reference rotor current	V_{rd}, V_{rq}	d-q components of rotor voltage
a_s, a_r	Stator and Rotor flux	i_{rd}, i_{rq}	d-q components of rotor current
L_s, L_r	Stator and Rotor self-inductance	R_s, R_r	Stator and Rotor resistance
L_m	Magnetizing inductance	T_e	Torque electromagnetic axis
L_{ls}, L_{lr}	Stator and Rotor leakage inductance	w_s	Synchronous speed
R_s, R_r	Stator and Rotor resistance	w_r	Rotor speed

1. Introduction

The DFIG stands as a premier solution for integrating wind turbines with the electrical grid, owing to its superior control features and the efficiency of its compact converter design. DFIGs are distinguished by their exceptional ability to manage and adapt power output, making them highly suitable for renewable energy applications. However, it is imperative to acknowledge that these generators exhibit a heightened sensitivity to voltage fluctuations, particularly in instances of grid faults. This vulnerability is especially pertinent given the geographical positioning of many wind power installations in isolated locales, where they are frequently connected to less robust power grids. Consequently, these systems are more susceptible to disturbances, including voltage sags and short circuits, necessitating sophisticated management and protection strategies to ensure grid stability and reliability.

Upon the occurrence of a grid short circuit, there is an alteration in grid voltage, precipitating elevated induced voltages within the DFIG rotor circuit. In the absence of effective control measures, this scenario can provoke the generation of high currents within the rotor circuit, endangering the integrity of the rotor-side converter (RSC). Amid such a fault, the magnitude and frequency of induced voltage in the rotor circuit undergo significant shifts, surging to levels substantially above the norm. In these situations, the DFIG's standard control system is inept at furnishing suitable control signals for the RSC converter, owing to the Proportional-Integral (PI) controllers in the control loops being unadjusted for these extreme scenarios and lacking the requisite agility for managing such states. Consequently, the DFIG's protective system initiates a block to avert damage to the electronic converters within the RSC, culminating in the disconnection of the wind turbine from the circuit [1]. However, DFIG's disconnection from the circuit contradicts grid regulations, which stipulate that large wind farms must remain connected to the grid during faults and not be disconnected from service. Therefore, it is essential to quickly detect faults in the grid and implement appropriate control actions to keep the wind turbine connected to the grid without being disconnected from service.

Numerous strategies have been proposed to improve the LVRT capability of the DFIG. The rotor crowbar circuit is commonly utilized to safeguard the RSC. Furthermore, the significance of the grid-side converter has been highlighted, with its role being integral to the Energy Conversion System (ECS) of the DFIG or operating independently as a unified voltage restorer. The introduction of an additional resistive circuit, serving as a current limiter in conjunction with the stator resistance and a passive resistive network, has been suggested. This resistive circuit plays a pivotal role in limiting the surge current in the rotor and mitigating electromagnetic torque oscillations. Additionally, the incorporation of an energy storage device is instrumental in stabilizing the DC-Link voltage, thereby offering a protective mechanism for the RSC. Moreover, a specialized control strategy has been developed to augment the LVRT capacity of DFIG, with subsequent validation indicating enhanced LVRT performance.

During a network fault connected to a wind turbine equipped with a DFIG, two crucial issues arise. One is fault detection, and the other is restricting the fault effects to protect

stator windings, especially the electrical converters in the rotor. So far, the "crowbar" has been widely used to limit fault current. The crowbar is a set of resistances connected in parallel with the rotor windings, short-circuiting the rotor winding circuit during faults and preventing fault current from flowing through the Rotor-Side Converter. However, with the introduction of the crowbar, the DFIG transforms into a conventional induction generator, absorbing reactive power from the grid and limiting the control capability of the wind turbine's power. In [2] and [3], methods have been proposed to improve the crowbar's response speed; however, the issue of reactive power absorption still persists. In [4], a control method for the grid-side converter to enhance DFIG performance during faults is presented, which suffers from control scheme complexity and inconsistency in fault and normal DFIG operation. [5] proposes the use of dynamic series resistors with the rotor, introducing system reliability concerns, thermal issues, and generating high voltages that can disrupt RSC performance when fault current passes through these resistors.

Also, the integration of renewable energy, particularly wind power, calls for innovative strategies to ensure grid stability. Recent studies have focused on improving DFIG systems' fault ride-through capabilities and reducing grid disturbances through advanced control strategies [6], fault current limiters [7,8], and power flow controllers [9]. Additionally, research into limiting fault currents [10,11], enhancing proactive stabilization [12], and integrating systems for better frequency regulation [13], alongside developing multifunctional limiters for power management [14], highlights a concerted effort towards robust wind power integration. The literature has investigated multiple solutions to enable higher penetration levels of renewables, notably forecasting and scheduling optimization for resilience [15], incorporating energy storage for stability [16-18], advanced power electronics interfaces, dynamic demand response, and virtual synchronous machines. Recent researches have also delved into enhancing the efficiency and reliability of renewable and hybrid systems. Studies have introduced optimal operation models for multi-energy microgrids [19], innovative short-term load forecasting techniques sensitive to weather changes [20], and advanced power flow analysis methods for AC microgrids [21], showcasing the evolving landscape of smart grid optimization and management.

In this article, we propose integrating a SFCL into the rotor circuit of DFIG wind turbines to enhance their LVRT capability. The SFCL serves three key functions: acting as a fault current limiter during normal operation, restricting excess stator and rotor currents during grid faults, and attenuating voltage fluctuations in the rotor circuit to protect the converter and gearbox. We examine tuning the SFCL coil inductance to optimize its current limiting performance. The effectiveness of the SFCL-enhanced DFIG system is evaluated under various grid fault scenarios through simulations in the MATLAB/Simulink environment. The results demonstrate substantial improvements in LVRT capability, reduced electrical/mechanical stresses, avoidance of severe voltage drops, and prevention of torque drops to zero, highlighting the potential of this solution to enable higher wind energy penetration levels.

The remainder of the article is structured as follows: Section 2 provides details on the wind turbine structure and modeling of the DFIG and its control circuits, as well as the operating principles of the SFCL. Section 3 presents the simulation setup and results evaluating the performance of the proposed SFCL-integrated DFIG system under different grid fault conditions. Finally, Section 4 concludes the article and outlines potential future research directions.

2. Wind Turbine Structure

Here, the problem of planning the presence of EV charging stations in smart distribution systems is discussed to enhance the power output and electrical parameters of the distribution system.

2.1. Modeling Doubly-fed Induction Generators

A wind turbine equipped with a doubly-fed induction generator consists of three main components: the turbine blades, the DFIG generator, and the power electronic converter. The turbine blades capture wind energy and transform it into mechanical rotation, which is then transmitted to the DFIG generator through a gearbox. The DFIG generator receives the mechanical energy and converts it into electrical energy. Figure 1 illustrates the structure of a DFIG. In this model, the stator coil is directly connected to the network through an electronic converter, and the rotor coil is also connected to the network through an electronic converter. The electronic converter, consists of two converters: the Rotor-Side Converter and the Grid-Side Converter. They are connected back-to-back, and a capacitor is placed in the DC link between them as shown in Figure 2. The Grid-Side Converter maintains a constant voltage in the DC link, while the Rotor-Side Converter controls the current and voltage in the rotor circuit.

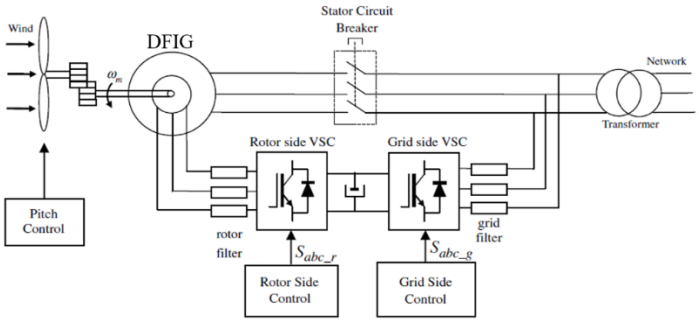

Figure 1. Wind turbine structure equipped with DFIG.

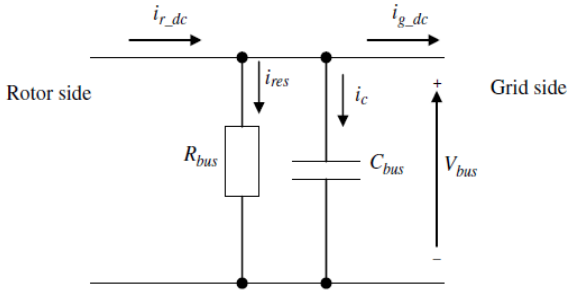

Figure 2. DC-link System.

By adjusting these, the active and reactive power produced by the Doubly Fed Induction Generator can be controlled. The dynamic model of DFIG examines the behaviour of its variables in transient and steady states, essential for the proper design and control of DFIG.

Dynamic behaviour of machines is usually studied using their "dynamic model." By utilizing the dynamic model of a machine, the behaviour of its variables, such as torque, currents, and fluxes at all times (not just in a steady state) when a specified supply voltage is applied, becomes apparent. Information obtained from the dynamic model allows the identification of unsafe machine conditions, such as instability or extreme transient currents. Additionally, the dynamic model provides more insights into the performance of the stable system, such as dynamic oscillations, torque ripple, flux variations, and more. The dynamic model is presented in the form of a compact set of ordinary differential equations, enabling computer simulation, often referred to as "simulation model." Using this model, the analysis of the behaviour of all machine variables at every moment of machine operation becomes possible.

2.2. Dynamic Modeling of Doubly-Fed Induction Generator

Deep analysis of DFIG provides a profound understanding of its behaviour in transient and steady-state conditions. This information is essential for the proper design and control of DFIGs. The dynamic behaviour of DFIGs is typically examined using a mathematical model that encompasses complex relationships between machine variables, such as torque, currents, and fluxes. Through model simulation, engineers can accurately predict machine behavior across a wide spectrum of operational scenarios. The dynamic analysis of DFIGs pursues two objectives: it aids in identifying potential issues, such as instability or extreme transient currents, while optimizing machine performance, including reducing oscillations and enhancing efficiency.

The dynamic model of DFIGs is usually presented as a compact set of ordinary differential equations, facilitating computer simulation. Hence, it is often referred to as a "simulation model." Using this model, engineers can scrutinize the intricate behavior of all machine variables throughout the entire operational cycle. In summary, the dynamic analysis of DFIGs forms the foundation for their proper design and control, providing engineers with the capability to anticipate potential issues, optimize performance, and ensure the stability and efficiency of the machine under various operational conditions.

2.3. Control Circuit of the Rotor-Side Converter

The purpose of the Rotor-Side Converter is to control the rotor currents. The Rotor-Side Converter serves as a torque controller for adjusting the output of the wind turbine and measuring the active or reactive power at the stator terminal. To minimize the error in power or rotor speed towards zero, a PI controller is employed in an external control loop. The output of the current controller, the reference rotor current, should be injected into the rotor coil by the Rotor-Side Converter. This component controls the torque electromagnetic axis. The real part of the rotor current is compared with the reference

rotor current, and the error is driven to zero by the PI current controller in the inner control loop. The output of this current controller is the voltage, generated by the Rotor-Side Converter and combined with other similar controllers for (i_{rd}), (v_{rd}), and the required three-phase voltage applied to the rotor coil. The voltage equations are as follows:

$$V_s = i_s * R_s + {}^{d\alpha}/_{dt} \quad (1)$$

$$V_r = i_r * R_r + {}^{d\alpha}/_{dt} \quad (2)$$

Here, V_s represents the applied stator voltage to the network. The rotor voltage V_r is controlled by the rotor-side converter and is used to control the generator's performance. The flux equations are as follows:

$$\alpha_s = L_s * i_s + L_m * i_r \quad (3)$$

$$\alpha_r = L_m * i_s + L_r * i_r \quad (4)$$

L_s and L_r will be driven, respectively.

$$L_s = L_m + L_{ls} \; and \; L_r = L_m + L_{lr} \quad (5)$$

The leakage coefficient is defined as:

$$\sigma = 1 - \frac{L_m^2}{L_r} * L \quad (6)$$

$$L_0 = L_m^2 / L_s \quad (7)$$

$$V_{rd} = i_{rd} * R_r + \sigma L_r * \frac{d_{ird}}{dt} - w_{slip} * \sigma L_r * i_{rq} \quad (8)$$

$$V_{rq} = i_{rq} * R_r + \sigma L_r * \frac{d_{irq}}{dt} - w_{slip}(\sigma L_r * i_{rd} + L_0 * i_{ms}) \quad (9)$$

$$w_{slip} = w_s - w_r \quad (10)$$

The stator flux angle is calculated using the following formula:

$$\alpha_{st} = \int (V_{st} - i_s * R_s) dt \quad (11)$$

$$\alpha_{sb} = \int (V_{sb} - i_s * R_s) dt \quad (12)$$

$$\theta_s = tan^{-1}\left({}^{\alpha_{st}}/_{\alpha_{sb}}\right) \quad (13)$$

The calculated parameters obtained from the above equations in the PI controller system are employed to enable the controller to regulate speed and torque in the generator. This allows the controller to have dual-mode functionality instead of directly adjusting the active power. The fundamental operation of the Superconducting Fault Current Limiter involves limiting the fault current in a unidirectional manner. During normal operation, the fault current is regulated to be within the peak range of ni_{rabc} or ni_{sabc}, representing the rotor current and stator current, with 'n' being the transformer ratio. Under normal conditions, the SC exhibits a non-inductive impedance, with the voltage drop across the unidirectional rectifier and the voltage drop from the resistance of the winding and leakage inductance of the isolated transformer being the only significant impedances in the circuit. During a fault, when the current magnitude reaches $\frac{i_{sc}}{n}$, the SFCL enters the circuit. The impedance of the fault circuit increases, limiting the

fault current to a predetermined level. When the fault current is cleared, and the rotor or stator current drops below $\frac{i_{sc}}{n}$, the SFCL automatically exits the circuit.

2.4. Control Circuit of the Grid-Side Converter

The purpose of the Grid-Side Converter is to regulate the voltage of the DC link capacitor. Therefore, it is authorized to generate or absorb the reactive power required to support the voltage. This function is achieved through two internal control loops and an external regulating loop. The measured current at the output is utilized by a voltage controller to regulate the current. The internal current control loop consists of a current controller to control the magnitude and phase of the voltage produced by the converter.

2.5. Superconducting Fault Current Limiter

The use of current limiters during short-circuit events contributes to optimal current control. Almost all current limiters during short-circuits operate by introducing a significant impedance in series with the system. The introduction of this impedance has led to the development of various current limiters for power systems, demonstrating significant advancements over the past three decades. The Superconducting Fault Current Limiter is one of the most effective types. However, during a network fault, the SFCL impedance rapidly transitions from a superconducting state to a normal state, swiftly limiting the fault current and reducing various fault types. These limiters do not require control circuits and automatically increase impedance during a short-circuit incident, restricting the fault current in less than half a cycle.

Nevertheless, due to challenges such as lengthy recovery and high costs at high voltage levels, the practical use of these limiters is not feasible and requires further research. In this article, the implementation of a diode-bridge-type superconducting fault current limiter is examined, reducing associated weaknesses such as extended recovery time and high costs. In practical operation, the current passing through the superconductor during continuous network operation remains almost constant. Consequently, it acts as an equivalent short circuit to a secondary transformer, leading to a substantial reduction in voltage drop across the secondary transformer and, as a result, almost eliminating the voltage drop in the primary transformer series. Thus, the current limiter has no significant effect on restricting fault current during normal network operation, which is one of its main advantages. In the event of a fault on the load side, the impedance circuit resulting from the superconductor limits the fault current. The main advantage of this limiter is its ability to prevent a sudden increase in fault current during a short-circuit incident, with the fault current gradually increasing with the rise in superconductor current. The research methodology is outlined through a process flowchart in Figure 3, depicting the sequential integration of the Superconducting Fault Current Limiter into Doubly-Fed Induction Generator wind turbine systems and subsequent optimization in MATLAB/Simulink.

3. Simulation and Results

In this section, to examine the performance of the presented system, an SFCL circuit in a 1.5 MW dual-fed induction generator connected to the grid is simulated using the Simulink environment in MATLAB. Table 1 will present the parameters of the DFIG under study and the network connected to it. Subsequently, the performance of the DFIG under normal grid voltage conditions and with the proposed method added to the circuit will be investigated. Furthermore, the performance of the proposed method will be examined under various network fault scenarios. For this purpose, the system's performance will be evaluated under single-phase to ground faults, two-phase to ground faults, and three-phase to ground faults. During the analysis of the DFIG performance, wind blows at a constant speed of 15 meters per second, and the reactive power generated by the DFIG is set to zero per unit. The graphical representation of the system in the DFIG is connected to the grid through a transformer 25 KV / 575 V and two parallel 30-kilometer lines. These lines are arranged in parallel to each other so that in the event of a fault in one of them, the other line maintains the DFIG's connection to the grid, enhancing the system's reliability. The 25-kilovolt network is also connected to the main 120 KV network through a transformer 120 KV / 25 KV. The graphical representation of the DFIG system connected to the grid along with the SFCL circuit is shown in Figure 4. The SFCL circuit employed, illustrated in Figure 5, is a diode-bridge type configuration comprising a superconducting coil connected to a rectifier bridge. This SFCL design serves the dual purpose of limiting fault currents during grid disturbances and attenuating voltage fluctuations in the DFIG's rotor circuit.

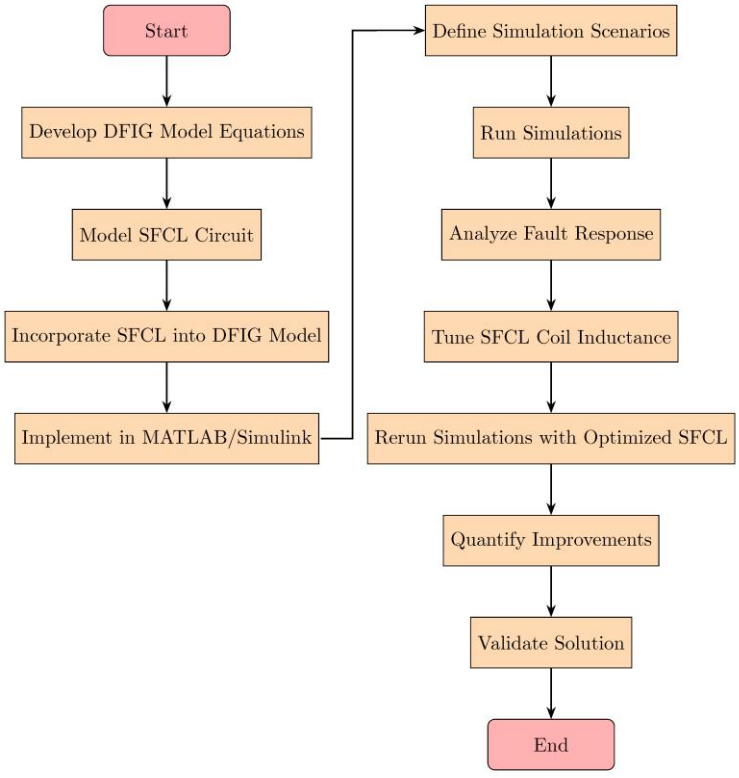

Figure 3. Process flowchart for the integration of SFCL into DFIG systems and optimization in MATLAB/Simulink.

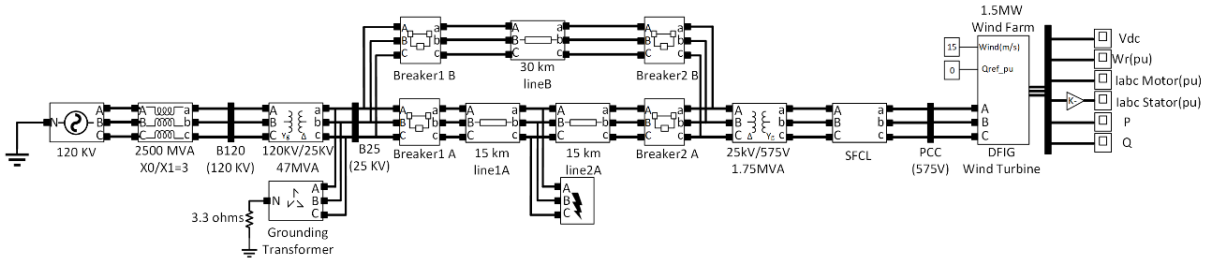

Figure 4. Wind turbine circuit with SFCL.

Table 1. Doubly Fed Induction Generator and Grid Information**.**

Parameter	Value
Grid Voltage	575 volts
Frequency	60 Hz
Rated Power	1.5 MVA
R_s	0.023 PU
L_{ls}	0.18 PU
R'_r	0.016 PU
L'_r	0.16 PU
L_m	2.9 PU
H	0.685 PU
p	3 Pairs of Poles
C	10 mF

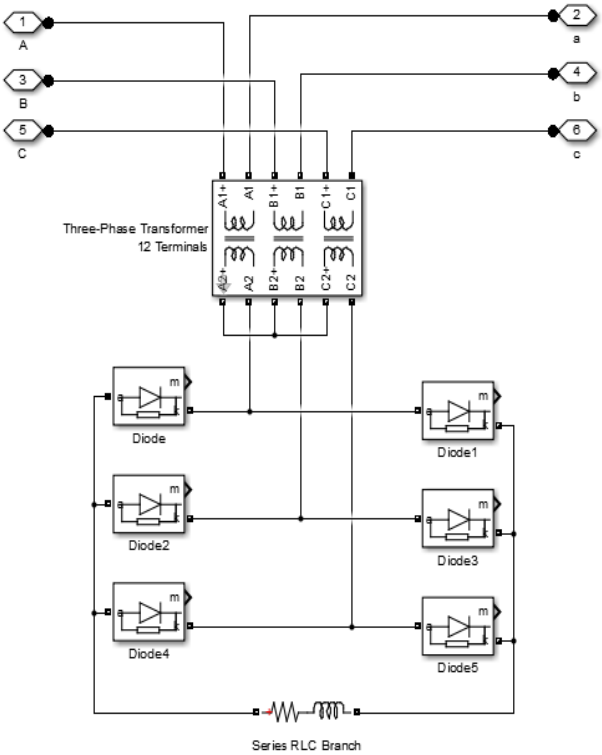

Figure 5. The SFCL circuit.

In this study, the performance of SFCL in the event of single-phase, two-phase, and three-phase short circuits has been investigated. Furthermore, the impact of the coil value used in the SFCL circuit has been evaluated. Figure 6 illustrates the results of simulating a single-phase fault. As evident, in this scenario, the presence of SFCL has a negligible effect on limiting the short-circuit current in the rotor and stator windings. The dashed line waveform corresponds to the circuit with SFCL. However, the results indicate that the presence of SFCL reduces transient and sub-transient oscillations in the rotor current, resulting from the occurrence of a two-phase short circuit to the ground in the system, to an acceptable level as shown in Figure 7. Since decreasing the peak value of sub-transient oscillations reduces the likelihood of triggering the wind turbine's trip and its disconnection from the circuit, employing the SFCL circuit in wind turbines is justified.

Similarly, to Figure 7, Figure 8 illustrates the effect of the SFCL on limiting the current, but this time for the stator phase b current during a two-phase-to-ground fault scenario. The figure presents two waveforms: the dashed line waveform corresponds to the circuit with the SFCL integrated, while the solid line waveform represents the circuit without the SFCL. Analogous to the rotor current behavior observed in Figure 7, the results in Figure 8 demonstrate that the presence of the SFCL significantly reduces the magnitude and range of oscillations in the stator current compared to the circuit without the SFCL. The dashed line waveform, which includes the SFCL, exhibits a smaller oscillation amplitude and a quicker damping of the oscillations in the stator current than the solid line waveform without the SFCL. This damping effect on the stator current oscillations is beneficial as it helps prevent potential damage to the circuit and generator windings caused by excessive current levels during the two-phase-to-ground fault condition. As mentioned, the presence of SFCL results in all three stator phase currents having smaller oscillation amplitudes. This prevents damage to the circuit and the generator windings. Figure 9 illustrates that the presence of SFCL further limits the oscillations in the rotor current during a three-phase short circuit to the ground, reducing the likelihood of wind turbine disconnection and increasing the possibility of its recovery after a fault occurs.

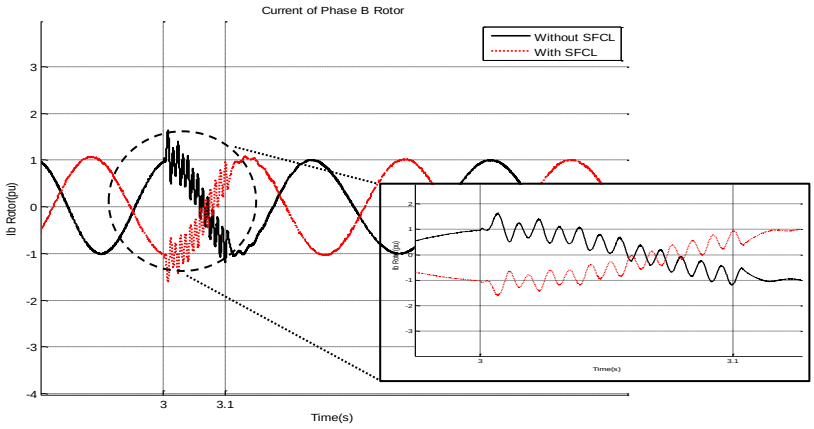

Figure 6. The effect of SFCL on limiting the phase a current of the rotor in a single phase to ground fault.

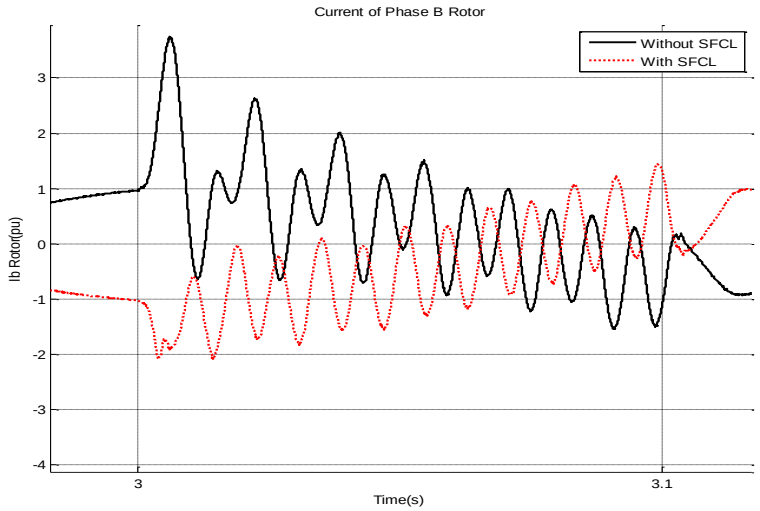

Figure 7. The impact of SFCL on limiting the phase b current of the rotor in a two-phase to ground fault.

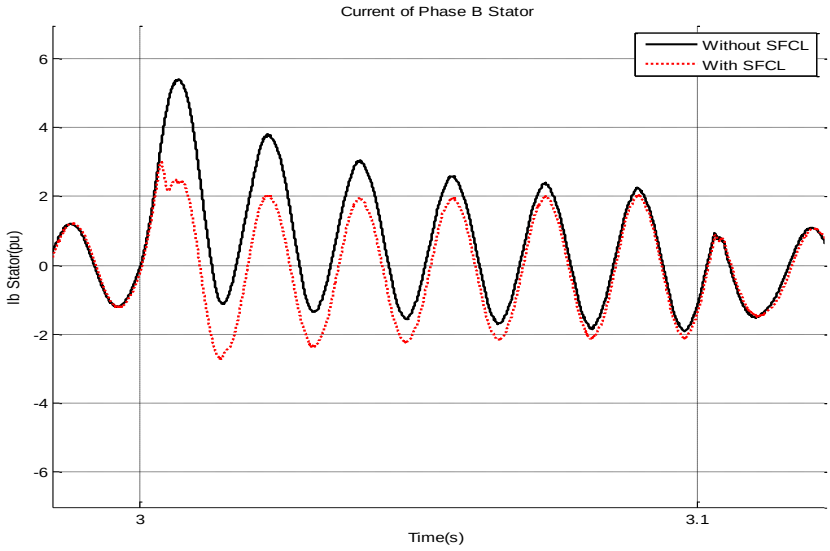

Figure 8. The effect of SFCL on limiting the phase b current of the stator in a two-phase to ground fault.

Further investigation examined the impact of varying the SFCL circuit's coil inductance value on the rotor current oscillations during short circuit events. The results, as depicted in Figures 10 and 11, indicate that determining the coil value in a way that places the coil current in continuous conduction mode (CCM) yields the maximum reduction in rotor current oscillations.

Figure 10 shows the rotor phase 'b' current with an SFCL coil inductance of 0.1 Henry during a three-phase to ground fault. While the dashed line waveform (with SFCL) exhibits reduced oscillations compared to the solid line waveform (without SFCL), further optimization is possible. Figure 11, on the other hand, illustrates the rotor phase 'b' current when the SFCL coil inductance is set to the calculated optimal value of approximately 0.2 Henry for the studied system.

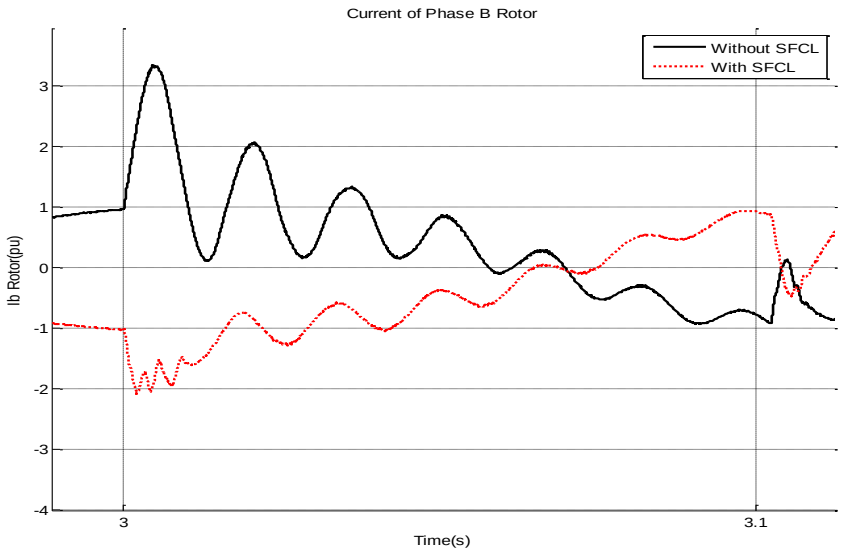

Figure 9. The effect of SFCL on limiting the phase b current of the stator in a three-phase to ground fault.

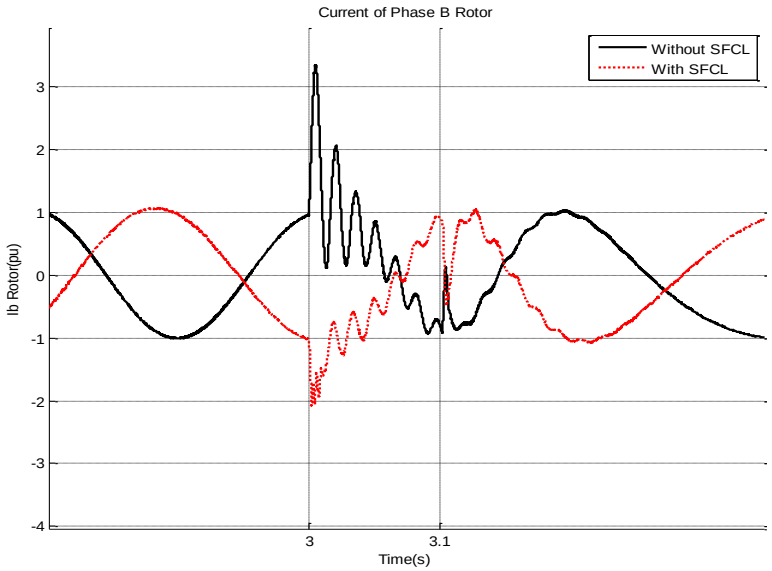

Figure 10. Phase b current of the rotor during three-phase-to-earth fault in two states with SFCL and without SFCL, when the value of the inductor is 0.1 H.

The dashed line waveform in this figure demonstrates significantly diminished rotor current oscillations during the three-phase fault, highlighting the importance of tuning the coil inductance to achieve maximum effectiveness in mitigating transient phenomena and enhancing the low voltage ride-through capability of the DFIG wind turbine.

Tables 2 and 3 comprehensively present the peak stator and rotor currents for various inductor values under different fault conditions, with and without the SFCL. The tabulated data validates the SFCL's ability to substantially reduce peak currents, thereby mitigating electrical and mechanical stresses on the generator and converters during grid disturbances. Collectively, these results demonstrate the proposed SFCL system's viability in bolstering the low voltage ride-through capabilities of DFIG-based wind farms, paving the way for higher renewable energy penetration levels.

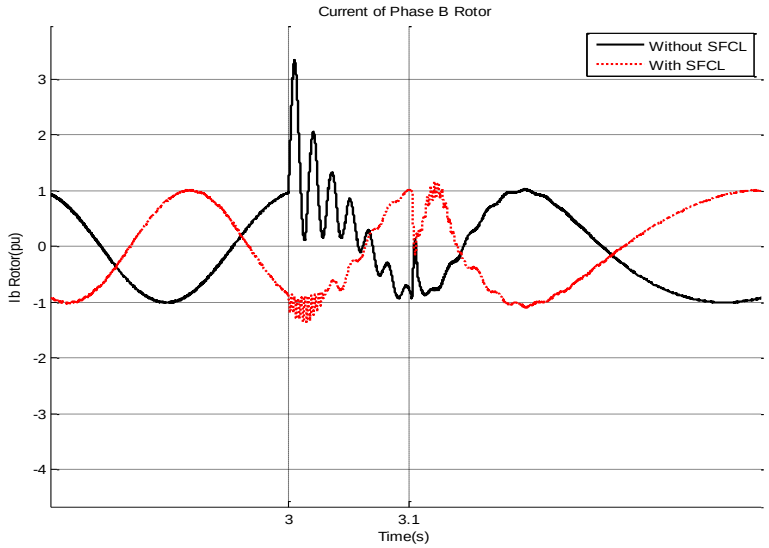

Figure 11. Phase b current of the rotor during three-phase-to-earth fault in two states with SFCL and without SFCL, when the value of the inductor is 0.2 H.

Table 2. Peak current of the stator for different inductor values.

Stator Current (PU)						
Type of short circuit						
SFCL Value (H)	Three-phase to ground		Two-phase to ground		Single-phase to ground	
	Without SFCL	With SFCL	Without SFCL	With SFCL	Without SFCL	With SFCL
0.1	4.77	2.54	4.77	2.54	1.79	1.76
0.2	4.77	1.81	4.77	1.81	1.79	1.55
0.3	4.77	2.05	4.77	2.05	1.79	1.72
0.5	4.77	1.90	4.77	1.90	1.79	1.75
0.9	4.77	2.89	4.77	2.70	1.79	2.60
1.2	4.77	3.26	4.77	3.29	1.79	3.30

Table 3. Peak current of the rotor for different inductor values.

Rotor Current (PU)						
Type of short circuit						
SFCL Value (H)	Three-phase to ground		Two-phase to ground		Single-phase to ground	
	Without SFCL	With SFCL	Without SFCL	With SFCL	Without SFCL	With SFCL
0.1	3.35	1.76	3.35	1.75	1.64	1.53
0.2	3.35	1.17	3.35	1.17	1.64	1.24
0.3	3.35	1.45	3.35	1.45	1.64	1.33
0.5	3.35	1.59	3.35	1.44	1.64	1.38
0.9	3.35	2.08	3.35	2.11	1.64	2.03
1.2	3.35	2.34	3.35	2.32	1.64	2.36

4. Conclusions

In this study, we have demonstrated the effectiveness of integrating Superconducting Fault Current Limiters with Doubly-Fed Induction Generator wind farms to significantly enhance their Low Voltage Ride-Through capabilities. Our findings highlight the potential for SFCL technology to mitigate the adverse effects of grid disturbances, thereby improving the reliability and stability of wind power generation systems. Through comprehensive simulations conducted in MATLAB/Simulink, we have validated the improved performance of DFIG systems under various fault conditions, underscoring the viability of SFCL as a robust solution for enhancing wind farm resilience. The successful implementation of SFCL in DFIG systems not only addresses current challenges in wind power generation but also sets a foundation for the future integration of renewable energy sources into the power grid. Our study contributes to the body of knowledge by providing a detailed analysis of the SFCL-DFIG interaction and its impact on system performance, offering valuable insights for researchers, engineers, and policymakers involved in the renewable energy sector.

While this study provides a comprehensive assessment of SFCL integration with DFIG wind farms, several avenues for future research emerge from our work. These include:

1. Broadening SFCL use in renewables like solar and hydro needs exploration for wider benefits and challenges.

2. More sophisticated SFCL-DFIG control algorithms could significantly enhance performance and efficiency under variable grid conditions.

3. It's crucial to conduct a comprehensive economic analysis on SFCL integration in renewables to understand its cost-benefit, including potential savings from enhanced reliability.

4. Examining SFCL's impact on grid stability, quality, and resilience is essential for its sustainable and secure expansion.

These directions will help further renewable energy integration, contributing to a more sustainable and resilient future. By pursuing these future research directions, the scientific community can build upon the foundational insights provided by this study, driving forward the integration of renewable energy into the global power grid and advancing the pursuit of a more sustainable and resilient energy future.

References

[1] W. Qiao, G. K. Venayagamoorthy, and R. G. Harley, "Real-Time Implementation of a STATCOM on a Wind Farm Equipped with Doubly Fed Induction Generators," *IEEE Transactions on Industry Applications*, vol. 45, no. 1, pp. 98-107, 2009.

[2] J. Lopez, E. Gubia, E. Olea, J. Ruiz, and L. Marroyo, "Ride Through of Wind Turbines with Doubly Fed Induction Generator Under Symmetrical Voltage Dips," *IEEE Transactions on Industrial Electronics*, vol. 56, no. 10, pp. 4246-4254, 2009.

[3] I. Erlich, J. Kretschmann, J. Fortmann, S. Mueller-Engelhardt, and H. Wrede, "Modeling of Wind Turbines Based on Doubly-Fed Induction Generators for Power System Stability Studies," *IEEE Transactions on Power Systems*, vol. 22, no. 3, pp. 909-919, 2007.

[4] P. S. Flannery, and G. Venkataramanan, "A Fault Tolerant Doubly Fed Induction Generator Wind Turbine Using a Parallel Grid Side Rectifier and Series Grid Side Converter," *IEEE Transactions on Power Electronics*, vol. 23, no. 2, pp. 1126-1135, 2008.
[5] Y. Jin, J. E. Fletcher, and J. O'Reilly, "A Series-Dynamic Resistor-Based Converter Protection Scheme for Doubly-Fed Induction Generator During Various Fault Conditions," *IEEE Transactions on Energy Conversion*, vol. 25, no. 2, pp. 422-432, 2010.
[6] N. R. Naguru, A. Karthikeyan, C. Nagamani, and V. S. Kumar, "Comparative Study of Power Control of DFIG Using PI Control and FeedBack Linearization Control," *International Conference on Advances in Power Conversion and Energy Technologies (APCET)*, pp. 1-6, 2012.
[7] A. R. Fereidouni, B. Vahidi, and T. H. Mehr, "The Impact of Solid State Fault Current Limiter on Power Network With Wind-Turbine Power Generation," *IEEE Transactions on Smart Grid*, vol. 4, no. 2, pp. 1188-1196, 2012.
[8] G. Rashid, and M. H. Ali, "Transient Stability Enhancement of Doubly Fed Induction Machine-Based Wind Generator by Bridge-Type Fault Current Limiter," *IEEE Transactions on Energy Conversion*, vol. 30, no. 3, pp. 939-947, 2015.
[9] M. Firouzi, G. B. Gharehpetian, and B. Mozafari, "Power-Flow Control and Short-Circuit Current Limitation of Wind Farms Using Unified Interphase Power Controller," *IEEE Transactions on Power Delivery*, vol. 32, no. 1, pp. 62-71, 2016.
[10] M. S. Alam, M. A. Abido, and I. El-Amin, "Fault Current Limiters in Power Systems: A Comprehensive Review," *Energies*, vol. 11, no. 5, p. 1025, 2018.
[11] G. M. Gomes Guerreiro, R. Sharma, F. Martin, P. Ghimire, and G. Yang, "Concerning Short-Circuit Current Contribution Challenges of Large-Scale Full-Converter based Wind Power Plants," *IEEE Access*, vol.11, pp. 64141 – 64159, 2023.
[12] P. Verma, and P. Gupta, "Proactive Stabilization of Grid Faults in DFIG Based Wind Farm Using Bridge Type Fault Current Limiter Based on NMPC," *Energy Sources, Part A: Recovery, Utilization, and Environmental Effects*, vol. 45, no. 2, pp. 6062-6081, 2023.
[13] X. Liu, and W. Han et al., "Active Fault Current Limitation for VSC-MTDC Integrated Offshore Wind Farms Participating in Frequency Regulation," *IEEE Transactions on Sustainable Energy*, pp. 1 – 15, 2023.
[14] M. Ghorbani, M. Firouzi, B. Mozafari, and F. Golshan, "Power Flow Management and LVRT Enhancement by Using Multi-Functional Capacitive Bridge-Type Fault Current Limiter in DFIG System," *International Journal of Electrical Power & Energy Systems*, vol. 148, 108810, 2023.
[15] D. Baimel, "Transient Stability Enhancement of Steam Turbine-Based Power Plant by Using Improved Bridge Fault Current Limiter," *Engineering Science and Technology, an International Journal*, vol. 39, 101345, 2023.
[16] L. F. Azeredo, and I. Yahyaoui et al., "Study of Reducing Losses, Short-Circuit Currents and Harmonics by Allocation of Distributed Generation, Capacitor Banks and Fault Current Limiters in Distribution Grids," *Applied Energy*, vol. 350, 121760, 2023.
[17] B. Carbonell, and C. Cardozo et al., "An Open Source Modelica Implementation of The IEC 61400-27-1 Type 4 Wind Turbine Model for Power System Stability Assessment," *Electric Power Systems Research*, vol. 214, 108313, 2023.
[18] M. Sarwar, and M. Arshed et al., "Stability Enhancement of Grid-Connected Wind Power Generation System Using PSS, SFCL and STATCOM," *IEEE Access*, vol. 11, pp. 30832-30844, 2023.
[19] A. Mobasseri, M. Tostado-Véliz, A. A. Ghadimi, M. R. Miveh, and F. Jurado, "Multi-Energy Microgrid Optimal Operation with Integrated Power to Gas Technology Considering Uncertainties," *Journal of Cleaner Production*, vol. 333, 130174, 2022.
[20] A. Mansouri, A. H. Abolmasoumi, and A. A. Ghadimi, "Weather Sensitive Short Term Load Forecasting Using Dynamic Mode Decomposition with Control," *Electric Power Systems Research*, vol. 221, 109387, 2023.
[21] M. Bayat, M. M. Koushki, A. A. Ghadimi, M. Tostado-Véliz, and F. Jurado, "Comprehensive Enhanced Newton Raphson Approach for Power Flow Analysis in Droop-Controlled Islanded AC Microgrids," *International Journal of Electrical Power & Energy Systems*, vol. 143, 108493, 2022.

Declaration of Competing Interest

The authors declare that they have no known competing financial interests or personal relationships that could have appeared to influence the work reported in this paper. The ethical issues, including plagiarism, informed consent, misconduct, data fabrication and/or falsification, double publication and/or submission, redundancy, have been completely observed by the authors.

Credit Authorship Contribution Statement

Seyed Ehsan Aminoroayaye yamani: Conceptualization, Data curation, Formal analysis, Methodology, Software, Roles/Writing - original draft. **Mohammad Amin Barhamian:** Resources, Visualization, Roles/Writing - original draft, Writing - review & editing. **Ali Asghar Ghadimi :** Conceptualization, Formal analysis, Methodology, Supervision, Validation Roles/Writing.

Bibliography

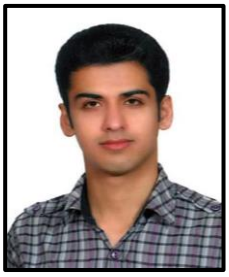

Seyed Ehsan Aminoroayaye yamani was born in 1989 in Isfahan, Iran. He received his B.Sc. and M.Sc. degrees in Electronics Engineering and Power Systems Engineering in 2009 and 2017, respectively, from Payam Golpayegan Institute of Higher Education, Golpayegan, Iran. He is currently an expert in the control and protection of power distribution and transmission networks in the companies affiliated to the regional electricity company of Isfahan province. His fields of interest are protection and control of power systems, microgrids, and renewable energies.

Mohammad Amin Bahramian received a B.Sc. degree in electrical engineering from Arak University, Arak, Iran, in 2020. He is now an M.Sc. graduate in electrical engineering from Arak University, having completed his degree in 2022. He also is currently employed at "Camellia Electronics Industry Innovators," a knowledge enterprise company, where he contributes to the field of power electronics, specializing in DC-DC converters and LED drivers. His research interests include Power Converters, Renewable Energy Systems, Smart Grid Technologies and Digital Control Systems.

Ali Asghar Ghadimi received his M.Sc. and Ph.D. degree in Power Engineering from Tehran Polytechnic University, Tehran, Iran in 2002 and 2008 respectively. He is currently Associate Professor and research member in Department of Electrical Engineering at Arak University, Arak, IRAN. His current research interests are in the area of Microgrid, Renewable Energy, and Power system optimal planning.

Journal of Green Energy Research and Innovation

Control and Improvement of Power Quality in Hybrid Three-Terminal AC/DC Microgrids

Mahdi Shiravand, Ali Nahavandi

Highlight

- **Presenting a synchronized power control technique for power sharing between power electronic converters**
- **Presenting a distributed cooperative control method for voltage and frequency control in AC MGs**
- **Providing voltage and current control in a DC MG for hybrid AC/DC MGs**
- **Performing both power control and power quality improvement of the AC/DC MG system**

Graphical Abstract

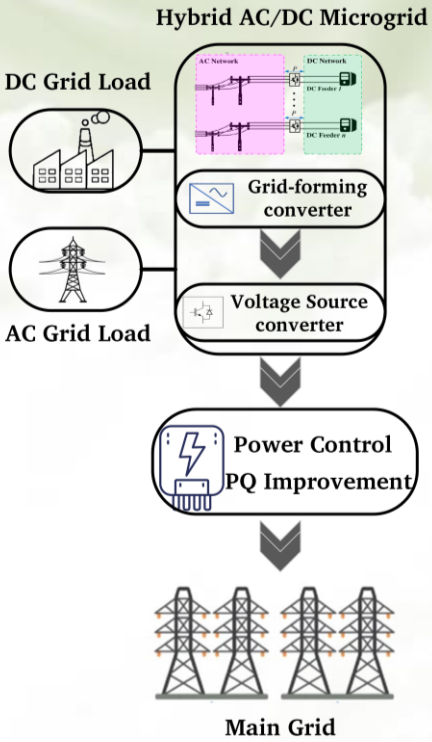

Use your device to scan and read the article online

Citation
M. Shiravand, and A. Nakabandi, "Control and Improvement of Power Quality in Hybrid Three-Terminal AC/DC Microgrids," *Journal of Green Energy Research and Innovation*, vol. 1, no. 2, pp. 31-45, 2024.

https://doi.org/10.61186/jgeri.1.2.31

Online ISSN: 3041-9018

Journal of Green Energy Research and Innovation

Journal Homepage: www.jgeri.araku.ac.ir

Control and Improvement of Power Quality in Hybrid Three-Terminal AC/DC Microgrids

Mahdi Shiravand, Ali Nahavandi*

Department of Electrical Engineering, Faculty of Engineering, Malayer University, Malayer, Iran.

* ***Corresponding Author:*** *ali.nahavandi@malayeru.ac.ir*

ARTICLE INFO

Keywords:
Renewable energy sources,
Power control,
Hybrid AC/DC microgrid,
Power quality.

Article history:
Received: 27 January 2024;
Revised: 27 February 2024;
Accepted: 02 March 2024;

Article type:
Research Article

ABSTRACT

Nowadays, the use of renewable energy sources has gained more attention due to their lower pollution and cost compared to traditional fossil fuel generators. Microgrid (MG) structures are used for better management of these resources. This article focuses on power control in three-terminal AC/DC hybrid MGs. For this purpose, a network backup converter is used to improve power sharing and reduce power quality disturbances. The components of the MG include distributed generation units, AC loads, DC loads, energy storage system (battery), and parallel connecting converters. In the studied topology of AC/DC hybrid MG in this article, there are two main converters: a grid-forming converter that acts as an intermediary converter and is used to control the MG voltage, and a VSC converter that is located between the DC link (including the DC MG and battery) and the AC MG. In this article, a control system is implemented for a hybrid MG and simulations are performed in MATLAB software for four different scenarios related to active and reactive power of the MG and loads. Simulation results show that the energy management system and power control in the AC/DC hybrid MG have reduced harmonics and improved system reliability in the MG.

1. Introduction

The utilization of distributed generation (DG), frequently employing renewable energies, is experiencing a significant surge in recent years, mostly driven by growing environmental and economic concerns. The introduction of the MG concept aims to maximize the utilization of DGs and address the issued arising from their integration into power systems. At first, MGs were classified into two categories: AC MG and DC MG. Each of these structures possesses distinct benefits and drawbacks. In AC MGs, AC sources like wind turbines can be directly linked to the MG [1]. However, it is more cost-effective and energy-efficient to link most renewable energy sources, such as photovoltaic (PV) sources and electrical energy storage sources, to the DC MG due to their DC output voltage. Furthermore, with DC MGs, concerns of frequency management and reactive power

control have been eradicated. To leverage the benefits of both forms of MGs, hybrid AC-DC MGs were established. These MGs allow for the simultaneous utilization of the advantages offered by both types. The use of hybrid AC-DC MGs is experiencing a remarkable growth in the present day due to their numerous advantages over other types of MGs [2]. The hybrid AC-DC MG involves the interconnection of AC and DC MGs through bidirectional AC/DC converters, also known as interface converters. Hence, the primary converter holds significant importance in hybrid AC-DC MGs. The primary function of this converter is to facilitate the exchange of power between AC and DC MGs in both directions. Additionally, it is responsible for stabilizing the voltage in the DC MG and controlling the voltage and frequency in the AC MG to maintain them close to their desired values. In conventional configurations, AC MGs are directly linked to the AC grid transformer, while DC MGs are connected to AC MGs via one or more parallel inverters [3]. The prevailing configuration of the interface converter is the three-phase, two-level, common inverter. In this structure, several converters are usually used in parallel to improve control capability, increase power transfer capacity, and enhance reliability. In these conditions, the issues of circulating current and power sharing among parallel converters arise, leading to reduced stability, decreased power transfer capacity, and increased energy losses [4]. Alternative configurations for interface converters exist; but, the majority of these configurations exhibit significant drawbacks, as outlined in [5] and described below. AC MGs are directly connected to the AC grid and voltage and frequency fluctuations in the grid affect the power quality of the AC MG. In addition, harmonics generated by nonlinear loads in the AC MG are injected directly into the main grid [6]. The growing trend of consolidating DGs in MGs [7], along with the rising need for medium-voltage and low-voltage DC MGs, has led to increased focus on hybrid multi-terminal MGs. The aim of this paper is to propose a structure for hybrid AC-DC MGs that can isolate MGs from the main grid, provide complete power control between MGs and the main grid, prevent harmful harmonics from being injected into the main grid, increase control flexibility between MGs and the main grid, and enable operation in both grid-connected and islanded modes. Furthermore, a well-suited control configuration is devised for the new MG to guarantee its stable functioning in diverse settings [8]. A back-to-back converter is employed in [9] to regulate the power exchange among many interconnected AC-DC MGs. A back-to-back converter is a configuration where the DC sections of two inverters are interconnected. The same research employs hierarchical distributed coordinated control to regulate both AC and DC MGs. Additionally, a proposed internal control approach is offered for the utilization of back-to-back converters and power sharing among MGs. The suggested control mechanism is specifically developed to enhance the power quality in MGs. Telecommunication lines are incorporated to establish connections between MGs in this context. The benefits of this effort include the consistent online availability of these links, while the drawbacks encompass the potential for delays and disruptions. The solution in [10] aims to minimize power conversion steps and deliver DC energy at various voltage levels. It introduces a four-terminal configuration for hybrid AC-DC MGs. The proposed structure includes a modular multilevel converter as the main intermediate

converter between the medium-voltage AC terminal and the medium-voltage DC terminal, and a DAB (Dual-Active Bridge) between the low-voltage DC terminals. The advantages of this work include improved energy control and reduced switches. However, a drawback is the omission of any discussion on the AC MG. In reference [11], an integrated and switchable design for hybrid AC-DC MG and a hierarchical control method is suggested for it. A new structure for interface converter is presented, which is called smart connection unit, and it can provide multiple AC/DC connection. In the following, a hierarchical control structure is designed for the smart connection unit. In [12], a simpler and more flexible structure for hybrid MGs is proposed, which includes an interface converter with several output ports. By using this structure, the number of power converters required in hybrid MGs with different DC voltage levels is reduced, and at the same time, the control flexibility of the MG does not decrease. Reference [13] discusses the improvement of power quality in hybrid AC/DC MG. In this article, by using the control of the converter between the two AC and DC sides, in addition to the power transfer between the two MGs, the harmonics due to the nonlinear load on the AC side are also reduced. In fact, the DC converter and MG act as filters, which improves power quality by removing nonlinear load harmonics. In reference [14], the hierarchical control structure, including internal, primary and secondary control levels, is introduced for hybrid MG control. The internal control is used to adjust the output voltage of the inverter. The primary control is based on the droop control. The secondary control compensates the voltage difference of the MG which is caused by the primary control so that the voltage between the MG and the main grid are completely synchronous and consistent. The MG can work well with the same control schematic that is proposed in two grid-connected and islanded modes. In reference [15], a modified structure is presented for interface converter of the hybrid AC-DC MG. In the proposed structure, energy storage is used in the interface converter. Also, in this article, an energy management strategy is presented that improves the quality of MG power. The interface converter suggested in this work includes two parallel three phase inverters, one of which is connected to the AC grid through a transformer and directly to the DC grid. The second inverter is directly connected to the AC grid, but its DC side is connected to a storage device and is linked to the DC grid via a bridge converter. Reference [16] discusses the establishment and management of a hybrid MG in the context of fluctuating renewables. The decentralized control of converters enables the independent operation and coordination of all renewable sources without the need for communication between them. The suggested control allows it to function as an active power filter besides its power sharing operation. A harmonic compensation approach suitable for hybrid AC-DC ILCs operating at lower switching frequency is being planned [17]. The text covers the proposed approach, methods for modeling, study of stability, and a comprehensive design of virtual impedance. A unique control technique is introduced in [18] to enhance the power quality of renewables, including PV, wind turbine (WT), fuel cell (FC), and battery. The primary objective is to improve power quality by considering variations in both active and reactive power. Literature [19] suggest a transformation method that combines AC and DC MGs and electric car operation. This technique aims to

improve power quality and power reliability operation. The objective of [20] is to analyze the harmonic characteristics of hybrid MGs. In order to attain the intended objective, a customized active power filter and a power filter compensator kit modules have been employed to enhance the harmonics of the AC component of the system. In accordance with reference [21], a solitary MG is constructed utilizing PVs, WTs, and FCs as distributed energy resources. An investigation has been conducted on a controller in this MG to ensure that power quality issues are kept within the specified standard range. The controller's performance is evaluated by comparing it to PID and fuzzy-PID controllers.

2. The structure of the hybrid AC/DC MG and converters

The present study examines a hybrid AC/DC MG configuration that includes DGs, electrical loads, energy storage, and the main grid. Figure 1 depicts the arrangement of the hybrid AC/DC MG, including all the mentioned components.

As can be seen, in one side of the MG, DC sources and DC loads are placed, while AC sources and AC loads are located on the other side. Furthermore, the part on AC loads includes the modeling of nonlinear and harmonic loads. The main grid is interconnected with the MG, and the system also incorporates electric energy storage. The benefit of this configuration lies in the isolation of vulnerable AC MG loads in the grid-connected mode. This research examines a hybrid AC/DC microgrid topology where DGs utilize grid-fed converters functioning as maximum power point tracking (MPPT)-controlled current sources. The grid forming converter is an interlinking converter (ILC), which is used for regulating the voltage of the MG. Two network backup converters are used to enhance power sharing and minimize power quality disruptions. The ILC model is represented in the dq reference frame and is characterized as follows.

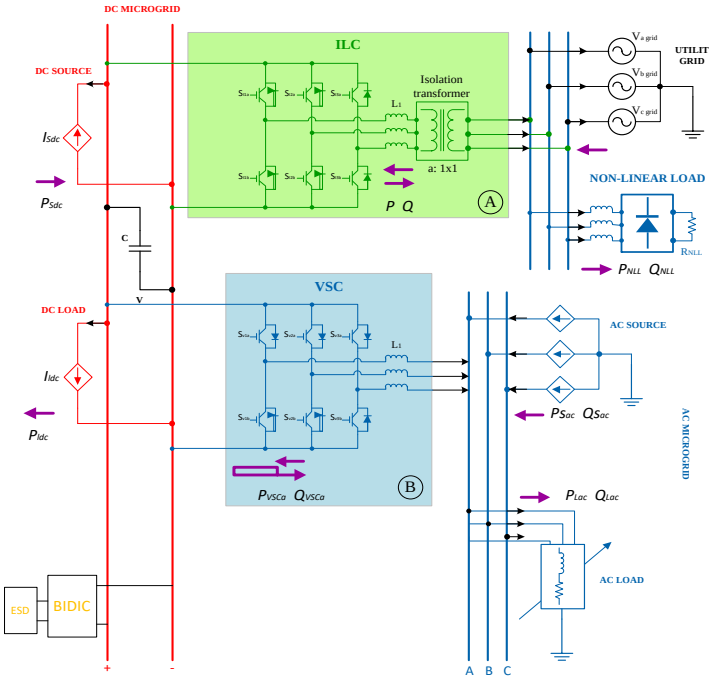

Figure 1. Structure of the hybrid MG under study.

A. ILC interface converter: The converter depicted in Figure 1 is a VSC that is linked to the main grid and a harmonic nonlinear load via a series inductor. The DC-link voltage is controlled, enabling the interconnection of DC sources and loads. Thus, the responsibility for power control between AC and DC MGs lies with ILC [15]. The ILC model is defined in the dq reference frame and is represented by Equations (1)-(2).

$$\begin{cases} L_i \dfrac{d}{dt} i_{id} = v_{id} - R_i i_{id} + L_i \omega_i i_{iq} - v_{sd} \\ L_i \dfrac{d}{dt} i_{iq} = v_{iq} - R_i i_{iq} + L_i \omega_i i_{id} - v_{sq} \end{cases} \quad (1)$$

$$\frac{C_{DCMG}}{2} \frac{dV_{DC}^2}{dt} = P_{ilcin} - P_{losses} - P_{ilcout} \quad (2)$$

where i_{id} and i_{iq} are d- and q-axes currents of the converter, and v_{id} and v_{iq} are voltages of the d- and q-axes. L_i and R_i are inductance and resistance of the filter L. Also, ω_i is the angular frequency of the ICL, and v_{sd} and v_{sq} are voltages of the d- and q-axes. C_{DCMG} represents the DC-link capacitor, V_{DC} is voltage of the DC link, P_{ilcin} and P_{ilcout} are the input and output power of the converter, and P_{losses} expresses the power loss in the converter. By applying the Laplace transform to Equations (1)-(2), and by considering only state variables, Equations (3)-(4) are established:

$$G_{cilc}(s) = \frac{I_{id}}{m_{id}} = \frac{I_{iq}}{m_{iq}} = \frac{1}{L_i s + R_i} \quad (3)$$

$$G_{vilc}(s) = \frac{V_{dc}^2}{P_{REF_{ilc}}} == \frac{2}{C_{DCMG} s_i} \quad (4)$$

m_{id} and m_{iq} are modulation indices of the ILC in the dq reference frame, and P_{refilc} is the reference power of the ICL.

B. VSC: Figure 1 illustrates the placement of this converter, which is positioned between the DC link (comprising the DC MG and battery) and the AC MG. The VSC modeling shares similarities with ILC, as both include VSCs equipped with L-filters [15].

3. Control block of the ILC converter

The ILC facilitates the two-way flow of electrical current between a DC MG and an AC grid. The ILC is driven by two control loops. The internal loop controls the electric current flowing through the L filter, whilst the external loop has control on the voltage across the DC-link capacitors. Figure 2 depicts the control design for the ILC. Part A in Figure 2 illustrates the Park transform alongside the use of a PLL to synchronize the ILC with the grid. To do this, the Park transform utilizes the three-phase voltages and currents obtained from the point of common connection (PCC) as its input. However, it is crucial that the synchronous angle created by the synchronous reference frame phase-locked loop (SRF-PLL) is also provided.

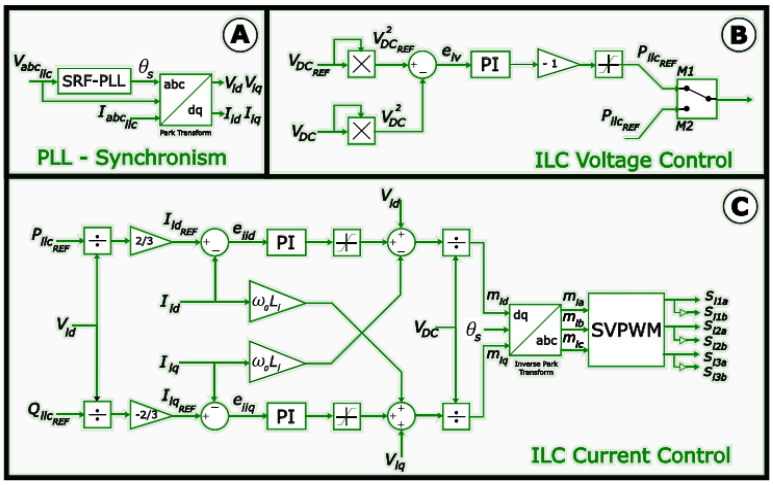

Figure 2. Control block of the ILC.

The voltage controller, seen in detail B of Figure 2, calculates the discrepancy between the squared reference voltage and the measured voltage in the DC link. This discrepancy is then utilized as the input for the proportional-integral (PI) controller. During operation in M_1 mode, the reference voltage loop is responsible for generating the reference power for the current loop. However, in M_2 mode, the reference power is obtained directly without any voltage control. The reference current for the dq axis is produced based on the relationships between the reference active and reactive power as given in Equations (5)-(6):

$$I_{dREF} = \frac{2}{3}\frac{P_{REF}}{V_d} \tag{5}$$

$$I_{qREF} = -\frac{2}{3}\frac{Q_{REF}}{V_d} \tag{6}$$

I_{dREF} and I_{qREF} represent the reference dq currents, while P_{REF} and Q_{REF} represent the reference active and reactive power, respectively. The formulae are same for both ILC and VSC converters. The current controller for the ILC is depicted in part C of Figure 2. The reference currents in the dq frame are determined by using the calculated reference active and reactive powers. The modulation indices are then generated through the use of PI controllers. Subsequently, the modulation indices in the dq reference frame yield the modulation indices in the abc frame, which serve as the inputs for the SVPWM and generate the ILC switching pulses. The primary objective of the ILC control strategy is to compensate the reactive power of the grid and share the active power using the droop control technique.

4. Control block of the VSC

The VSC is a power converter that links the AC MG to the energy storage device (ESD) and the DC MG, thus acting as a grid backup unit. VSC directly controls the voltage and frequency of the AC MG. Figure 3 shows the block diagram of the control section of the VSC converter.

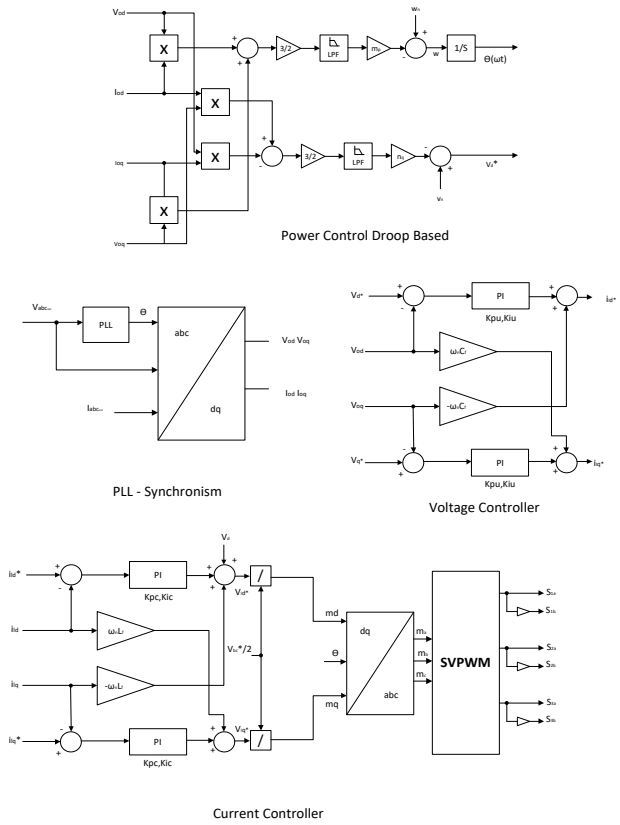

Figure 3. Control block of the VSC.

According to Figure 3, this converter, which is of grid-forming type, is used to regulate voltage and frequency to meet the voltage and frequency distribution requirements. W is obtained using the equation W=Wn-Mp(Pavr-Pn), and the reference voltage is obtained using the equation V=Vn-Nq(Qavr-Qn). To make the output voltage follow the reference value, first, the reference current must be obtained in the voltage control block. After obtaining the reference voltage, it is fed into the current control block, and the reference output voltage is obtained, and then switching is performed.

5. Simulation results

In this section, the structure presented in Figure 1 is implemented in MATLAB software, which includes AC and DC loads, AC and DC sources, an electrical energy storage device, and intermediate converters. The simulation system parameters in this study are listed in Table 1.

To examine the simulation results of the proposed AC/DC hybrid MG, scenarios presented in Table 2 are applied to the system. In Table 2 the P_{ACMG} is power of AC microgrid and P_{DCMG} is power of DC microgrid that each one can have positive value or negative value. If P_{ACMG} is positive value, the AC microgrid will deliver active power to grid and if the P_{ACMG} is negative, the AC microgrid will consume active power. Also, there will be similar condition for DC microgrid. Figure 4 illustrates the power curves of the AC MG, DC MG, grid, and storage for different scenarios.

During the time interval t= 0 to t=1 s, the entire power of the grid is transmitted to the AC MG through the VSC associated with the AC MG. Here, the AC MG has a power consumption of -2 kW. Approximately 10% of the power is derived from the battery, while the other portion is supplied from the AC grid. The goal of droop control is to modify these ratios by either decreasing or increasing the droop control coefficient. DC and AC MGs rapidly produce electricity within a timeframe of 1 to 2 s and supply it to the main grid.

Table 1. Simulation parameters.

Parameter	Value
Parameters of converters	
C_{DCMG} (µF)	2250
C_{BESS} (µF)	1125
L_i(mH)	5
L_v(mH)	10
L_b(mH)	10
R_{int}(Ω)	0.1
Rated values	
f_n (Hz)	50
Vdc_{ref} (V)	900
Vn_{rms}(V)	220
P_n(W)	4500
ESD	
E_{0b}(V)	3.366
R_{bat}(Ω)	0.01
SOC_0	0.5

Table 2. Performance conditions of sources and loads at different times.

Scenario	1	2	3	4
Time duration (s)	1-2	2-3	3-4	4-5
Conditions	$P_{ACMG} > 0$ $P_{DCMG} > 0$	$P_{ACMG} > 0$ $P_{DCMG} < 0$	$P_{ACMG} < 0$ $P_{DCMG} < 0$	$P_{ACMG} < 0$ $P_{DCMG} > 0$

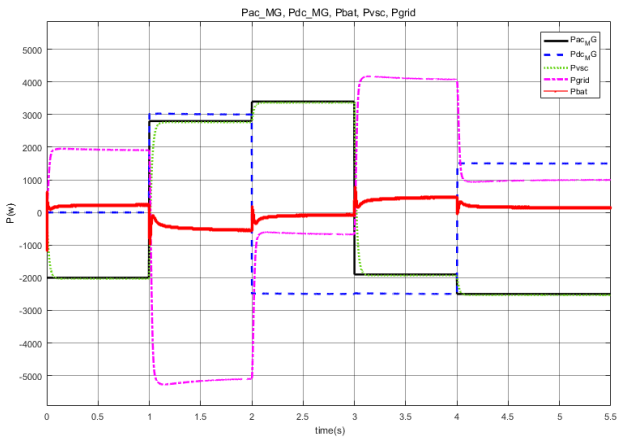

Figure 4. Active power curves of AC and DC MGs, the grid, and the storage.

In this case, excess power is stored in the storage. The AC MG transfers power to both the main grid and the DC MG within a time t=2s to t=3 s using the VSC. In fact, in this case, the DC MG also has a power shortage. From t=3s to t=4s, both DC and AC MGs have a power shortage, and this power is compensated through the main grid. It should be noted that some of this power is supplied by discharging the battery. During t=4s to t=5s, the AC MG has a power shortage that is compensated through the main grid and the DC MG. In this case, the battery is in discharge mode.

To examine the performance of converters in this situation, it is necessary to study the system's reactive power curve. Figure 5 shows the reactive power curve of the main grid, VSC converter related to the AC MG, and ILC intermediate converter.

The presence of fixed capacitors in the grid results in a constant reactive power curve of 4500 Var. However, the reactive power curve of the ILC is zero, indicating that no reactive power is transferred through this converter. It means that just VSC is capable of grid transferring reactive power in various scenarios, depending on the MG's reactive power demand and the loads that are accessible. Figure 6 displays the voltage curve of the DC link and its association with droop control.

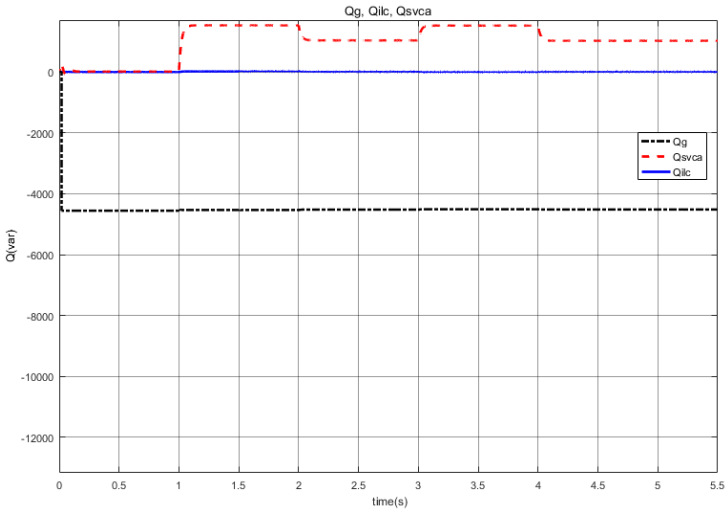

Figure 5. Reactive power curves of the main grid, the VSC of AC MG, and the ILC.

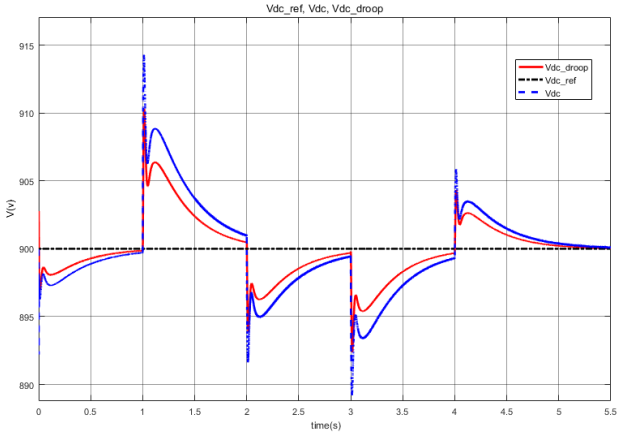

Figure 6. Voltage curve of the DC link and droop control DC-link.

Assuming proper functioning of the energy management system and controllers in the hybrid AC/DC MG system, the DC-link voltage is expected to consistently track the reference voltage value of 900 V across various conditions and scenarios. By altering the loads and system conditions at various instances, it is evident that the DC-link voltage deviates from its reference value. This deviation, whether a drop or a rise, remains within a margin of less than 2%. Furthermore, the voltage curves promptly align with the reference value. Figure 7 displays the current curve of the grid, the nonlinear load, and the ILC. The system's current fluctuates in various settings and conditions, corresponding to variations in both DC and AC demands.

The nonlinear load current curve in Figure 7 shows that the load enters the system at t=1s and becomes harmonic from that moment on. Figure 8 displays the gri current curve, nonlinear load, and ILC converter at the time of the entry of the nonlinear load at t=1s. As observed, before the entry of the nonlinear load into the system, the grid current curve is completely sinusoidal and without distortion, but with the entry of the nonlinear load, the curve becomes distorted.

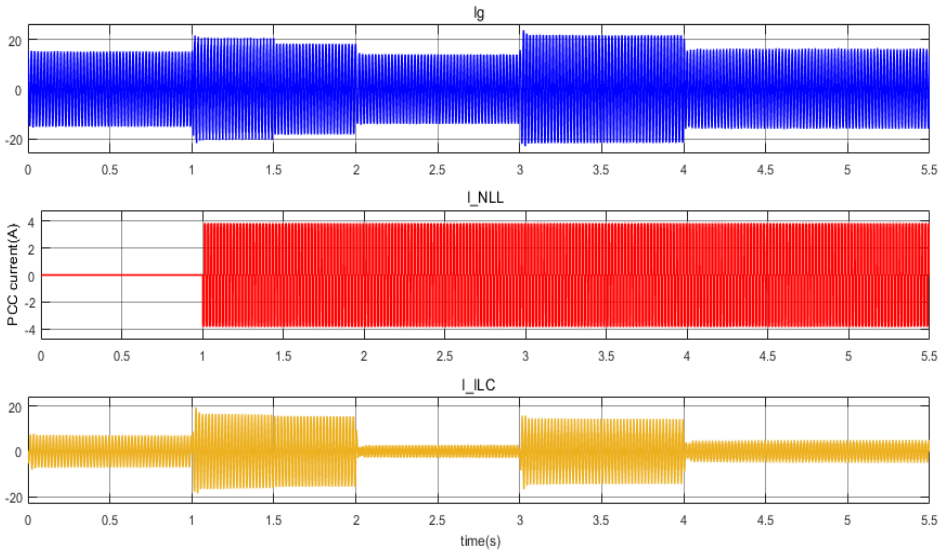

Figure 7. Current curves of the gird, the nonlinear load, and the ILC.

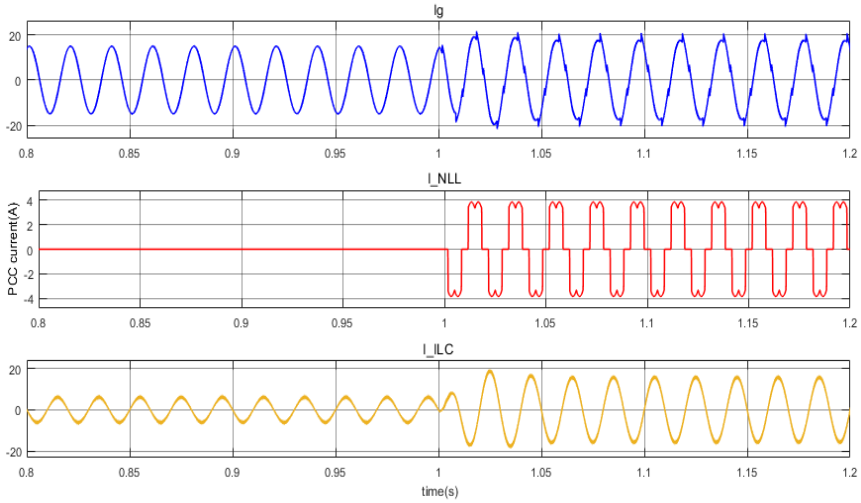

Figure 8. Current curves of the gird, the nonlinear load, and the ILC when the nonlinear load is introduced.

Figure 9 shows the grid current curve, nonlinear load, and ILC converter at the time of operation of the harmonic control section at t= 1.5s. As observed, the control system operates well from 1.5s onwards and the grid current curve becomes undistorted.

It should be noted that harmonic compensation is done through the ILC converter, and for this reason, after 1.5 seconds, the current curve of the ILC intermediate converter is affected by harmonics to avoid having a harmonic grid current curve. To evaluate the level of distortion, FFT analysis available in Matlab is used to calculate the THD level. Figure 10 shows the level of harmonic and distortion in the grid current when there is no nonlinear load present in the grid, and the THD value is 1.91%, which is low and acceptable.

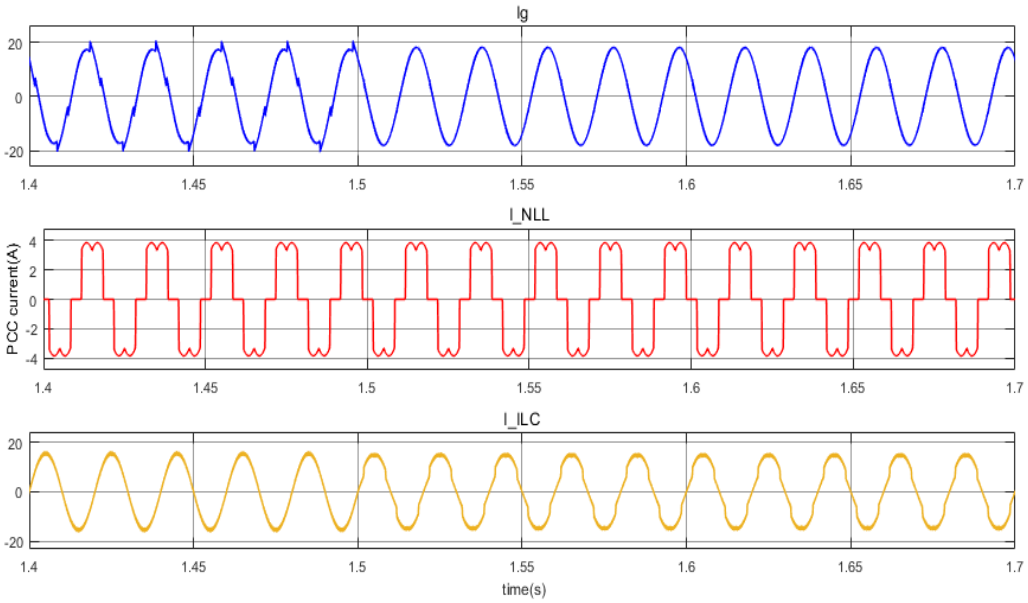

Figure 9. Current curves of the gird, the nonlinear load, and the ILC when the harmonic-generator control block operates.

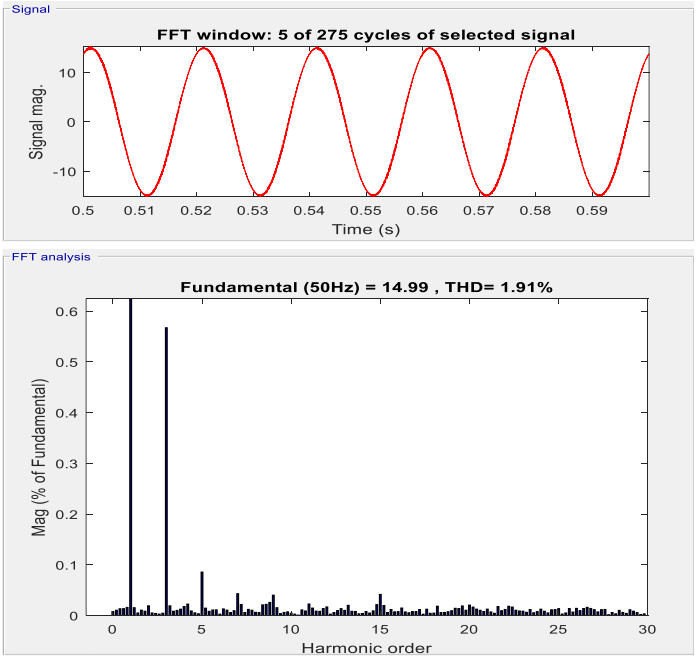

Figure 10. Harmonic and distortion levels of the grid current in the absence of the nonlinear load.

At t = 1 s, a load with both harmonic and nonlinear characteristics is introduced into the system. Figure 11 illustrates the level of harmonic and distortion in the grid current when the nonlinear and harmonic load is applied. In this case, the THD level of the grid current is 7%, which is higher than the standard value. Therefore, it is necessary to reduce the level of distortion. After the implementation of the control block related to harmonic compensation in the hybrid AC/DC MG, the THD level returns to its original value and even less than that. Figure 12 shows the level of harmonics and grid current distortion during the operation of the control and harmonic compensation section, with the THD level being about 1.87% and even less than the initial value.

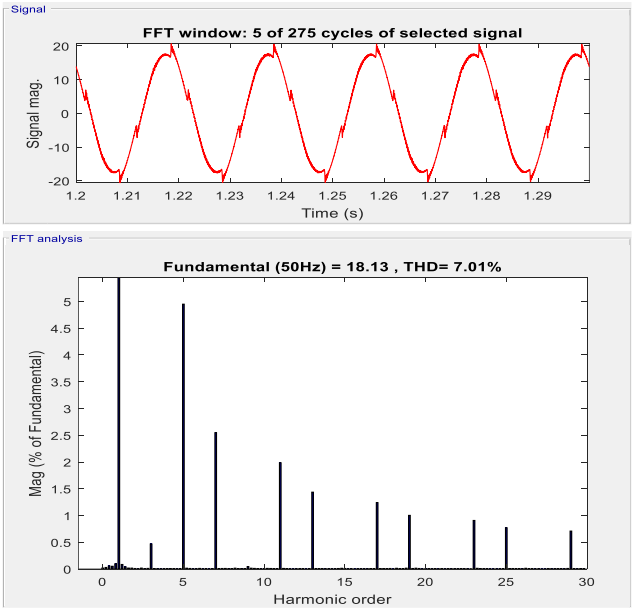

Figure 11. Harmonic and distortion levels of the grid current when the nonlinear, harmonic-generator load is introduced.

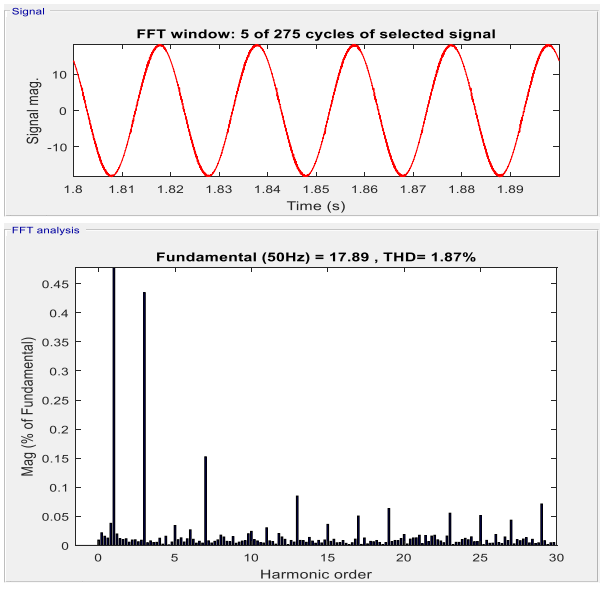

Figure 12. Harmonic and distortion levels of the grid current during the operation of the control block and harmonic compensator.

Therefore, the energy management system, power control, and the section aimed at improving power quality and reducing harmonics in the combined AC/DC MG have performed well under all conditions. Consequently, the proposed structure in this study has shown very good performance.

6. Conclusion

Hybrid AC/DC MGs have been designed for better integration of various DG resources with the power grid and to utilize the features of both AC and DC MGs. To establish the connection between these MGs, an interface converter equipped with a suitable power management and control scheme is required. To control frequency and voltage in the AC MG, the voltage in the DC MG must be adjusted and the power must be effectively managed and controlled based on the capacity of each MG. Therefore, it is essential to develop a suitable method for energy supervision in the hybrid AC/DC MG. In this paper, a novel architecture and a suitable control method for hybrid AC/DC MGs were presented. Also, a synchronized power control technique for power sharing between the power electronic converters is presented. In addition, a distributed cooperative control method for voltage and frequency control in AC MG and voltage and current control in DC MG for hybrid AC/DC MG was presented. The research investigated a hybrid AC/DC MG topology in which DGs utilize grid-forming converters. The grid-forming converter is an ILC used to control the MG voltage. Two grid-forming converters were used to boost the capability of power sharing and minimize power quality disturbances. Overall, the results indicate that both the power control and power quality improvement components of the AC/DC MG system work effectively under all conditions. Consequently, the structure described in this paper shows excellent performance. It should be noted that in this article, the AC MG is isolated from the main grid, and therefore sensitive loads are isolated from main grid faults and are not affected by them.

References

[1] M. Abasi, M. F. Nezhadnaeini, M. Karimi, and N. Yousefi, "A Novel Metaheuristic Approach to Solve Unit Commitment Problem in the Presence of Wind Farms," *Rev Roumaine des Sciences Techniques-Series Electrotechnique et Energetique,* vol. 60, no. 3, pp. 253- 262, 2015.

[2] M. Eidiani, and M. Kargar, "Frequency and Voltage Stability of the Microgrid with the Penetration of Renewable Sources, " *9th Iranian Conference on Renewable Energy & Distributed Generation (ICREDG)*, IEEE, 2022.

[3] S. Muchande, and S. Thale, "Hierarchical Control of a Low Voltage DC Microgrid with Coordinated Power Management Strategies," *Engineering, Technology & Applied Science Research*, vol. 12, no. 1, pp. 8045-8052, 2022.

[4] M. Abasi, M. Joorabian, A. Saffarian, and S. G. Seifossadat, "A Comprehensive Review of Various Fault Location Methods for Transmission Lines Compensated by FACTS Devices and Series Capacitors," *Journal of Operation and Automation in Power Engineering*, vol. 9, no. 3, pp. 213-225, 2021.

[5] A. Aldosary, M. Rawa, et al., "Energy Management Strategy Based on Short-Term Resource Scheduling of a Renewable Energy-Based Microgrid in the Presence of Electric Vehicles Using θ-Modified Krill Herd Algorithm," *Neural Computing and Applications*, vol. 33, no. 16, pp. 10005-10020, 2021.

[6] S. Jena, and N. P. Padhy, "Distributed Cooperative Control for Autonomous Hybrid AC/DC Microgrid Clusters Interconnected via Back-to-Back Converter Control," *IEEE Power & Energy Society General Meeting (PESGM)*, pp. 1-5, IEEE, 2020.

[7] M. Sadeghi, and M. Abasi, "Optimal Placement and Sizing of Hybrid Superconducting Fault Current Limiter for Protection Coordination Restoration of the Distribution Grids in the Presence of Simultaneous Distributed Generation," *Electric Power Systems Research*, vol. 201, 107541, 2021.

[8] Z. Li, Z. Cheng, et al., "Hierarchical Control of Parallel Voltage Source Inverters in AC Microgrids," *The Journal of Engineering*, vol. 2019, no. 16, pp. 1149-1152, 2019.

[9] X. Hou, Y. Sun, et al., "Distributed Hierarchical Control of AC Microgrid Operating in Grid Connected, Islanded and Their Transition Modes," *IEEE Access*, vol. 6, pp. 77388-77401, 2018.

[10] Q. Xiao, Y. Mu, et al., "Modular Multilevel Converter Based Multi-Terminal Hybrid AC/DC Microgrid with Improved Energy Control Method," *Applied Energy*, vol. 282, 116154, 2021.

[11] H. Yu, S. Niu, Y. Zhang, and L. Jian, "An Integrated and Reconfigurable Hybrid AC/DC Microgrid Architecture with Autonomous Power Flow Control for Nearly/Net Zero Energy Buildings," *Applied Energy*, vol. 263, 114610, 2020.

[12] J. Khodabakhsh, and G. Moschopoulos, "Simplified Hybrid AC-DC Microgrid with a Novel Interlinking Converter," *IEEE Transactions on Industry Applications*, vol. 56, no. 5, pp. 5023-5034, 2020.

[13] M. Khederzadeh, and M. Sadeghi, "Virtual Active Power Filter: A Notable Feature for Hybrid AC/DC Microgrids," *IET Generation, Transmission & Distribution*, vol. 10, no. 14, pp. 3539-3546, 2016.

[14] I. Ziouani, D. Boukhetala, et al., "Hierarchical Control for Flexible Microgrid Based on Three-Phase Voltage Source Inverters Operated in Parallel," *International Journal of Electrical Power & Energy Systems,* vol. 95, pp. 188-201, 2018.

[15] J. P. C. Silveira, P.J. dos Santos Neto, T.A. dos Santos Barros, and E. Ruppert Filho, "Power Management of Energy Storage System with Modified Interlinking Converters Topology in Hybrid AC/DC Microgrid," *International Journal of Electrical Power & Energy Systems*, vol. 130, 106880, 2021.

[16] J. Jayaram, M. Srinivasan, N. Prabaharan, and T. Senjyu, "Design of Decentralized Hybrid Microgrid Integrating Multiple Renewable Energy Sources with Power Quality Improvement," *Sustainability*, vol. 14, no. 13, 7777, 2022.

[17] S. R. Das, A. K. Mishra, P. K. Ray, S. R. Salkuti, and S. C. Kim, "Application of Artificial Intelligent Techniques for Power Quality Improvement in Hybrid Microgrid System," *Electronics*, vol. 11, no. 22, 3826, 2022.

[18] P. Rajesh, F. H. Shajin, B. Rajani, and D. Sharma, "An Optimal Hybrid Control Scheme to Achieve Power Quality Enhancement in Micro Grid Connected System," *International Journal of Numerical Modelling: Electronic Networks, Devices and Fields*, vol. 35, no. 6, 2022.

[19] B. Sahoo, S. K. Routray, P. K. Rout, and M. M. Alhaider, "Power Quality and Stability Assessment of Hybrid Microgrid and Electric Vehicle through a Novel Transformation Technique, " *Sustainable Energy Technologies and Assessments*, vol. 51, 101927, 2022.

[20] N. Khosravi, S. Echalih, et al., "Enhancement of Power Quality Issues for a Hybrid AC/DC Microgrid Based on Optimization Methods," *IET Renewable Power Generation*, vol. 16, no. 8, pp. 1773-1791, 2022.

[21] A. Satapathy, N. Nayak, and T. Parida, "Real-Time Power Quality Enhancement in a Hybrid Micro-Grid Using Nonlinear Autoregressive Neural Network," *Energies,* vol. 15, no. 23, 2022.

Declaration of Competing Interest

The authors declare that they have no known competing financial interests or personal relationships that could have appeared to influence the work reported in this paper. The ethical issues, including plagiarism, informed consent, misconduct, data fabrication and/or falsification, double publication and/or submission, redundancy, have been completely observed by the authors.

Credit Authorship Contribution Statement

Mehdi Shiravand: Conceptualization, Data curation, Formal analysis, Methodology, Software, Roles/Writing - original draft. **Ali Nahavandi :** Conceptualization, Formal analysis, Methodology, Supervision, Validation Roles/Writing-original draft, Writing-review & editing.

Bibliography

Mehdi Shiravand was born in 1995 in Iran. He graduated with a bachelor's degree and a master's degree in electrical power engineering from Malayer University, Malayer, Iran in 2019 and 2023, respectively. His special interests are power electronics, distributed generation and renewable energies, and power quality evaluation.

Ali Nahavandi was born in Malayer, Iran, in 1983. He received the B.Sc., M.Sc. and Ph.D. degrees in electrical power engineering from University of Tabriz, Tabriz, Iran, in 2006, 2008 and 2014 respectively. Since 2014 he is assistant professor in Faculty of Engineering, Malayer University, Malayer, Iran. His research interests include power electronic converters, renewable energy systems and power quality.

Journal of Green Energy Research and Innovation

Frequency Stabilizing and Reducing Power Outages of The Islanded Power Network Using a Load Shedding Method in The Presence of Renewable Energy Resources

Reza Eslami

Highlight

- Introduction of a novel load shedding strategy for microgrids
- Aiming to stabilize frequency and minimize power outages
- Implementation of load shedding in islanded power networks with renewable energy sources
- The proposed method's benefits include flexibility, rapid response, and precision

Graphical Abstract

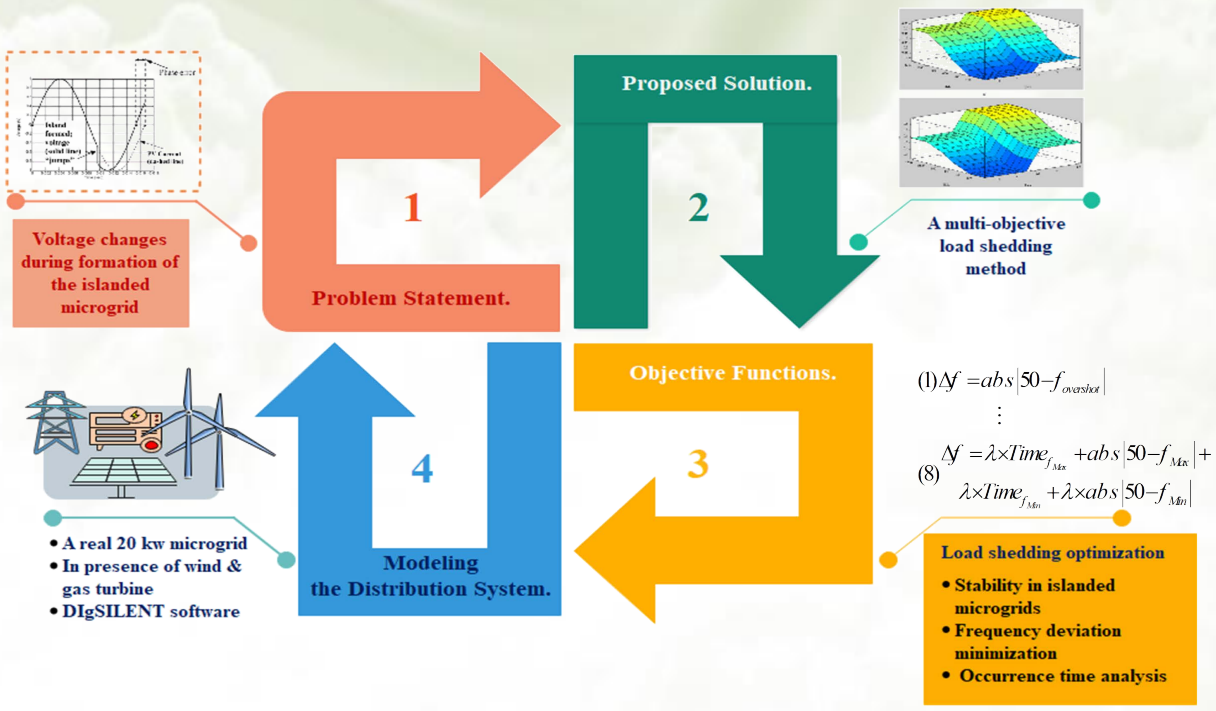

Use your device to scan and read the article online

Citation

R. Eslami, "Frequency Stabilizing and Reducing Power Outages of The Islanded Power Network Using a Load Shedding Method in The Presence of Renewable Energy Resources," *Journal of Green Energy Research and Innovation*, vol. 1, no. 2, pp. 46-63, 2024.

https://doi.org/10.61186/jgeri.1.2.46

JGERI Journal of Green Energy Research and Innovation

Online ISSN: 3041-9018

Journal of Green Energy Research and Innovation

Journal Homepage: www.jgeri.araku.ac.ir

Frequency Stabilizing and Reducing Power Outages of The Islanded Power Network Using a Load Shedding Method in The Presence of Renewable Energy Resources

Reza Eslami *

Electrical Engineering Faculty, Sahand University of Technology, Tabriz, Iran.

* ***Corresponding Author:*** *eslami@sut.ac.ir*

ARTICLE INFO

Keywords:
Renewable energy resources,
Power outages,
Load shedding,
Stability of the frequency,
The islanded microgrid.

Article history:
Received: 15 February 2024;
Revised: 05 March 2024;
Accepted: 28 March 2024;

Article type:
Research Article

ABSTRACT

Controlling the frequency and voltage of the power network with renewable energy resources is one of the most important things in the integrity of the network. Therefore, after occurring any accident or fault in the network, the frequency and voltage and in general all the basic parameters of the network must return to their acceptable range within a certain period of time. Despite all the technical, economic and environmental advantages that renewable energy resources have, the presence of these kind of sources may have negative effects on voltage profiles and protection coordination in distribution networks, it is also possible that a part of the network acts as an unwanted island, which complicates the operation and control of the network and creates a risk of electrocution for the network personnel. Therefore, islanding detection is very important and necessary in network protection and load shedding methods are usually used to eliminate this event. In this paper, a multi-objective load shedding method in microgrids is proposed for the frequency stability and reduction of power outages. Among the advantages of the proposed method can be mentioned its flexibility, speed of operation and high accuracy. The proposed method is applied and simulated on a microgrid in the DIgSILENT software environment, and the results of the simulation confirm the advantages of the proposed method.

1. Introduction

In the field of electricity industry, a massive evolution has taken place in the energy generation and transmission systems in most developed countries, which have several advantages in technical and economical cases of generation and transmission grids. This new energy generation system is called distributed generations (DGs) [1, 2].

Despite all benefits of DGs, the presence of DGs may have negative effects on voltage profiles and protection coordination in the distribution grids, so the operation and control of the grid becomes more complicated [3, 4]. Connection of DGs to the grid creates harmonics and reduces the short-circuit impedance. Additionally, it can be dangerous for grid repairmen if grid-connected DGs work as an island during outages. Islanding means wanted or unwanted disconnection of a part of the distribution system from the main

power source [5]. Figure 1 shows voltage variations during islanding. The control of the grid frequency and voltage is one of the most important cases in the integrity of the grid. Therefore, the frequency and voltage and, in general, all the basic parameters of the grid should return to their acceptable state within a certain period of time (after the occurrence of an emergency condition). Load shedding is one of the common methods to control the grid emergency states. Many studies in the field of load shedding have been made in recent years. The scheme presented in [6] was not suitable for the system protection.

In the mentioned study, load shedding strategy was considered based on voltage and frequency indices. In this strategy, load shedding was conducted outside the desired voltage and frequency range, according to the Q-V curve of the reactive power. Furthermore, the goal of this paper was to release the microgrid in the severe combined contingencies, where the rate of load shedding was not economically important. Reference [7] announced the operator's experience as the basis for load shedding and recommended the exact load model for better results. In this paper, the microgrid was divided into smaller islands and load shedding was performed based on the disturbance rate. In this method, the delay time of each step was assumed be of a larger value. So, this control method was inappropriate in low power microgrids, which should be stable in the shortest possible time and causes the disintegration of these microgrids. In [4, 8], speed and accuracy were introduced as the basic factors in sub-frequency load shedding to maintain the stability of the system and the use of SCADA system was presented to improve the deficiencies of adaptive protection model. As well, a static load shedding strategy was proposed in [9], in which a constant amount of load was cut off with reduction of frequency. In [10], a method was presented in the central control system to perform a fast load shedding, which was not applicable in the low power systems. In [11], difficulties of adaptive load shedding such as estimating the amplitude of the disturbance, cut-off positions and control actions by relays were introduced.

In another article, the author claimed that if there are several sources in the microgrid, it will be better to consider the result of frequency change rate graphs. In the Slovenian load shedding standard, four threshold frequency values were defined, in which the percentage of the load unplugged from the whole microgrid was defined for each threshold frequency with considering the disturbance rate. The mentioned article mostly

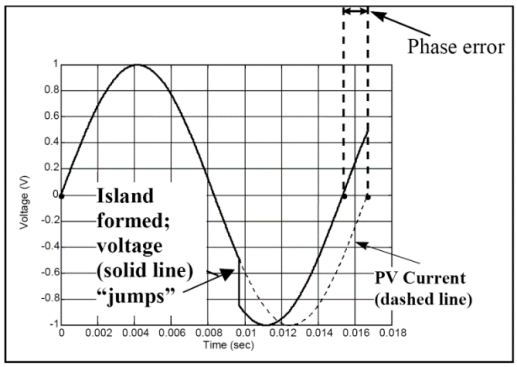

Figure 1. Voltage changes during formation of the islanded microgrid.

focused on correcting the coefficients of the cut off load percentage. This paper includes desirable results for high power systems; but it was not useful for low power systems [12]. In [13], the authors showed that, in one case out of five load shedding cases, a suitable response to power shortage could be achieved. Also, given that the slope (frequency change rate) lonely is not able to have a convincing response; the authors proposed the frequency change rate in terms of voltage. Ref. [14] fixed the grid frequency by ejecting additional loads and stabilized the grid by removing sensitive buses; however, it was analyzed only for grids containing two small hydro generators.

Moreover, [15] indicated that the concavity in the frequency of load shedding could be determined. But big disturbances led to a decline in the system frequency and the buses voltage was dependent on the shortage of active and reactive powers or it related to information of the generation inter-load unbalancing. In [16], the frequency change rate was used to estimate the amplitude of disturbance and the voltage change rate corresponding to the reactive power was used to identify the buses, which required load shedding. To calculate the change rate of frequency and voltage, using devices such as numerical stability or phase measurement units or methods such as Kalman filter to estimate the parameters was proposed. This method conferred good results; however, in modern microgrids, at least in low power systems, loads are frequently prioritized and it cannot be said that load shedding should be conducted according to the priority system conditions [16].

In [17], a new adaptive load shedding is presented, which prevents the large reduction of frequency in the emergency situations and minimizes the line overload. Size and position of disturbance in decentralized models were not known, so disturbance rate was related to the frequency change rate and inertia constant and frequency local change was related to the disturbance position. As a result, an attempt was made to optimize the threshold frequency value using these cases in this study. Then by averaging the microgrid frequency graph (total regions in the microgrid), if average of the microgrid frequency was less than threshold frequency value, then load shedding was conducted. In [18], in addition to frequency stability, the voltage stability was also considered and swing equation and telecommunication systems were used respectively to calculate the amplitude of the disturbance and transmit information. In this method, choosing small sampling time (the information sampling time to transmit) created some problems such as aberration in the frequency natural fluctuations. Also, telecommunication systems were not able to transmit the information in a short time. A relay was proposed for each station in this method. These relays implement load shedding program based on voltage level of certain buses in case of frequency change. And those buses were which reached below the threshold. The cost was not a criterion in this paper and only technical aspect was discussed.

According to [19], when the microgrid frequency reduced to a value less than the threshold frequency, load shedding was conducted according to frequency change rate. A try was made in this article to correct the threshold frequency. But it faced to the problem of normal frequency fluctuations at frequencies close to the normal frequency. So, in the

mentioned article, a phase control loop was used to solve this problem and to choose the exact frequency. Moreover, six steps with six different threshold frequencies were considered for load shedding. Another load shedding strategy was based on online load measurement and frequency-load curve. But real-time load information was not always available and online load measurement was expensive for small distribution systems. Furthermore, determining frequency-load dependence of the system is often difficult. In the adaptive load shedding strategy, the relay regulation was changed with the frequency collapse curve [20], which was determined based on the frequency information of the amount of the ejected load [21]. Adaptive load shedding strategy required real time data of loads and generations and also, that was difficult to determine the microgrid inertia. The issues mentioned above were for the microgrid containing generation sources at the scale of large power plants. In [22], load shedding of the islanded microgrid, which is supplied by low-power DGs was discussed. The load shedding of the islanded distribution system should be different from high power systems due to different specifications. Most generators have small inertia in the islanded distribution system, so the frequency tends to collapse faster.

2. The proposed method of load shedding in the islanded microgrid in the presence of distributed generation sources

2.1. Introducing the objective function of the paper

Load shedding with the presence of DGs is an optimization process, which is conducted for various goals. These goals enter the load shedding problem in the form of objective function parameters. Since the considered optimization problem in this paper is load shedding with the presence of DGs based on the stability and reliability factors in the sub-transmission substations. These factors will enter the objective function. so, the most important factor will enter the problem objective function. Then, by analyzing each of the objective functions and their upsides and weaknesses, the objective function could have better results was selected and the presented tables were used for each of these 8 objective functions.

2.2. Factors affecting the load shedding in the presence of distributed generation sources

The new method presented in this paper has the following steps to achieve the stability of the islanded microgrid in the shortest possible time:

- Creating a selection table based on the tendency-to-pay factor of each subscriber (formation of this table is done based on the presented method in study [22].)
- After providing the selection table and the load departure priority, by creating the 8 objective functions which are introduced in the following, a main project and 3 sub-project are written in DIgSILENT software in order to reduce the grid frequency drop, lessen the microgrid frequency overshoot and determine the times at which these frequencies will occur, and the objective functions are analyzed and the best function to attain the shortest possible time to achieve the

stability is selected. This is performed by linking two softwares, DIgSILENT and MATLAB, in which the genetic optimization algorithm is written.

In the following, the proposed load shedding strategy is analyzed, which covers the grid variables in the form of 8 objective functions.

❖ The first objective function:

As a first step, the following formulation is introduced to reduce the difference between the created maximum frequency and the base frequency:

$$\Delta f = abs\left|50 - f_{Overshoot}\right| \quad (1)$$

$f_{overshoot}$ in Equation (1) is the maximum frequency produced in the network due to creation of the islanded state.

❖ The second objective function:

The difference between the frequency and the base frequency can be minimized with the help of this objective function. In order to examine how effective this parameter is in achieving the above purposes, Equation (2) will be defined and analyzed separately.

$$\Delta f = abs\left|50 - f_{Min}\right| \quad (2)$$

❖ The third objective function:

One of the considered factors to achieve the suitable response is to analyze the maximum frequency created in the grid and also the minimum frequency created in the microgrid simultaneously. So, in this step, the best state is analyzed in which the minimum overshoot and the minimum frequency drop are achieved by interrupting the minimum load. Therefore, the objective function for this purpose is written in Equation (3).

$$\Delta f = abs\left|50 - f_{\min}\right| + abs\left|50 - f_{Overshot}\right| \quad (3)$$

❖ The fourth objective function:

The objective function given in Equation (4) is used to survey the occurrence time of the grid maximum frequency and the maximum frequency drop.

$$\Delta f = Time_{f_{\min}} + Time_{f_{\max}} \quad (4)$$

In this Equation, $Time_{f_{\min}}$ and $Time_{f_{\max}}$ are the times that the grid minimum and maximum frequency occur respectively.

❖ The fifth objective function:

One of important factors considered in this paper is the time that the maximum drop occurs in the grid. For this purpose, in the objective function given in Equation (5), in which the best time that the frequency drop is at its minimum value, is introduced. This optimal time is when the frequency drop is in its minimum value.

$$\Delta f = Time_{f_{\min}} \quad (5)$$

❖ The sixth objective function:

Simultaneous consideration of the maximum frequency occurred in the grid along with the time at which this frequency is created, is presented in another objective function that is specified by Equation (6). In this objective function, in order to equalize the limit of numbers, the factors are multiplied by a coefficient of λ, This weight coefficient shows the importance degree of factors from a design point of view.

$$\Delta f = \lambda \times Time_{f_{min}} + \lambda \times abs\left|50 - f_{min}\right| \quad (6)$$

In Equation (6), λ equals to *0.1*.

❖ The seventh objective function:

In order to analyze separately the time that the grid maximum frequency occurs along with the relevant time, another objective function is defined by considering the points made in the previous step.

$$\Delta f = \lambda \times Time_{f_{max}} + abs\left|50 - f_{max}\right| \quad (7)$$

❖ The eighth objective function:

In order to comprehensively review and compare different important scenarios, a new load shedding method was presented in this paper that covered all the load shedding goals mentioned in Equations (1) to (7). This general objective function is introduced in Equation (8). As it is shown in the simulation results, it certainly has higher flexibility, speed and accuracy.

$$\begin{aligned}\Delta f &= \lambda \times Time_{f_{max}} + abs\left|50 - f_{max}\right| \\ &+ \lambda \times Time_{f_{min}} + \lambda \times abs\left|50 - f_{min}\right|\end{aligned} \quad (8)$$

2.3. Modeling of the under-studying Distribution system

A 20 KW real microgrid owned by Himmerland Elforsynig Factory in Denmark has been selected for this study [23]. The single-line diagram of the distribution system is illustrated in Figure 2. In this microgrid, 11 radial feeders exist named JUEL, STK1, HJOR, FLOE, REBD, MAST, STCE, SORP, STNO, STKV, STSY. A CHP (Combined Heat and Power) power plant with 3 gas turbine generators exists in the STKV feeder. Also, there are 3 constant-speed wind turbines in the SORP feeder.

SORP, STKV, STNO, STSY, JUEL, FLOE, MAST, STCE feeders were used to test the proposed method. The whole studied distribution system was modeled in the standard models of DIgSILENT v.14.1.3 software. The wind turbines were modeled as a Two-Mass system in this study, which is suitable for studying the transient mode of the power system [24]. The power factors of all turbines were 1.

In the eight objective functions which are introduced above, the coefficient of the constant power loads is 0 and the coefficient of the loads which are severely dependent on the frequency and voltage is 1. So, a value of 0.5 is considered for these coefficients in order to balance the frequency change rate.

In the selection table, at which the loads interrupting priority are defined, the change rate of each parameter (i.e., frequency change rate, voltage dependent frequency change rate, power shortage) is available. This table is to see how many loads should be omitted in order to compensate for the active power shortage of the microgrid. In this regard, 3 considered scenarios are as follows:

First scenario (Table 1): it is assumed that loads with less power pay less to the distribution companies. Accordingly, arranging the loads based on cost is equal to arranging the loads in order of the minimum to maximum electrical power respectively.

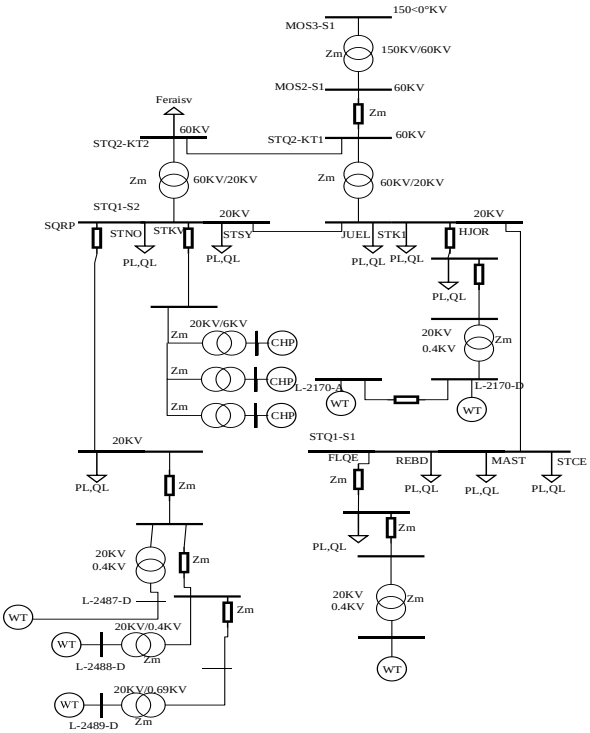

Figure 2. A local microgrid in Denmark.

Second scenario (Table 2): it is assumed that the loads cost has no relation with their power. So, arranging loads based on cost is a random function in terms of their power.

Third scenario (Table 3): like the second scenario, loads are arranged randomly, except that the maximum electrical power is in the first place.

Since the frequency changes can occur over a relatively long period of time due to various transient occurrences, the time period of the frequency changes is important. Therefore, the rate of frequency changes over time is used to detect the islanded state. Equation (9) indicates how to calculate the frequency change rate.

$$R_O C_O F = \frac{df}{dt} = \frac{f_2 - f_1}{t_2 - t_1} \tag{9}$$

In Equation (9), dt is contracted to be *10 ms* for each load in the selection table. Moreover, df is the frequency difference in the islanded microgrid, which is equal to half cycle (the microgrid frequency is *50 Hz*).

In the tables, the frequency change rate, the rate of frequency change dependent to the voltage and the microgrid power shortage are used. But in cutting off a number of loads in the first step, no significant difference was observed between this method and the method [22]. Mathematic formulations of these two functions (the rate of frequency change depends on the voltage and the microgrid power shortage) are available in [14], which are displayed in Equation (10).

$$P_{def} = \frac{2H_{COI}}{f_N}.100.\frac{df_{COI}}{dt} + \sum_{i=1}^{m} P_{L0,i}.\left[\left(\frac{U_i}{U_{0,i}}\right) - 1\right].\frac{100}{P_{L0}} \tag{10}$$

The islanded microgrid was created in zero second. The time of 80 ms is considered for operation of the breaker and command of the relays.

Table 1. The selection table which is sorted by minimum to maximum of loads power.

First scenario

Load level	Load name	Willingness to pay of each load	Rate of change of frequency	Sum of the rate of change of frequency	Rate of change of frequency according to the voltage	Sum of the rate of change of frequency according to the voltage	Deficiency of power (dp)	Sum of the deficiency of power (dp)
1	Load 09	0.81	-21.7	-21.7	-1.7027	-1.7027	-83.5099	-83.5099
2	Load 10	0.83	-21.7	-43.4	-1.7027	-3.4054	-83.5099	-167.0199
3	Load 11	0.86	-21.7	-65.1	-1.7027	-5.1081	-83.5099	-250.5299
4	Load 07	0.87	-25.1	-90.2	-1.7908	-6.8989	-88.5935	-339.1235
5	Load 08	0.89	-28.5	-118.7	-1.8736	-8.7726	-93.4586	-432.5821
6	JUEL	0.91	-29.6	-148.3	-1.9010	-10.6737	-94.7444	-527.3266
7	STCE	0.92	-32.5	-180.8	-1.9824	-12.6561	-99.4948	-626.8214
8	FLOE	0.93	-40.9	-221.7	-2.2084	-14.8646	-111.9883	-738.8098
9	STSY	0.95	-41.1	-262.8	-2.2151	-17.0797	-112.2833	-851.0931
10	STNO	0.96	-38.7	-301.5	-2.1469	-19.2266	-108.6315	-959.7246
11	MAST	1	-48.9	-350.4	-2.4404	-21.6671	-125.1918	-1084.9164

Table 2. The selection table which is sorted by stochastic function of loads power.

Second scenario

Load level	Load name	Willingness to pay of each load	Rate of change of frequency	Sum of the rate of change of frequency	Rate of change of frequency according to the voltage	Sum of the rate of change of frequency according to the voltage	Deficiency of power (dp)	Sum of the deficiency of power (dp)
1	STSY	0.79	-41.1	-41.1	-2.2151	-2.2151	-112.2833	-112.2833
2	Load 10	0.84	-21.7	-62.8	-1.7027	-3.9178	-83.5099	-195.7933
3	STNO	0.85	-38.7	-101.5	-2.1469	-6.0647	-108.6315	-304.4248
4	Load 09	0.86	-21.7	-123.2	-1.7027	-7.7674	-83.5099	-387.9348
5	STCE	0.89	-32.5	-155.7	-1.9824	-9.7498	-99.4948	-487.4296
6	Load 07	0.9	-25.1	-180.8	-1.7908	-11.5407	-88.5935	-576.0232
7	Load 08	0.91	-28.5	-209.3	-1.8736	-13.4144	-93.4586	-669.4818
8	FLOE	0.95	-40.9	-250.2	-2.2084	-15.6229	-111.9883	-781.4702
9	Load 11	0.98	-21.7	-271.9	-1.7027	-17.3256	-83.5099	-864.9802
10	JUEL	0.99	-29.6	-301.5	-1.9010	-19.2266	-94.7444	-959.7246
11	MAST	1	-48.9	-350.4	-2.4404	-21.6671	-125.1918	-1084.9164

Table 3. The selection table which is sorted by stochastic function of loads power and the maximum load is in the first level.

Third scenario

Load level	Load name	Willingness to pay of each load	Rate of change of frequency	Sum of the rate of change of frequency	Rate of change of frequency according to the voltage	Sum of the rate of change of frequency according to the voltage	Deficiency of power (dp)	Sum of the deficiency of power (dp)
1	MAST	0.89	-48.9	-48.9	-2.4404	-2.4404	-125.1918	-125.1918
2	Load 07	0.9	-25.1	-74	-1.7908	-4.2313	-88.5935	-213.7853
3	Load 09	0.91	-21.7	-95.7	-1.7027	-5.9340	-83.5099	-297.2953
4	Load 10	0.92	-21.7	-117.4	-1.7027	-7.6367	-83.5099	-380.8053
5	STCE	0.93	-32.5	-149.9	-1.9824	-9.6191	-99.4948	-480.3001
6	STNO	0.94	-38.7	-188.6	-2.1469	-11.7660	-108.6315	-588.9316
7	Load 11	0.95	-21.7	-210.3	-1.7027	-13.4687	-83.5099	-672.4416
8	JUEL	0.96	-29.6	-239.9	-1.9010	-15.3698	-94.7444	-767.1860
9	FLOE	0.97	-40.9	-280.8	-2.2084	-17.5783	-111.9883	-879.1744
10	Load 08	0.99	-28.5	-309.3	-1.8736	-19.4520	-93.4586	-972.6331
11	STSY	1	-41.1	-350.4	-2.2151	-21.6671	-112.2833	-1084.9164

3. Simulation results

The sample grid introduced for simulation using the proposed method is analyzed in two states:

- The overshoot state, in which the maximum frequency value of the islanded microgrid became more than 1 P.U during frequency stability. Optimal situation for this state occurs when this factor has the minimum value, because the islanded microgrid will be stabilized more quickly.
- Second simulation is performed based on the maximum value of frequency drop in the islanded migrogrid. It is obvious that the less value is the better when the simulation is performed.

To identify the capabilities of the present paper in creating stability in the islanded microgrids, comparisons with [22] have been made; because both articles have the same purpose. These comparisons have been done in 6 states that cover all the states involved in the islanded mode. These 6 states are:

- Minimum microgrid frequency
- Maximum time, at which the overshoot occurs along with the maximum time, at which this frequency occurs.
- Maximum time, at which the frequency of the islanded microgrid decreases.
- Maximum frequency drop in the sample islanded microgrid along with the maximum time, at which this frequency occurs.
- Maximum overshoot frequency along with the maximum time, at which the maximum frequency drop occurs.
- Maximum microgrid frequency, maximum overshoot time, maximum frequency drop and its maximum time.

In the following, each of the proposed tables has been analyzed with the defined objective functions.

3.1. The selection table which is sorted by the first scenario

The goal of the comparison made in this state is to evaluate the capability of the proposed method at the time of the maximum overshoot in the islanded microgrid. Table 4 shows the loads cut-off time according to their priority with the first, fifth and eighth objective functions. In fact, this table indicates the time after which of the loads should be disconnected from the grid when the islanded mode occurs. Accordingly, load 9, which has the shortest operating time, is the least important one among the grid loads and should be unplugged faster than the other grid-connected loads. On the other hand, the result of Table 4 points out that the MAST load has the longest operating time, so this load is the most important load. The objective function of this state presented in Section 2 is ptimized by the genetic optimization algorithm, the results of which are presented in Table 5. Additionally, Figure 3(a-c) shows the diagram of the grid frequency variations in the islanded microgrid and the load shedding for the first, fifth and eighth objective functions respectively.

Table 4. Interruption times of loads for the first, fifth and eighth objective functions in the first scenario.

Load breaker	First objective function	Fifth objective function	Eighth objective function
Load 09	0.0809	0.1025	0.0869
Load 10	0.095859	0.604287	0.133594
Load 11	0.096759	0.924487	0.143394
Load 07	0.100484	1.303721	0.16479
Load 08	0.116384	2.343321	0.16559
Load JUEL	0.137028	2.758584	0.200397
Load STCE	3.288928	3.193084	0.226897
Load FLOE	3.794485	3.537994	0.454497
Load STSY	4.384085	3.974594	0.535197
Load STNO	6.350155	4.484685	1.189543
Load MAST	7.233555	4.663485	2.034243

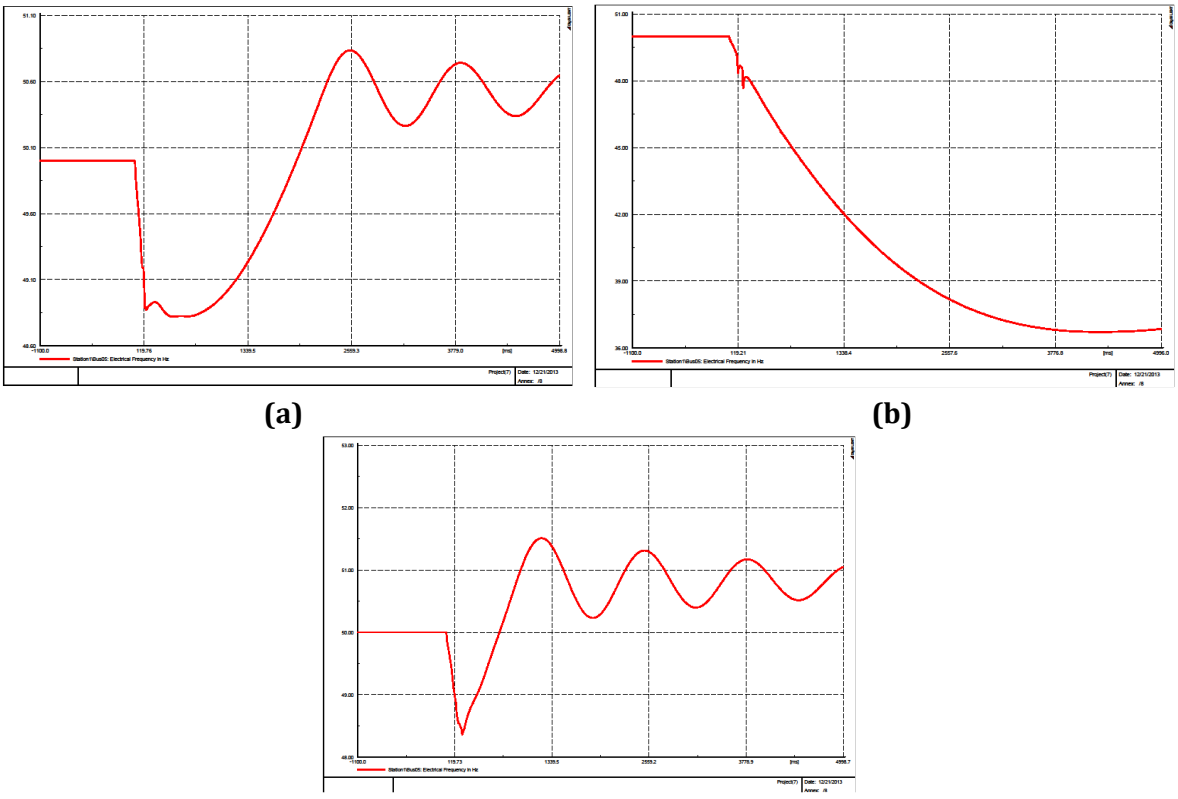

(a) **(b)**

(c)

Figure 3. The load shedding implementation in the first scenario
a. With the first objective function, b. With the fifth objective function, c. With the eighth objective function.

Table 5 exhibits the optimal state obtained from the proposed method using the first, fifth and eighth objective functions. As shown by the first objective function column, the optimal state and stability of the microgrid are achieved by leaving out 6 loads. The convexity and concavity times in this state are specified in the table. It is obvious from the

minimum and maximum times of frequency presented in this table, the stability state of the microgrid has been achieved by the presented method.

According to the values indicated in Table 5, the mentioned objective function has three main advantages compared to the method [22]:

- The frequency drop in the proposed method is much less than the method presented in Ref. [22]. This advantage results in fewer loads outages in the method presented in this paper.
- The maximum frequency of the islanded microgrid in the proposed method is closer to the standard frequency compared to [22], which shows the frequency stability.
- The time to achieve stability in this method is much shorter than the method presented in [22].

Leaving out only 2 loads seemed to be suitable at first. However, the results obtained from fifth objective function indicated that this function could not meet our goals. According to the fact that the microgrid maximum output load was less than the previous step, but this amount of output load was not able to restore the grid stability state and continuation of this process would certainly lead to leaving out all available loads in the islanded microgrid. Therefore, just leaving out the fewer loads cannot be a reason for the excellence of this objective function compared to the previous objective functions.

The eighth objective function is intended to decrease the microgrid maximum frequency, the maximum overshoot time and the maximum frequency drop. So, it is clear that the maximum and minimum frequencies in the proposed method have been significantly improved in this section, which can improve the stability of the microgrid and bring significant technical and economic advantages. According to the comparisons made in the expressed objective functions and considering all the goals of this paper, which are the minimum frequency drop at an optimal time and also reducing the microgrid overshoot at the best time in order to have the minimum output load and the faster stability of the microgrid, the eighth objective function can be an appropriate option in this case.

3.2. The selection table which is sorted by the second scenario

The genetic algorithm of loads cut-off time of the second, sixth and eighth objective functions loads are presented in Table 6 based on the random function of the loads power.

The objective function of this scenario is optimized by the genetic optimization algorithm, the results of which are presented in Table 7. The simulation results of the microgrid after load shedding in the second objective function are given in the second column of Table 7, the purpose of which is to reduce the maximum frequency drop of the islanded microgrid. The results obtained from this objective function show that this function cannot meet our goals in load shedding. According to the fact that the maximum output load of the microgrid is less than the previous steps, but this amount of load leaving could not restore the grid to the stable state and the continuation of this process absolutely will interrupt the all-available loads in the island.

Table 5. Results of the genetic optimization algorithm to investigate the ability of the proposed method at the time that the maximum overshoot occurred in the islanded microgrid for the first, fifth and eighth objective functions in the first scenario.

	Load shedding with first scenario	Load shedding with fifth scenario	Load shedding with eighth scenario
The difference between the maximum frequency and the base frequency	0.8353	1.09	0.51
The maximum frequency	50.8353	51.09	50.51
The concavity time	2530	4.96	1200
The difference between the minimum frequency and the base frequency	1.18	12.25	1.64
The minimum frequency	48.8196	37.75	48.35
The convection time	458	616	212
The number of loads which have experienced power outages	6	2	7

Table 6. Interruption times of loads for the second, sixth and eighth objective functions in the second scenario.

Load breaker	Second objective function	Sixth objective function	Eighth objective function
Load STSY	0.0997	0.098	0.0935
Load 10	0.7315	0.101209	0.102941
Load STNO	0.8259	0.132609	0.119241
Load 09	1.94401	0.973655	0.559156
Load STCE	3.96241	1.137755	0.736256
Load 07	4.753467	2.850715	0.83812
Load 08	4.767467	3.343215	1.52432
Load FLOE	5.900207	4.186286	1.689759
Load 11	6.090407	5.348086	2.272759
Load JUEL	7.420477	6.002209	2.52469
Load MAST	9.340277	6.588609	3.43919

So, ejection of only two loads in the first step cannot be a guarantee for the success of this method. The proposed formulation in the sixth objective function is presented with the goal of reducing the maximum frequency drop in the sample islanded microgrid along with the time, at which this frequency occurred. The frequency of the proposed method is closer to the main frequency in comparison with [22]. Also, in the proposed method, the time to reach 50 Hz after the frequency drop is shorter than [22]. Therefore, this objective function is suitable for load shedding and can reduce the times obtained from the study [22] to an acceptable level. The eighth objective function is considered with the aim of reducing the maximum frequency of the microgrid, the maximum overshoot time, the maximum frequency drop and the maximum time. The number of the proposed outputs of this objective function is three.

Table 7. Results of the genetic optimization algorithm to investigate the ability of the proposed for the second, sixth and eighth objective functions in the second scenario**.**

	Load shedding with second scenario	Load shedding with sixth scenario	Load shedding with eighth scenario
The difference between the maximum frequency and the base frequency	-	1.47	1.55
The maximum frequency	-	51.47	51.471
The concavity time	-	954	941
The difference between the minimum frequency and the base frequency	5.47	1.11	1.14
The minimum frequency	44.52	48.89	48.86
The convection time	743	144	105
The number of loads which have experienced power outages	2	3	4

The time of the microgrid maximum frequency drop and the time of the grid maximum frequency in the proposed method are improved in comparison with [22]. Moreover, in the proposed method, the time to reach *50 Hz* after the frequency drop is at *402 ms* and in the method [22], it is *860 ms*. Minimum frequency drop and reducing the microgrid overshoot, both at an optimal time, are the objectives of this paper in order to have the minimum output load and faster stability of the microgrid. According to the comparisons, first and eighth objective functions can be suitable to achieve these purposes.

3.3. The selection table which is sorted by the third scenario

The genetic algorithm of the loads cut-off time for the third, seventh and eighth objective functions is proposed in Table 8 according to their priorities based on the random function of the loads power with the difference that the maximum electric power is in the first place. The figures of the final frequency for the third, seventh and eighth objective functions are given in the Figure 4(a-c). The simulation results after load shedding are given in Table 9 using the third objective function. The number of recommended outputs of the third objective function is 1. The loads cut-off time according to its priorities is presented in Table 8 in the seventh objective function so as to reach the goals of reducing the maximum overshoot time and the maximum frequency drop time. The figure of the final frequency and the simulation results after load shedding are given in the third column of Table 9.

The maximum frequency drop of the microgrid in the eighth objective function is *0.708* in *103 ms*; which is *0.90* in the method [22]. The maximum frequency of the grid is *51.1154 Hz* in *1083 ms*; which is *50.926 Hz* in the method [22]. The time to reach *50 Hz* after the frequency drop in the proposed method is *463 ms* and in the method [22] is *970 ms*.

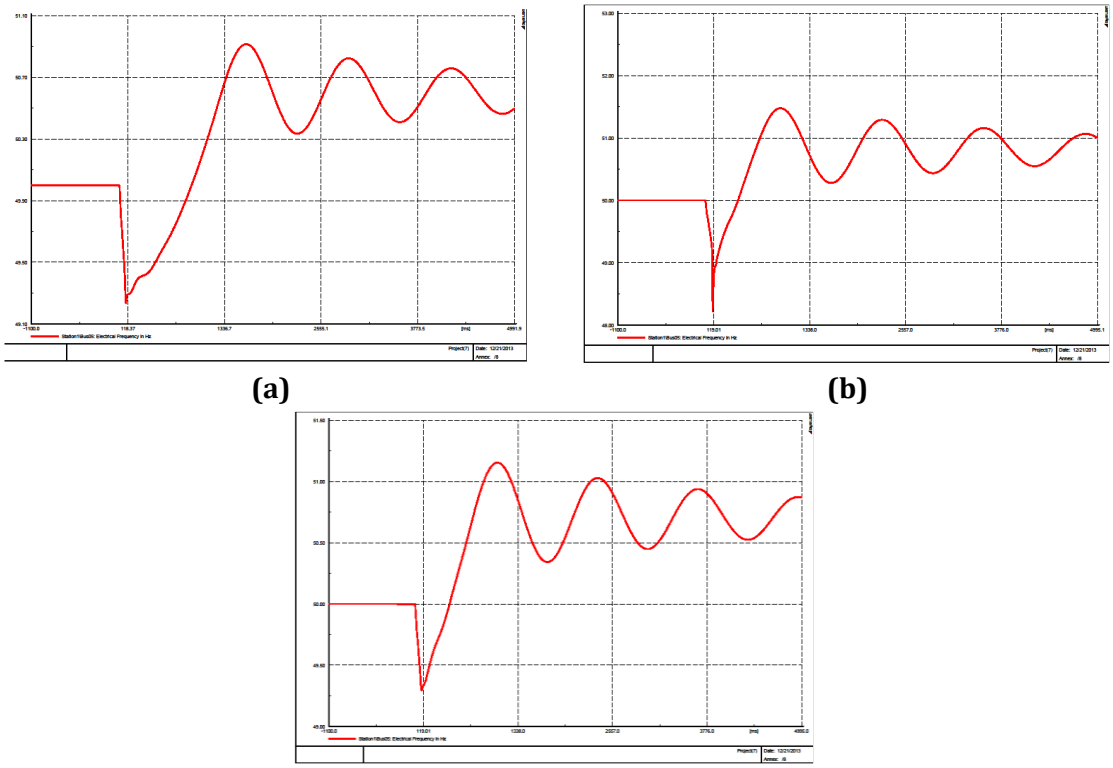

Figure 4. The load shedding implementation in the third scenario
a. With the third objective function, b. With the seventh objective function, c. With the eighth objective function.

Table 8. Interruption times of loads for the third, seventh and eighth objective functions in the third scenario.

Load breaker	Third objective function	Seventh objective function	Eighth objective function
Load MAST	0.0801	0.0923	0.0814
Load 07	0.88581	0.100993	0.083267
Load 09	1.00441	0.133293	1.307267
Load 10	1.408599	1.212483	2.043744
Load STCE	1.786699	1.803783	3.144644
Load STNO	1.970225	1.852836	3.295747
Load 11	2.409325	1.855336	3.314747
Load JUEL	2.82646	2.899916	3.334513
Load FLOE	3.10646	3.335916	3.588913
Load 08	3.509112	4.2736	3.716606
Load STSY	4.199612	4.6577	3.959106

According to the comparisons made in the expressed objective functions and the purposes of this paper, the eighth objective function can be a suitable option for this case. A comparison of these three scenarios with the selected objective function of each is observed in Figure 5. By comparing the selected functions for each of these three scenarios, the third objective function has the best response for the proposed objective function. For this scenario, maximum 2 cut-off loads for load shedding, the maximum

frequency drop of *0.71 Hz* at the best time of *103 ms* and the maximum frequency rise of *0.59 Hz* at the time of *1083 ms* are recorded. After that, the second scenario gives the proposed suitable response with maximum 3 loads for load shedding, the maximum frequency drop of *1.034 Hz* in *102 ms* and the maximum frequency rise of *1.55 Hz in 901 ms*. Finally, the first scenario gives the proposed objective function with maximum 7 loads for load shedding, the maximum frequency drop of *1.64 Hz* in the best time of *212 ms* and the maximum frequency rise of *1.51* in *1200 ms*. The obtained results show the superiority of the method presented in this paper over similar study made in [22], because as shown, the time to achieve stability in this paper is much better than the mentioned study in the all states. In addition to improve the stability of the grid and creating many technical benefits in the grid, this issue helps significantly in reducing the costs of the distribution companies. Because the numbers and duration of outages are decreased by the method proposed in this paper.

Table 9. Results of the genetic optimization algorithm to investigate the ability of the proposed for the third, seventh and eighth objective functions in the third scenario.

	Load shedding with third scenario	Load shedding with seventh scenario	Load shedding with eighth scenario
The difference between the maximum frequency and the base frequency	0.914	1.157	1.154
The maximum frequency	50.914	51.157	51.154
The concavity time	1611	1093	1083
The difference between the minimum frequency and the base frequency	0.764	0.919	0.708
The minimum frequency	49.236	49.08	49.29
The convection time	91	113	103
The number of loads which have experienced power outages	1	2	3

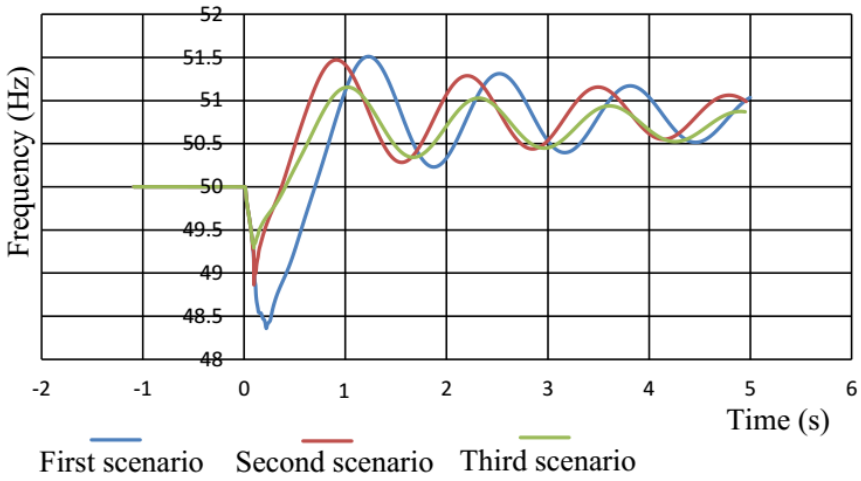

Figure 5. The comparison of the first, second and third scenarios.

4. Conclusions

Despite its advantages, operation of DGs in the islanded state may cause some concerns, the most important of which is the frequency stability.

Regarding the concerns, in this paper, solutions for load shedding of the small grids with the aim of stabilizing the frequency of these grids are analyzed and presented. In the method used in this paper, the technical and economic purposes related to load shedding strategy are considered simultaneously. The proposed method does not require the telecommunication infrastructures in order to communicate between the component and the real microgrid data.

The automatic load cut-off is done according to the frequency drop, frequency drop time, overshoot and its time. Other advantages of the proposed method in this paper compared to the previous studies are low drop of the frequency and achieving the stability in a shorter time. So, the importance of the results obtained from the implementation of this project can be summarized in the following cases:

- Successful exploitation of DGs in the islanded mode along with ensuring the frequency stability of the grid
- Increase in public satisfaction rate of consumers by creating frequency stability and a subsequent reduction in the outages of their sensitive loads

References

[1] R. Aljarrah, B. B. Fawaz, et al., "Issues and Challenges of Grid-Following Converters Interfacing Renewable Energy Sources in Low Inertia Systems: A Review," *IEEE Access*, vol. 12, pp. 5534-5561, 2024.

[2] A. H. Sajid, A. Altamimi, S. A. A. Kazmi, and Z. A. Khan, "Multi-Micro Grid System Reinforcement Across Deregulated Markets, Energy Resources Scheduling and Demand Side Management Using a Multi-Agent-Based Optimization in Smart Grid Paradigm," *IEEE Access*, vol. 12, pp. 21543-21558, 2024.

[3] R. Eslami, S. H. H. Sadeghi, H. Askarian-Abyaneh, and A. Nasiri, "A Novel Method for Fault Detection in Future Renewable Electric Energy Delivery and Management Microgrids, Considering Uncertainties in Network Topology," *Electric Power Components and Systems*, vol. 45, no. 10, pp. 1118-1129, 2017.

[4] R. Eslami, and S. A. Hosseini, "A Comprehensive Method for Fault Detection in AC/DC Hybrid Microgrid," *Electric Power Components and Systems*, vol. 50, no. 1-2, pp. 38-51, 2022.

[5] Ê. C. Resende, M. G. Simões, and L. C. G. Freitas, "Anti-Islanding Techniques for Integration of Inverter-Based Distributed Energy Resources to the Electric Power System," *IEEE Access*, vol. 12, pp. 17195-17230, 2024.

[6] M. Sun, G. Liu, M. Popov, V. Terzija, and S. Azizi, "Underfrequency Load Shedding Using Locally Estimated RoCoF of the Center of Inertia," *IEEE Transactions on Power Systems*, vol. 36, no. 5, pp. 4212-4222, 2021.

[7] S. Azizi, M. Sun, G. Liu, and V. Terzija, "Local Frequency-Based Estimation of the Rate of Change of Frequency of the Center of Inertia," *IEEE Transactions on Power Systems*, vol. 35, no. 6, pp. 4948-4951, 2020.

[8] R. Eslami, and S. A. Hosseini, "Presenting New Triple Methods for Fault Detection, Location, and Its Identification in DC Microgrid," *Iranian Journal of Science and Technology, Transactions of Electrical Engineering*, vol. 44, pp. 849-860, 2020.

[9] J. Yan, F. Guo, and C. Wen, "Attack Detection and Isolation for Distributed Load Shedding Algorithm in Microgrid Systems," *IEEE Journal of Emerging and Selected Topics in Industrial Electronics*, vol. 1, no. 1, pp. 102-110, 2020.
[10] J. Wang, F. Jie, et al., "Strategy on Interruptible Load Selection for Precise Load Shedding System of Source-Grid-Load Friendly Interaction System," *IEEE 3rd Conference on Energy Internet and Energy System Integration (EI2)*, pp. 1765-1769, 2019.
[11] S. Hirodontis, H. Li, and P. A. Crossley, "Load Shedding in A Distribution Network," *International Conference on Sustainable Power Generation and supply*, pp.1-6, 2009.
[12] U. Rudez, and R. Mihalic, "Monitoring the First Frequency Derivative to Improve Adaptive Underfrequency Load-Shedding Schemes," *IEEE Transactions on Power Systems*, vol. 26, no.2, pp. 839-846, 2011.
[13] U. Rudez, and R. Mihalic, "Analysis of Underfrequency Load Shedding Using a Frequency Gradient," *IEEE Transactions on Power Delivery*, vol. 26, no.2, pp. 565-575, 2011.
[14] N. M. Sapari, H. B. Mokhlis, et al., "Load Shedding Scheme Based on Frequency and Voltage Stability for an Islanding Operation of a Distribution Network Connected to Mini-Hydro Generation," *Turkish Journal of Electrical Engineering and Computer Sciences*, vol. 25, no.3, pp. 1852-1863, 2017.
[15] U. Rudez, and R. Mihalic, "A Novel Approach to Underfrequency Load Shedding," *Electric Power Systems Research*, vol. 78, no. 3, pp. 517-525, 2008.
[16] A. A. Girgis, and S. Mathure, "Application of Active Power Sensitivity to Frequency and Voltage Variations on Load Shedding," *Electric Power Systems Research*, vol. 80, no. 3, pp. 306-310, 2010.
[17] J. J. Ford, H. Bevrani, and G. Ledwich, "Adaptive Load Shedding and Regional Protection," *International Journal of Electrical Power & Energy Systems*, vol. 31, no. 10, pp. 611-618, 2009.
[18] S. Hirodontis, and H. Li, "An Adaptive Load Shedding Method for Intentional Islanding," *International Conference on Clean Electrical Power*, pp. 300-303, 2009.
[19] A. Arulampalam, and T. K. Saha, "Fast and Adaptive Under Frequency Load Shedding and Restoration Technique Using Rate of Change of Frequency to Prevent Blackouts," *IEEE PES General Meeting*, pp. 1-8, 2010.
[20] L. Zhang, and J. Zhong, "UFLS Design by Using f and Integrating df/dt," *IEEE PES Power Systems Conference and Exposition*, pp. 1840-1844, 2006.
[21] S. V. Kolluri, J. R. Ramamurthy, et al., "Relay-Based Undervoltage Load Shedding Scheme for Entergy's Western Region," *IEEE Power & Energy Society General Meeting*, pp. 1-5, 2015.
[22] P. Mahat, Z. Chen, and B. Bak-Jensen, "Underfrequency Load Shedding for an Islanded Distribution System with Distributed Generators," *IEEE Transactions on Power Delivery*, vol. 25, no. 2, pp. 911-918, 2010.
[23] F. T. Dai, "Impacts of Distributed Generation on Protection and Autoreclosing of Distribution Networks," *10th IET International Conference on Developments in Power System Protection (DPSP 2010)*, pp. 1-5, 2010.
[24] V. P. Singh, N. Kishor, P. Samuel, and N. Singh, "Small-Signal Stability Analysis for Two-Mass and Three-Mass Shaft Model of Wind Turbine Integrated to Thermal Power System," *Computers & Electrical Engineering*, vol. 78, pp. 271-287, 2019.

Declaration of Competing Interest

The authors declare that they have no known competing financial interests or personal relationships that could have appeared to influence the work reported in this paper. The ethical issues, including plagiarism, informed consent, misconduct, data fabrication and/or falsification, double publication and/or submission, redundancy, have been completely observed by the authors.

Credit Authorship Contribution Statement

Reza Eslami: Conceptualization, Data curation, Formal analysis, Funding acquisition, Project administration, Software, Supervision, Validation, Roles/Writing - original draft, Investigation, Methodology, Resources, Visualization, Writing - review & editing.

Bibliography

Reza Eslami received the B.Sc., M.Sc. and Ph.D. degrees in Electrical and Electronics Engineering from the Department of Electrical Engineering, Amirkabir University of Technology, Tehran, Iran, in 2010, 2012 and 2017 respectively. He has also worked as an Associate Professor with the Department of Electrical Engineering, Sahand University of Technology, Tabriz, Iran, since 2017. His research interests are smart grids and power system protection.

Journal of Green Energy Research and Innovation

Applying Sliding Mode Control Along with Particle Swarm Algorithm in Order to Optimally Control the System Wind Turbines with Variable Speed

Sasan Pirouzi, Ali Naderi

Highlights

- MPP tracking while observing the allowed range of duty cycle
- Preserving the permissible range of ripples of various parameters
- Extending the operating range of the variable-resistance method
- Adopting the proposed method for PV energy management

Graphical Abstract

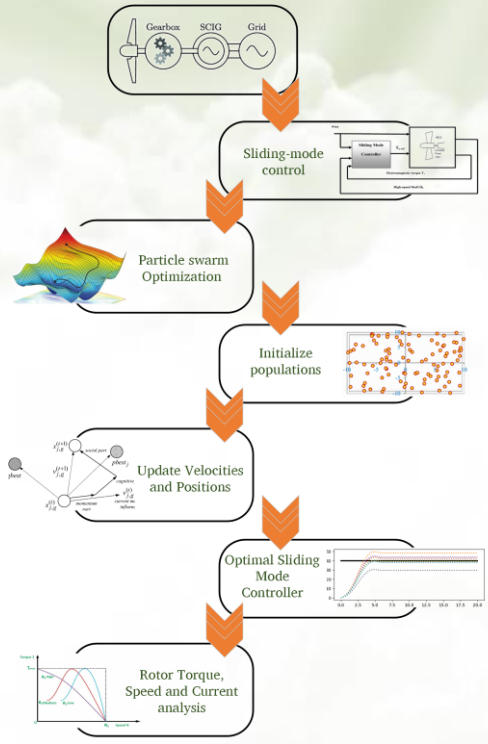

Use your device to scan and read the article online

Citation

S. Pirouzi, and A. Naderi, "Applying Sliding Mode Control Along with Particle Swarm Algorithm in Order to Optimally Control the System Wind Turbines with Variable Speed," *Journal of Green Energy Research and Innovation*, vol. 1, no. 2, pp. 64-80, 2024.

https://doi.org/10.61186/jgeri.1.2.64

JGERI Journal of Green Energy Research and Innovation

Online ISSN: 3041-9018

Journal of Green Energy Research and Innovation

Journal Homepage: www.jgeri.araku.ac.ir

Applying Sliding Mode Control Along with Particle Swarm Algorithm in Order to Optimally Control the System Wind Turbines with Variable Speed

Sasan Pirouzi [1]*, Ali Naderi [2]

[1] *Islamic Azad University of Semmirom Branch, Semmirom, Iran.*
[2] *Department of Engineering, Yazd University, Yazd, Iran.*

* ***Corresponding Author:*** *s.pirouzi@sutech.ac.ir*

ARTICLE INFO

Keywords:
Wind turbine,
Sliding mode control,
Particle swarm algorithm.

Article history:
Received: 04 February 2024;
Revised: 01 March 2024;
Accepted: 06 March 2024;

Article type:
Research Article

ABSTRACT

The utilization of renewables is developing rapidly due to environmental issues and a lack of fuel fossils. In this regard, wind turbines, as a type of renewable energy source, have been widely adopted in the power system thanks to their higher power generation capacity. Numerous methods have been introduced so far to control wind turbines, which are essential in generating wind energy. The sliding mode control, because of its unique features like being resistant to external disturbances, dynamics unmodeled and uncertainty, the relative simplicity of the control law, a relatively small amount of calculations, and straightforward implementation, is amongst the most preferred control designs in this realm. In this study, the control strategy is based on a combination of sliding mode and particle swarm optimization and is applied to a wind turbine with a grid-connected squirrel cage induction generator. The proposed method maximizes the power output of the wind turbine by limiting small changes in the electromagnetic torque. The main goal of the suggested design is to reduce the squared error of the electromagnetic torque, rotor speed, and stator current. The sliding mode control for the wind turbine helps obtain optimal values for the parameters of the design.

1. Introduction

1.1. Modified quadratic power curve

The use of renewable energy sources is expanding rapidly due to environmental concerns and the depletion of fossil fuels [1-3]. Among these sources, wind turbines have attracted considerable attention over other renewable technologies because of their significant power generation potential [4-5]. Wind turbines can be categorized based on their operational speed into two types: fixed and variable speed [6-7]. Variable-speed wind turbines offer numerous advantages over their fixed-speed counterparts, including the ability to align the generator shaft speed with varying wind speeds. Several control methods have been proposed by researchers to optimize turbine performance. For instance, some have developed a feedback controller for the system using linear control methods. These approaches rely on linearizing the wind turbine model, simplifying the

turbine equations, and designing the controller, which can simplify the analytical solution. However, linear controllers are limited by the wind turbine's nonlinear characteristics and cannot achieve the desired optimal performance due to these limitations and nonlinear behaviors. Sliding mode control, known for its robustness to external disturbances, unmodeled dynamics, and uncertainties, along with the simplicity of its control law and minimal computational requirements, emerges as an ideal solution for controlling nonlinear, multivariable systems like wind turbines. Thus, sliding mode control is considered by many researchers as the preferred method for achieving optimal turbine control.

1.2. Research background

Ref. [8] discusses the high-order sliding mode control method due to features such as reducing external mechanical stress, limited arrival time, and resistance to external and dynamic disturbances, including unmodeled ones. This article utilizes a 2nd order vector slip surface to generate control signals. It employs rotor current and electric torque to maximize output power without damaging the system. Article [9] explores control of production power in turbines, acknowledging that wind speeds vary. It introduces a system with two working areas dependent on peak speed, utilizing a high-degree sliding mode control method to ensure system stability in both areas and to apply ideal feedback control. Despite model uncertainties, this control method demonstrates resistance to system parameter uncertainties. It calculates the speed of the rotor and its torque via a sliding mode observer, and the difference from the optimal torque is used as the control error. A sliding mode modulator is employed to control the output power. Another approach for controlling the generator [10], is the adaptive fuzzy integral variable structure controller, aimed at maximizing wind power by adjusting turbine speed based on wind speed. This surpasses traditional control methods reliant on mathematical models. It introduces an adaptive fuzzy integral variable structure for control. The combination of a robust nonlinear controller with quadratic sliding mode control [11] represents another strategy for turbine control. This method integrates a robust nonlinear controller with a quadratic sliding mode method, known as the strong convolution algorithm, to manage the wind turbine system. The goal is to maximize wind energy captured by the turbine and maintain the stator power factor of a wire rotor induction generator at a desired level. Ref. [12] proposes a method to control generator speed, presenting a variable-speed wind turbine power control method connected to the grid. Another study combines integral variable structure control and directional field vector to manage rotor voltage, subsequently controlling rotor current and stator voltage [13]. To address the buzzing phenomenon, a saturation function replaces the sign function. Additionally, to minimize steady-state error, an integral sliding surface is employed, which overall achieves our objectives for the smoothness and safety of the generator in controlling no-load disconnection.

In another approach, sliding mode control is utilized for bending angle control due to its fast response, minimal lift, and resistance to disturbances. However, the sliding mode method often encounters the issue of creating a buzzing phenomenon. This article

mitigates the problem through the use of a pseudo-sliding mode generator, showcasing that the control agent employed offers higher efficiency compared to traditional integral controllers [14]. Ref. [15] discusses a control strategy employing a nonlinear flow on the turbine for variable-speed wind turbines with dual induction generators. Ref. [16] presents an enhanced direct power control method for grid-connected wind turbines, especially when facing unbalanced grid voltages. Furthermore, Ref. [17] explores the application of second-order sliding mode control for synchronous power control in networking.

1.3. Research gaps and contributions

Control of wind turbines using sliding mode control is sparsely covered in existing research. This method, notable for its distinct capabilities, is the focus of this paper. Sliding mode control is characterized by its variable structure, rapidly switching between multiple control strategies. The initial design step involves selecting a suitable sliding surface, crucial for modeling the system's optimal closed-loop performance in the variable state space. Subsequent steps include determining the paths for system control to ensure it remains within the desired trajectory [18]. The design of a sliding mode controller for wind turbines, especially variable speed ones, prioritizes ensuring effective performance and control stability. As demonstrated in Figure 1, this paper utilizes a smart particle swarm algorithm to optimize the parameters of the sliding surface function for sliding mode control. It's worth mentioning that the approach outlined in this paper potentially maximizes the power harvested from the wind turbine by minimizing fluctuations in electromagnetic torque. Essentially, this paper proposes a control strategy that merges sliding mode control with an optimal algorithm, specifically particle swarm optimization, applied to a grid-connected wind turbine with a squirrel cage induction generator. This strategy aims to achieve two objectives. The primary goal is to maximize the wind power captured by the turbine, while the secondary goal, pursued concurrently, is to minimize changes in electromagnetic torque. The innovation and features of this approach are highlighted as follows:

- Using the sliding mode control for the wind turbine to obtain the maximum power from the wind system.
- Determining the optimal values of the parameters of the sliding surface function of the sliding mode control for the optimal performance of the wind turbine.

Next, the proposed design model for the wind turbine is detailed in the second part. Following that, the third part provides numerical results to assess the effectiveness of the proposed design. Finally, the fourth part discusses the overall implications of the results.

2. Wind turbine model

Figures 1 and 2 present the comprehensive block diagram of the system under study, which is a variable speed squirrel cage induction generator (SCIG) controlled via sliding mode. Additionally, the parameters of the sliding mode controller are optimized using the Particle Swarm Optimization (PSO) algorithm, thereby assessing its optimal

configuration. Consequently, the model of the wind power plant, the sliding mode controller, and the PSO algorithm are detailed in the subsequent sections.

2.1. Wind energy conversion system model

Based on Figure 2, the important components of a variable-speed wind turbine are:

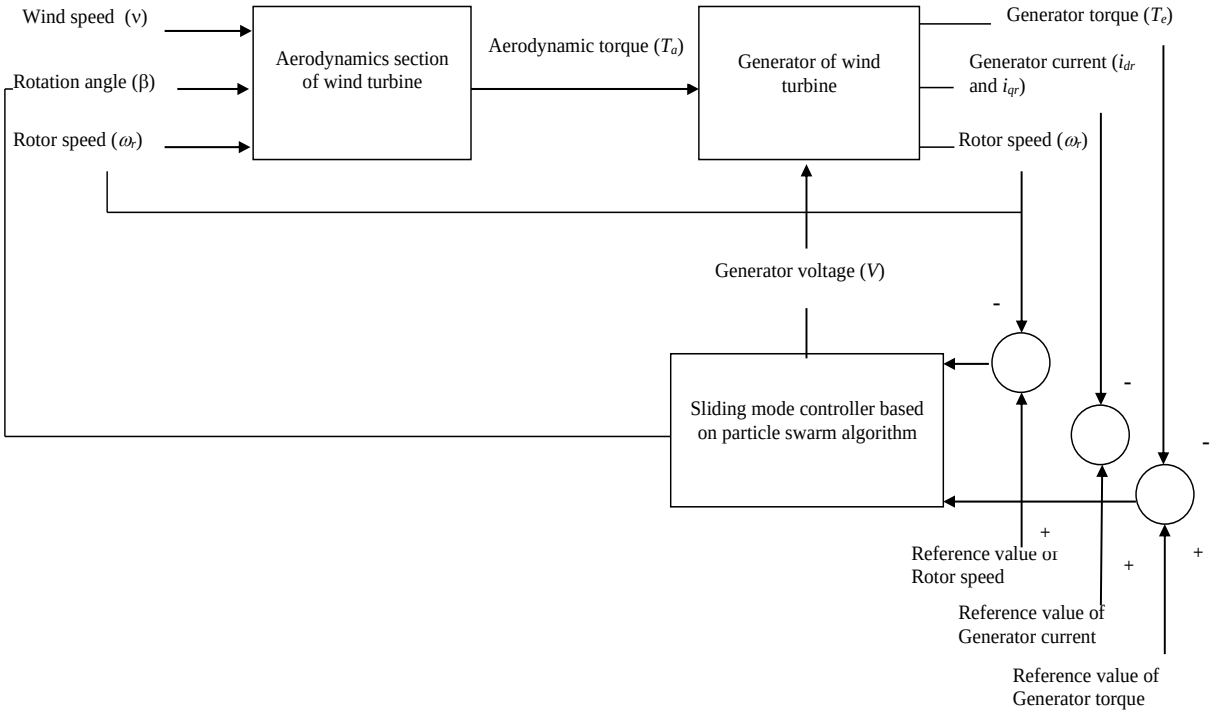

Figure 1. General of the proposed plan.

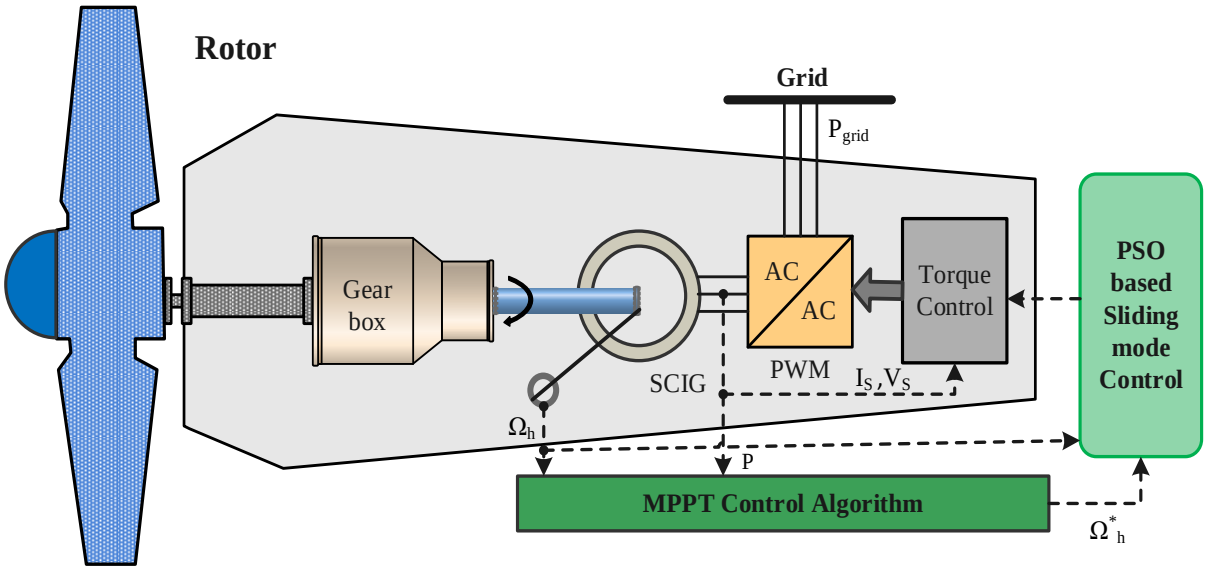

Figure 2. Wind energy conversion system based on SCIG.

1- Turbine
2- gearbox
3- Squirrel rack induction generator (SCIG) connected to the grid

Therefore, in the following, the mathematical model of these components will be presented in order, which expresses their behavior in the studied system.

A) wind turbine model (aerodynamic section) Wind turbine *generally* converts the kinetic energy of the wind into mechanical energy slowly and also the total energy available from the wind turbine can be calculated from Equation (1):

$$E_k = \frac{1}{2}mv^2 \tag{1}$$

where (m) represents the mass of air passing through a square disk of one square meter, and (v) denotes the wind speed, expressed in meters per second. It should be noted that the air mass can also be calculated from Equation (2):

$$m = \rho Ad \tag{2}$$

In Equation (2), (ρ) represents the air density, (A) denotes the area swept by the turbine blades, and (d) is the distance from the wind source. According to Betz's theory, the mechanical power extractable from the wind turbine (P_a) can be calculated using the form of Equation (3):

$$P_a = \frac{1}{2}\rho\pi R^2 v^3 C_p(\lambda,\beta) \tag{3}$$

where (R) is the radius of the wind turbine blade, (λ) represents the tip speed ratio, and (β) denotes the pitch angle, referring to the angle between the chord of the blade and the plane of rotation. Finally, (C_p) is the power coefficient of the wind turbine. It is noteworthy that the tip speed ratio is given by Equation (4):

$$\lambda = \frac{\omega_r R}{v} \tag{4}$$

(ω_r) is the rotational speed of the wind turbine rotor. It should be noted that Ref. [19] has derived a mathematical relationship for (C_p), which is expressed in the form of Equation (5):

$$C_p(\lambda,\beta) = 0.5176\times(116\Gamma - 0.4\beta - 5)\times e^{-21\Gamma} + 0.0068\lambda \qquad \forall\Gamma = \frac{1}{\lambda + 0.08\beta} - \frac{0.035}{\beta^3 + 1} \tag{5}$$

Phrase Γ introduces a covariate for calculating (C_p). Moreover, the power of the rotor (aerodynamic power, also denoted as (P_a)) is given by Equation (6):

$$P_a = \omega_r T_a \tag{6}$$

that (T_a) is equal to the aerodynamic torque, and Equation (7) can be calculated by:

$$T_a = \frac{1}{2}\pi\rho R^3 C_q(\lambda) v^2 \tag{7}$$

where (C_q) is calculated based on Equation (8):

$$C_q(\lambda) = \frac{C_p(\lambda)}{\lambda} \tag{8}$$

B) squirrel cage induction generator model (SCIG): Voltage equations of squirrel cage asynchronous generator in dq frame of reference based on references [19-20] can be expressed as Equation (9):

$$\begin{bmatrix} v_{ds} \\ v_{qs} \\ 0 \\ 0 \end{bmatrix} = \begin{bmatrix} R_s + L_s p & -\omega_1 L_s & L_m p & -\omega_1 L_m \\ \omega_1 L_s & R_s + L_s p & \omega_1 L_m & L_m p \\ L_m p & 0 & R_r + L_r p & 0 \\ \omega_s L_m & 0 & \omega_s L_r & R_r \end{bmatrix} \begin{bmatrix} i_{ds} \\ i_{qs} \\ i_{dr} \\ i_{qr} \end{bmatrix} \quad (9)$$

Also, the equations of connected flux are based on [20-21] and can be calculated by Equation (10):

$$\begin{bmatrix} \phi_{ds} \\ \phi_{qs} \\ \phi_{dr} \\ \phi_{qr} \end{bmatrix} = \begin{bmatrix} L_s & 0 & L_m & 0 \\ 0 & L_s & 0 & L_m \\ L_m & 0 & L_r & 0 \\ 0 & L_m & 0 & L_r \end{bmatrix} \begin{bmatrix} i_{ds} \\ i_{qs} \\ i_{dr} \\ i_{qr} \end{bmatrix} \quad (10)$$

Hence, the SCIG torque equation can be calculated by Equation (11):

$$T_e = n_p \frac{L_m}{L_r} i_{qs} \phi_r \quad (11)$$

Additionally, this is described by Equation (12):

$$\phi_r = \frac{L_m}{T_r p + 1} i_{ds} \quad (12)$$

In the aforementioned equations, (v_{ds}) and (v_{qs}) represent the components of the measured voltage; (i_{ds}), (i_{qs}), (i_{dr}), and (i_{qr}) are the respective stator and rotor current components. The vector components of stator and rotor flux linkages are denoted as (ϕ_{ds}), (ϕ_{qs}), (ϕ_{dr}), and (ϕ_{qr}). Stator and rotor phase resistances are indicated by (R_s) and (R_r)respectively. (L_r) and (L_s) correspond to the stator and rotor inductance, while (L_m) signifies the mutual inductance between the stator and rotor. The symbol (n_p) stands for the number of pole pairs, (p) denotes the time derivative $\left((\frac{d}{dt})\right)$, (ω_s) represents the synchronous angular velocity and the rotor time constant $((T_r))$ is expressed as $(\frac{L_r}{R_r})$.

2.2. Proposed sliding mode control

Sliding Mode Control (SMC) has been applied to various systems recently due to its simplicity in implementation and robustness against uncertainties and external disturbances [22]. SMC involves guiding the system to a desired sliding surface and then applying a control law to ensure the system remains within this surface [23]. The design process of SMC includes 1) selecting the sliding surface, 2) specifying the conditions for convergence, and 3) defining the control law for sliding mode, with each step detailed below:

A) Selecting the switching level: A nonlinear system can be be expressed as Equation (13):

$$\dot{X} = f(X,t) + g(X,t)u(X,t) \qquad X \in R^n, u \in R \quad (13)$$

that *f(X,t)* and *g(X,t)* are assumed to be bounded and non-deterministic linear non-continuous functions. Generally, the form of Eq is utilized by Cellutin to determine the sliding surface [24], as presented in the following form, known as Equation (14):

$$S(X)=\left(\frac{d}{dt}+\gamma\right)^{n-1} e, \quad e=X^{d}-X, \quad X=[X,\dot{X},...,X^{n-1}]^{T}, \; X^{d}=[X^{d},\dot{X}^{d},\ddot{X}^{d},...]^{T} \tag{14}$$

where, e, γ, n, X^{d}, and X are equal to the error vector, positive coefficient, system degree, requested state vector, and state vector, respectively.

b) Definition of convergence conditions: Convergence conditions that determine the allowed and non-allowed area are established through the Lyapunov Equation [25] as depicted in Equation (15):

$$S(x)\dot{S}(X)\leq 0 \tag{15}$$

The control algorithm is defined by Equation (16):

$$u=u^{eq}+u^{n} \tag{16}$$

where u, u_{eq}, u^{n}, $sat(S(X)/\varphi)$ and φ are Control variable, equivalent control variable, switching control, saturation function and threshold width of the saturation function respectively. See Equations (17) and (18):

$$u^{n}=u^{\max} sat(S(X)/\varphi) \tag{17}$$

$$sat(S(X)/\varphi)=\begin{cases}\text{sgn}(S) & if \;\; |S|>\varphi \\ S/\varphi & if \;\; |S|<\varphi\end{cases} \tag{18}$$

Based on Equation (12), the rotor flux (φ_r) is solely a function of the d-axis stator current (i_ds). Thus, if the rotor flux remains constant, the generator torque (T_e) depends only on the q-axis stator current (i_qs). Consequently, controlling T_e can be achieved by regulating i_qs. A proposed SMC scheme for controlling the electromagnetic torque (T_e) of a variable speed SCIG wind turbine is illustrated in Figure 3. In the variable speed wind turbine system, the sliding surface is chosen to allow the turbine to operate near the optimal regime characteristics [26]. Therefore, the sliding surface in this study is selected based on Ref. [27] as follows in Equation (19):

$$S=m_1 J_t \omega_h + m_2 J_t T_e - J_t \omega^{*}_{h} \tag{19}$$

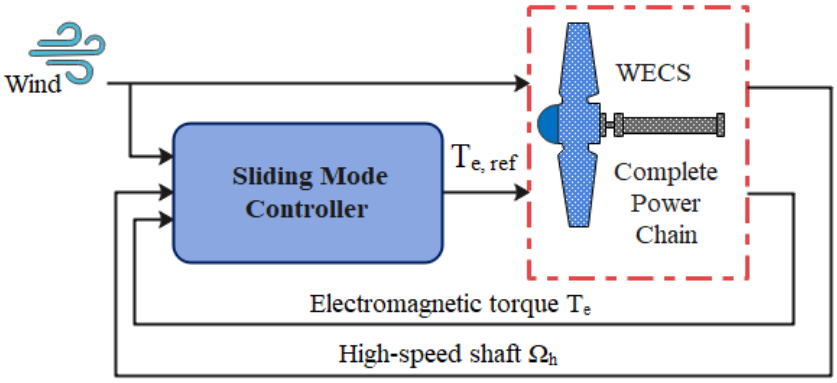

Figure 3. Sliding mode control plan.

The total sliding mode control law for the variable speed wind turbine system is the sum of the equivalent control components and switching control components. This is considered in Equations (20)-(22)

$$T_{e-ref} = u^{eq} + u^{n} \tag{20}$$

$$u^{eq} = T_e - \frac{T_e}{1+m_2 J_t}\left(m_1 J_t \omega_h + m_2 J_t T_e\right)\left(m_1 - A(\lambda, v)\right) \tag{21}$$

$$A(\lambda, v) = \left(K.v.R^2\right)/\, j^2.\left(\dot{C}_p(\lambda).\lambda - C_p(\lambda)\right)/\, \lambda^2 \tag{22}$$

Considering $K = 0.5\pi\rho * R^2$ and $\left(C_P'(\lambda)\right)$ equal to the derivative of the power factor relative to (λ). Also, $(m_1 = -1/T_{sm})$ is equal to the inverse of the time constant, and (m_2) is equal to the static gain. This relationship is presented as Equation (23):

$$m_2 = -m_1 \frac{\omega_{hopt}}{T_{eopt}\left(1+\kappa\left(\omega_h - \omega_{hopt}\right)/\, \omega_{hopt}\right)} \tag{23}$$

The switching component of the control of the sliding law $\left((u_n)\right)$ is determined by selecting the Lyapunov function. The root form of the obtained sliding surface is calculated according to Equation (24):

$$u^{n} = -\alpha\, \mathrm{sgn}_{\varphi}(S) \tag{24}$$

2.3. Particle swarm algorithm (PSO)

To initiate the particle swarm optimization (PSO) algorithm, specific populations are established for each variable. Subsequently, a random value is generated for each variable and population within the predefined range of variable changes. The next phase involves calculating the fitness function for each population, noting that the fitness function aligns with the objective function of the problem at hand. Following this, the algorithm determines the best point, representing the optimum of the fitness function, with the variables at this juncture denoted as (x_{best}). To navigate towards this optimal point, the particle transitions to a new position at a certain velocity. Thus, this stage necessitates the computation of the particle's new velocity and position, achievable through Equations (25) and (26), respectively [28].

$$v_j^{(k+1)} = w v_j^{(k)} + c_1 \times rand_1 \times \left(x_{best}^{(k)} - x_j^{(k)}\right) + c_2 \times rand_2 \times \left(x_{best}^{(k)} - x_j^{(k)}\right) \tag{25}$$

$$x_j^{(k+1)} = x_j^{(k)} + v_j^{(k+1)} \tag{26}$$

In Equation (25), the coefficients (c_1), (c_2), and(w) are recognized as the tuning parameters of the particle swarm optimization algorithm. Modifying these parameters can enhance the algorithm's proficiency in problem-solving at certain points. Typically, based on empirical evidence, suitable values for (c_1), (c_2), and (w) are 2, 2, and 0.7, respectively. This formula indicates that the velocity of each particle is determined by its deviation from the target position. Subsequently, Equation (26) calculates the particle's new location. The subsequent step involves evaluating the fitness function for the new positions of the particles and assessing the convergence criteria. It's important to note that these steps are iteratively refined to achieve convergence. For this study, the

objective function, or fitness criterion, for the particle swarm optimization is defined as the mean squared error (MSE), detailed in Equation (27):

$$MSE = \frac{1}{nT}\sum_{i=1}^{n} e(K)^2 \tag{27}$$

where $(e(k))$ represents the total number of samples, and (T) denotes the sampling time. (e) signifies the deviation between the reference rotor current and its actual value in the (d) direction, the difference between the reference electromagnetic torque and its actual value under Sliding Mode Control (SMC), and the disparity between the reference rotor speed and its actual speed. It is important to highlight that, as illustrated in Figure 2, the output of this process consists of the decision variables, which serve as reference signals for the torque, rotor current, and rotor speed.

3. Numerical results

In this section, the capability of the scheme is investigated. Hence, the case study is introduced first, and then, the obtained results are expressed.

3.1. Study case

The system under consideration is integrated into a 2 MW wind turbine. It's important to note that the characteristics of its generator and the aerodynamic components are detailed in Table 1. Additionally, it is assumed that the turbine experiences no friction, leading to the friction coefficient (K_t) being set to zero. Moreover, the optimal settings for the Particle Swarm Optimization (PSO) algorithm, namely the inertia weight (w), and the acceleration coefficients (c_1) and (c_2), are chosen to be 0.7, 2, and 2, respectively, as per Ref. [23]. The algorithm is configured with a population size of 20 and is set to run for 100 iterations.

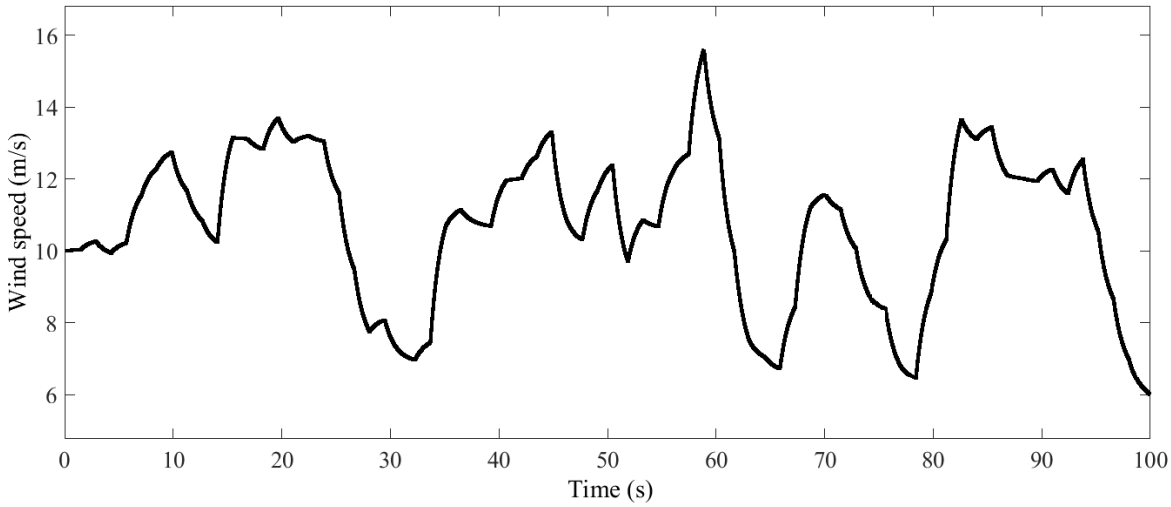

Figure 4. Time graph of wind speed.

Table 1. Wind turbine parameters.

Parameters	Values
K_t	0
J_t	$4.4532 * 10^5 Kgm^2$
ρ	1.225 kg/m^3
R	37.5m
τ_β	0.1

The performance of the wind turbine is significantly influenced by wind speed, making it a critical input parameter. In this study, the wind speed considered for the turbine is depicted in Figure 4. As illustrated, the wind speed fluctuates widely within both high and low-speed ranges, introducing a random element that tests the system's resilience across these conditions. The wind speeds range from 7 to 16 meters per second. It's important to clarify that such variability represents an extreme scenario unlikely to occur in practice. Rapid and severe changes in wind speed are rare in real-life conditions and are employed here solely to assess the robustness of the control system under challenging circumstances.

3.2. Results

The results depicted in Figures 5 to 9 showcase various parameters: the input time curve of the bending angle, bending angle itself, aerodynamic power, aerodynamic torque, turbine absorption coefficient, rotor speed, rotor flux in the q and d directions, generator torque, and the generator output voltage along the d and q axes. An examination of Figure (5-a) and a comparison with Figure 4 reveal that an increase in wind speed, or when the wind speed is notably high, triggers a control input signal for the bending angle, whereas this signal remains zero in conditions of low wind speed.

It is observed from Figure (5-b) that when the bending angle control input signal is engaged or is non-zero, the bending angle changes. This alteration helps in reducing the mechanical stress on the wind turbine, thereby preventing damage to the wind turbine system. Corresponding to the wind speed shown in Figure 4 and the bending angle depicted in Figure (5-b), the daily absorption coefficient curve resembles what is shown in Figure (5-c). From this figure, it is evident that the absorption coefficient consistently registers low values. However, due to variations in wind speed, the absorption coefficient curve is also subject to change over time. Nonetheless, as illustrated in Figures (5-d) and (5-e), the wind turbine exhibits high aerodynamic power and torque. It is important to note that, in many instances, the rotor speed difference relative to its reference speed diminishes, as shown in Figure 6.

Figures (7-a) and (7-b) display the rotor current curves in the q and d directions, respectively. It is important to note that the current in the d direction correlates with the reactive power of the turbine, which remains constant regardless of wind speed; hence, the rotor current in the d direction remains constant. Conversely, the flow in the q direction is tied to the aerodynamic power and, thus, varies in accordance with wind

speed. Consequently, the generator's output active power, which depends on the rotor current in the q direction, also fluctuates over time, as depicted in Figure 8. The last graph showcases the stator voltage in the d and q directions, presented in Figure 9.

From the figure, it's evident that the output voltage fluctuates over time, reflecting variations in wind speed. This phenomenon is attributed to the need for the rotor current in the q-direction to align closely with its reference signal, minimizing the error rate.

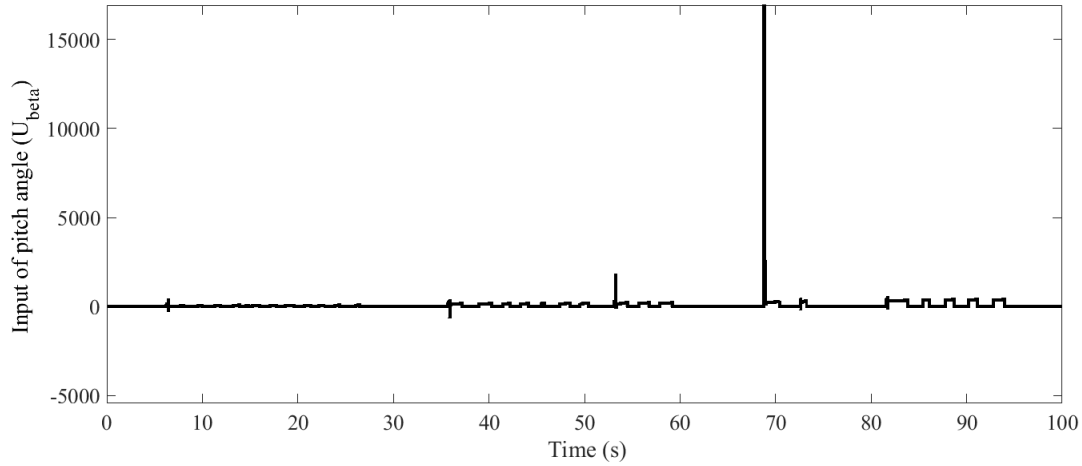

(a)

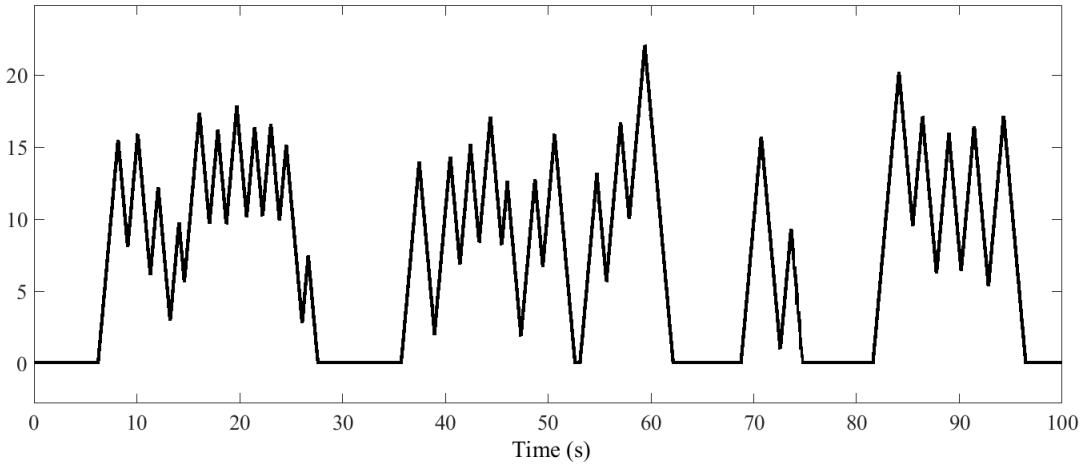

(b)

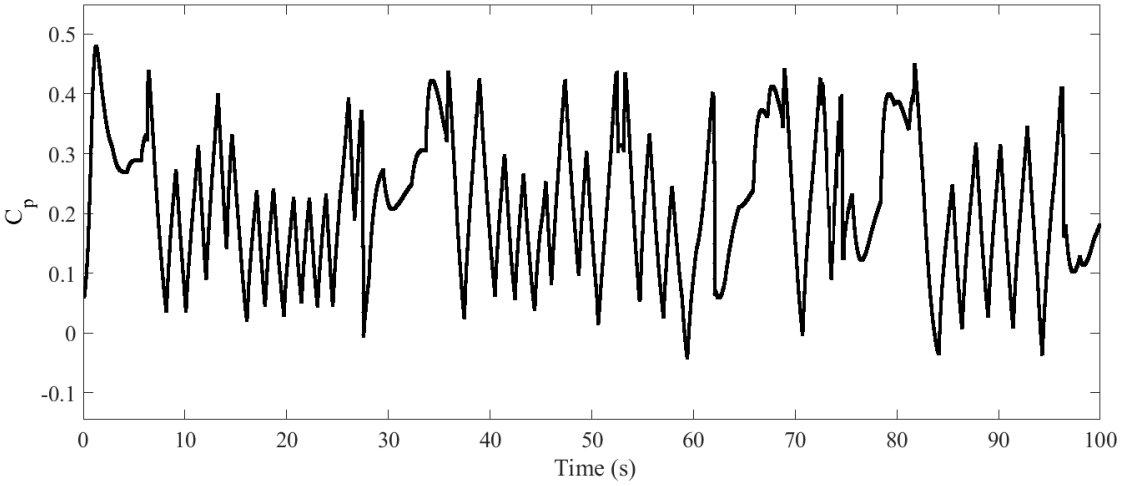

(c)

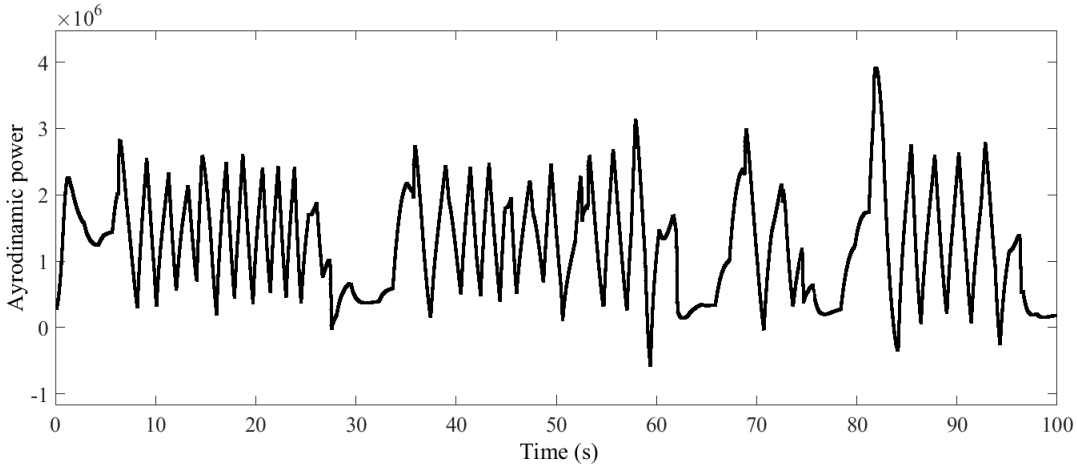

(d)

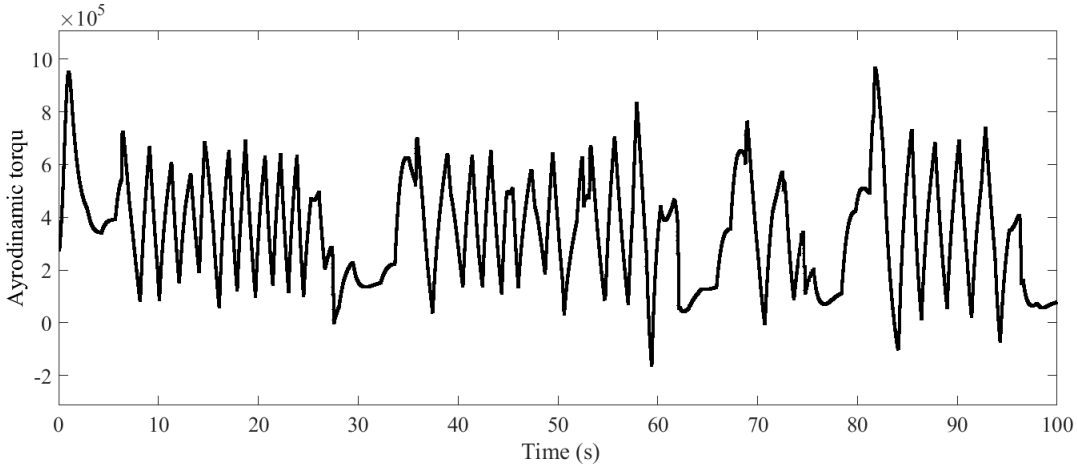

(e)

Figure 5. Time diagram, a) Bending angle input, b) Bending angle, c) Turbine absorption coefficient, d) Turbine aerodynamic power, e) Turbine aerodynamic torque.

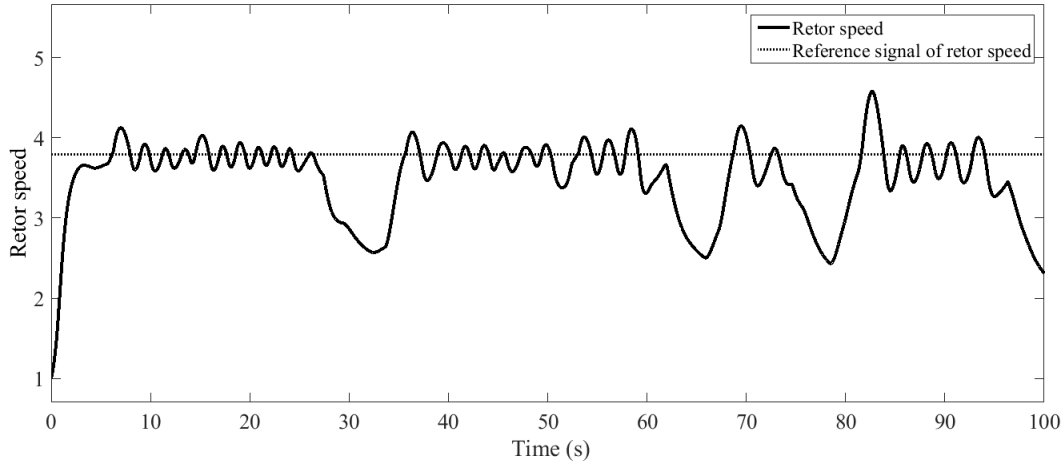

Figure 6. Time graph of real speed and rotor reference.

Consequently, the reference signal for the rotor current in the q-direction changes with wind speed, necessitating adjustments in the rotor current to match wind speed fluctuations. This adjustment leads to changes in the generator's output voltage.

Table 2 details the mean square error deviations for the control strategies under review: one employing solely sliding mode control and another combining sliding mode control with the PSO algorithm. The data indicate that the mean square error is significantly reduced in the design that integrates sliding mode control with the PSO algorithm, showcasing a notable advantage of the proposed design.

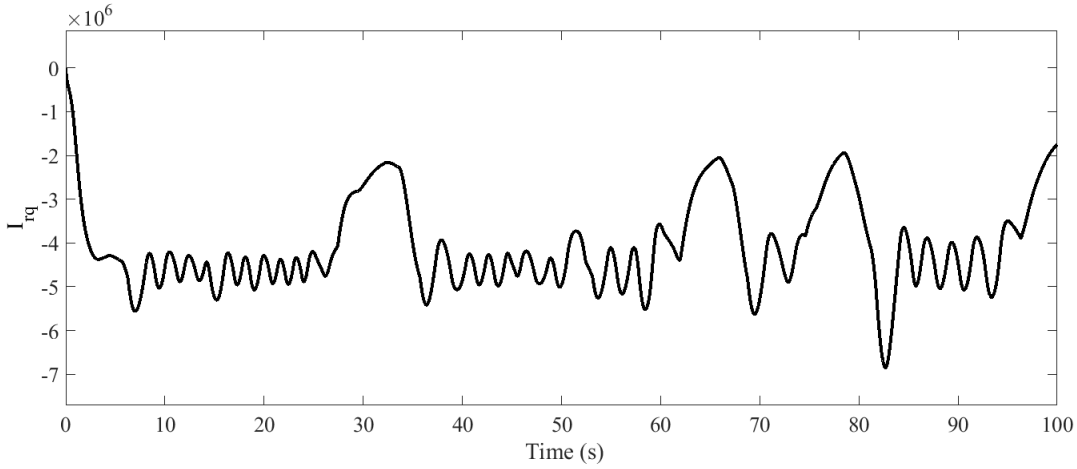

(a)

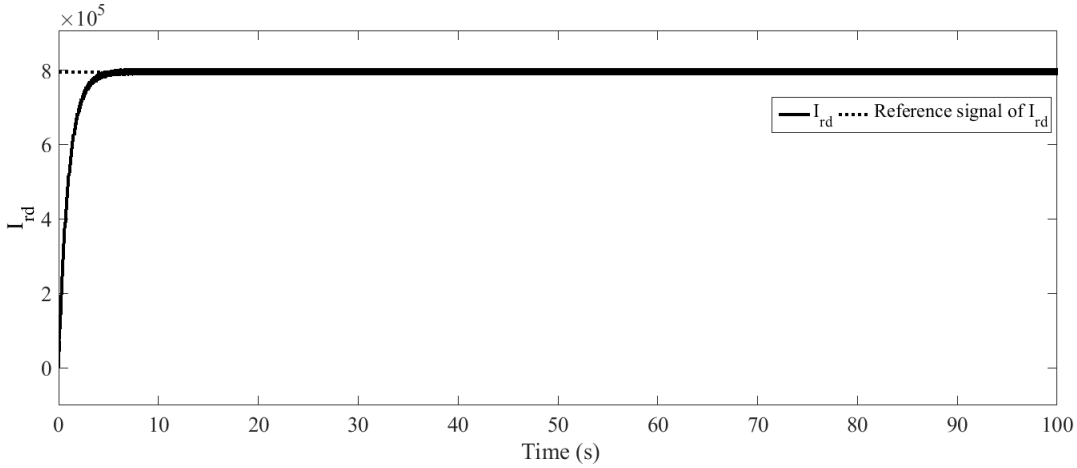

(b)

Figure 7. Time diagram, a) rotor current in direction q, b) rotor current in direction d.

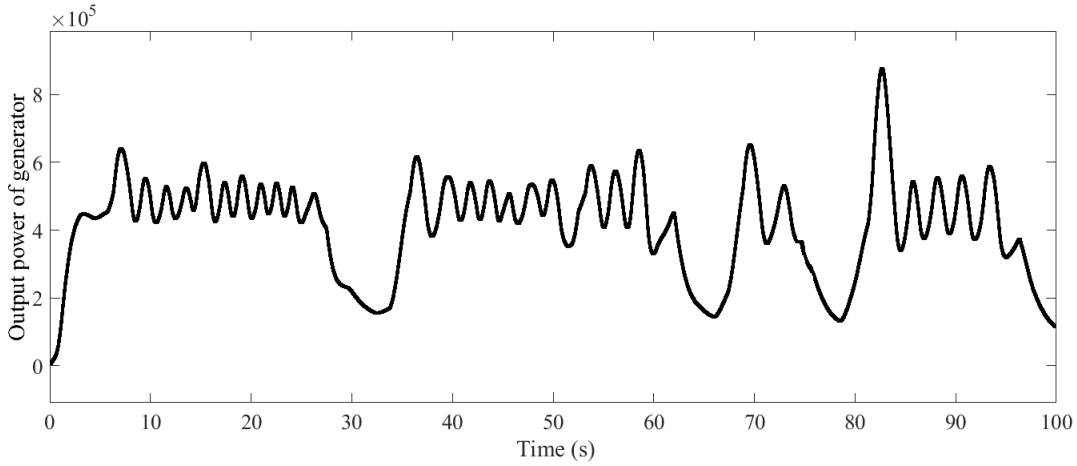

Figure 8. Time diagram of active generator power.

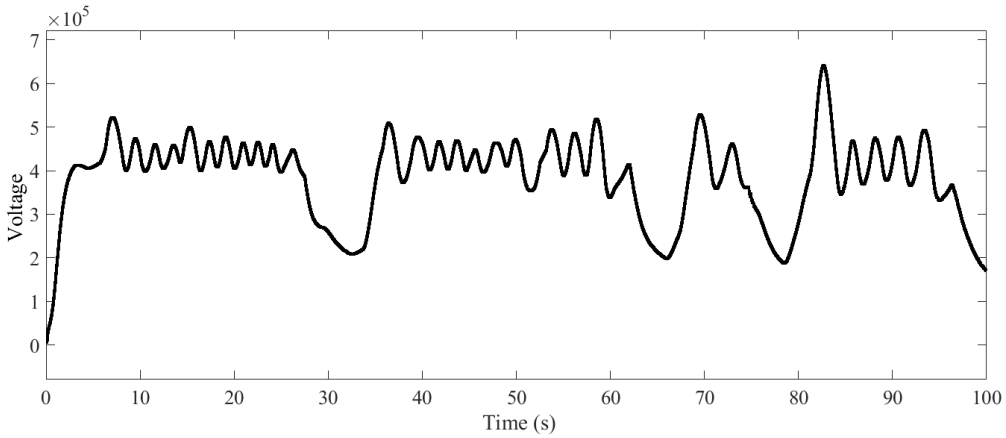

(a)

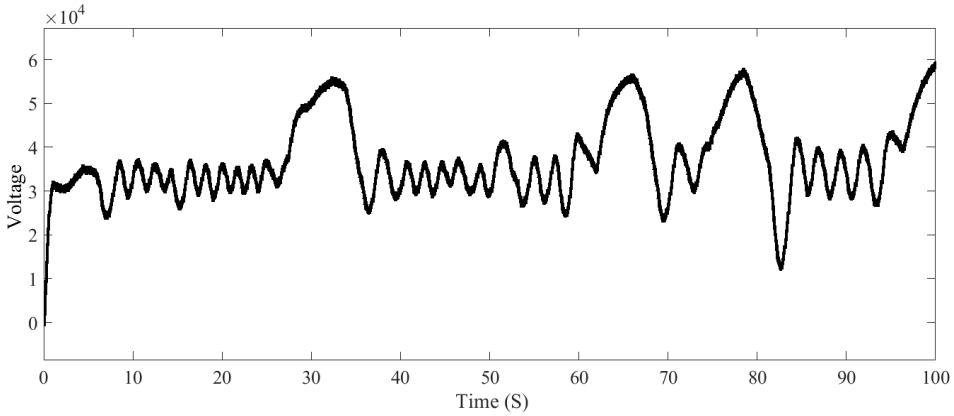

(b)

Figure 9. Time diagram of the output voltage of the stator, a) in the direction of d, b) in the direction of q.

Table 2. Mean square error deviations for different study cases.

Level	Study case
34/12	Proposed design with sliding mode control
57/8	The proposed combination of sliding mode control and PSO algorithm

4. Conclusion

In this paper, the wind turbine model is a combination of sliding mode and PSO algorithm. In the turbine model, the aerodynamic part and its generator were considered. Then the first-order sliding mode controller was presented on the proposed system. Finally, the PSO was applied to minimize the error correction between the reference signal of the control variables and the variables themselves. Then, the proposed problem was applied to a standard wind turbine and based on the numerical results, the following general results were obtained:

- Increasing blade bending angle at high-speed winds to reduce mechanical stress and damage mechanical flexibility
- The input signal of bending angle control at speed is zero the low wind was due to the lack of high mechanical pressure

- The low absorption coefficient of the wind turbine due to the proper control of the blade bending angle at speed upwind
- Changes in aerodynamic power and moment proportional to time and their dependence on wind speed and blade bending angle I see
- Excellent tracking of the rotor current in the *q* direction with minimal error when using a combination of sliding mode control and PSO algorithm
- Excellent tracking of the rotor current in the *d* direction with minimal error when using a combination of sliding mode control and PSO
- Dependence of the rotor current in the *q* direction on the wind speed due to the dependence of the rotor current in the *q* direction on the active generator power
- The lack of dependence of the rotor current in the *d* direction on the wind speed is due to the dependence of the rotor current in the *d* direction on the reactive power of the generator.
- Generator output voltage changes proportional to wind speed to properly control the rotor current in *q* and *d* directions
- A low mean square error (MSE) if a combination of sliding mode control and PSO algorithm is adopted.

References

[1] H. Liang, and S. Pirouzi, "Energy Management System Based on Economic Flexi-Reliable Operation for the Smart Distribution Network Including Integrated Energy System of Hydrogen Storage and Renewable Sources," *Energy*, vol. 293, 130745, 2024.

[2] F. Khalafian, and N. Iliaee, et al., "Capabilities of Compressed Air Energy Storage in the Economic Design of Renewable Off-Grid System to Supply Electricity and Heat Costumers and Smart Charging-Based Electric Vehicles," *Journal of Energy Storage*, vol. 78, pp. 109888, 2024.

[3] S. Pirouzi, "Network-Constrained Unit Commitment-Based Virtual Power Plant Model in the Day-Ahead Market According to Energy Management Strategy," *IET Generation, Transmission & Distribution*, vol. 17, no. 22, pp. 4958-4974, 2023.

[4] B. Wu, Y. Lang, N. Zargari, and S. Kouro, "*Power Conversion and Control of Wind Energy Systems,*" vol. 74. John Wiley & Sons, 2011.

[5] E. Strantzali, and K. Aravossis, "Decision Making in Renewable Energy Investments: A Review," *Renewable and Sustainable Energy Reviews*, vol. 55, pp. 885-898, 2016.

[6] L. Wang, R. Bergua, et al., "Experimental Investigation of Advanced Turbine Control Strategies and Load-Mitigation Measures with a Model-Scale Floating Offshore Wind Turbine System," *Applied Energy*, vol. 355, pp. 122343, 2024.

[7] N. J. Abbas, J. Jasa, D. S. Zalkind, A. Wright, and L. Pao, "Control Co-Design of a Floating Offshore Wind Turbine," *Applied Energy*, vol. 353, pp. 122036, 2024.

[8] S. Saravanan, and N. R. Babu, "Maximum Power Point Tracking Algorithms for Photovoltaic System–A Review," *Renewable and Sustainable Energy Reviews*, vol. 57, pp. 192-204, 2016.

[9] B. Beltran, M. E. H. Benbouzid, and T. Ahmed-Ali, "High-Order Sliding Mode Control of a Dfig-Based Wind Turbine for Power Maximization and Grid Fault Tolerance," *IEEE International Electric Machines and Drives Conference*, pp. 183-189, 2009.

[10] B. Beltran, T. Ahmed-Ali, and M. E. H. Benbouzid, "High-Order Sliding-Mode Control of Variable-Speed Wind Turbines," *IEEE Transactions on Industrial Electronics*, vol. 56, no. 9, pp. 3314-3321, 2008.

[11] X. Yang, and X. Liu, "Integral Variable Structure Fuzzy Adaptive Control for Variable Speed Wind Power System," *International Conference on Logistics Systems and Intelligent Management (ICLSIM)*, vol. 2, pp. 1247-1250, 2010.

[12] O. A. Morfin, A. G. Loukianov, J. M. Cañedo, and M. I. Castellanos, "Velocity Controller of a Wound Rotor Induction Generator via Block Control Linearization-Second Order Sliding Modes," *International Conference on Electrical Engineering Computing Science and Automatic Control*, pp. 77-82, 2010.
[13] C. Evangelista, F. Valenciaga, and P. Puleston, "Active and Reactive Power Control for Wind Turbine Based on a MIMO 2-Sliding Mode Algorithm with Variable Gains," *IEEE Transactions on Energy Conversion*, vol. 28, no. 3, pp. 682-689, 2013.
[14] G. L. Hou, R. Wang, and J. Zhang, "The Application of Integral Variable Structure Control in Cutting-in Control of Double-Fed Induction Generator," *2009 4th IEEE Conference on Industrial Electronics and Applications,* pp. 3152-3157, 2009.
[15] L. Zhang, E. Chunliang, H. Li, and H. Xu, "A New Pitch Control Strategy for Wind Turbines Base on Quasi-Sliding Mode Control," *2009 International Conference on Sustainable Power Generation and Supply*, pp. 1-4, 2009.
[16] X. Fei, H. X. Wang, and M. Chen, "A Novel Sensorless Control of PMSG Based on Sliding Mode Observer," *The XIX International Conference on Electrical Machines - ICEM 2010,* pp. 1-4, 2010.
[17] L. Shang, and J. Hu, "Sliding-Mode-Based Direct Power Control of Grid-Connected Wind-Turbine-Driven Doubly Fed Induction Generators Under Unbalanced Grid Voltage Conditions," *IEEE Transactions on Energy Conversion, vol. 27, no. 2, pp. 362-373,* 2012.
[18] Y. Kumar, J. Ringenberg, et al., "Wind Energy: Trends and Enabling Technologies," *Renewable and Sustainable Energy Reviews*, vol. 53, pp. 209-224, 2016.
[19] A. Luque, and S. Hegedus, "*Handbook of Photovoltaic Science and Engineering"*. John Wiley & Sons, 2011.
[20] H. Kobayashi, and H. Hatta, "Reactive Power Control Method Between DG Using ICT for Proper Voltage Control of Utility Distribution System," *IEEE Power and Energy Society General Meeting*, pp. 1-6, 2011.
[21] F. Blaabjerg, M. Liserre, and K. Ma, "Power Electronics Converters for Wind Turbine Systems," *IEEE Energy Conversion Congress and Exposition*, pp. 281-290, 2012.
[22] Y. Soufi, S. Kahla, and M. Bechouat, "Particle Swarm Optimization Based Sliding Mode Control of Variable Speed Wind Energy Conversion System," *International Journal of Hydrogen Energy*, vol. 41, no. 45, pp. 20956-20963, 2016.
[23] K. Tan, and S. Islam, "Optimal Control Strategies in Energy Conversion of PMSG Wind Turbine System Without Mechanical Sensors," *IEEE Transactions on Energy Conversion*, vol. 19, no. 2, pp. 392-399, 2004.
[24] J. M. Carrasco, L. G. Franquelo, et al., "Power-Electronic Systems for the Grid Integration of Renewable Energy Sources: A Survey," *IEEE Transactions on Industrial Electronics*, vol. 53, no. 4, pp. 1002-1006, 2006.
[25] D.K. Fidaros, C.A. Baxevanou, T. Bartzanas, and C. Kittas, " Numerical Simulation of Thermal Behavior of a Ventilated Arc Greenhouse During a Solar Day," *Renewable Energy*, vol. 35, no.7, 2010.
[26] R. Pena, J. C. Clare, and G. M. Asher, "Doubly Fed Induction Generator Using Back-to-Back PWM Converters and its Application to Variable-Speed Wind-Energy Generation," *IEE Proceedings - Electric Power Applications*, vol. 143, no. 3, pp. 231-241, 1996.
[27] I. Munteanu, A. I. Bratcu, E. Ceanga, and N.A. Cutululis, "Optimal Control of Wind Energy Systems"*, Towards a Global Approach*, vol. 22, p. 286. London: Springer, 2008.
[28] Y. Del Valle, G. K. Venayagamoorthy, S. Mohagheghi, J. C. Hernandez, and R. G. Harley, "Particle Swarm Optimization: Basic Concepts, Variants and Applications in Power Systems," *IEEE Transactions on Evolutionary Computation*, vol. 12, no. 2, pp. 171-195, 2008.

Declaration of Competing Interest

The authors declare that they have no known competing financial interests or personal relationships that could have appeared to influence the work reported in this paper. The ethical issues, including plagiarism, informed consent, misconduct, data fabrication and/or falsification, double publication and/or submission, redundancy, have been completely observed by the authors.

Credit Authorship Contribution Statement

Sasan Pirouzi: Conceptualization, Formal analysis, Project administration, Supervision, Validation, Roles/Writing - original draft. **Ali Naderi:** Conceptualization, Investigation, Methodology, Resources, Visualization, Writing - review & editing.

Bibliography

Sasan Pirouzi received a BSc degree in electrical engineering from the Technical and Vocational University, Mashhad, Iran, in 2012 and an MSc degree from the Isfahan University of Technology, Isfahan, Iran, in 2014, as well as a PhD from the Shiraz University of Technology (SUTECH), Shiraz, Iran, in 2017. His research interests are power system operation and planning, electric vehicles, DERs and the application of optimization methods in power systems.

Ali Naderi was born in Iran. He is currently a master's student in the field of electrical engineering at Yazd University. His special interests are operation and planning of power systems.

Journal of Green Energy Research and Innovation

Improving the Maximum Power Point Tracking in a Photovoltaic System Based on the Resistance-Predictive Method

Moaiad Mohseni, Alireza Niknam Kumleh, Mehdi Alibakhshi, Mona Sheikhi Abou Masoudi

Highlight

- Enhancing the MPPT by designing and controlling the step-up converter of the PV system
- Ensuring an efficient MPPT by proper calculation of parameters
- Employing predictive control to enhance the speed of MOSFET switching decisions
- Implementing a resistive-predictive step-up converter control

Graphical Abstract

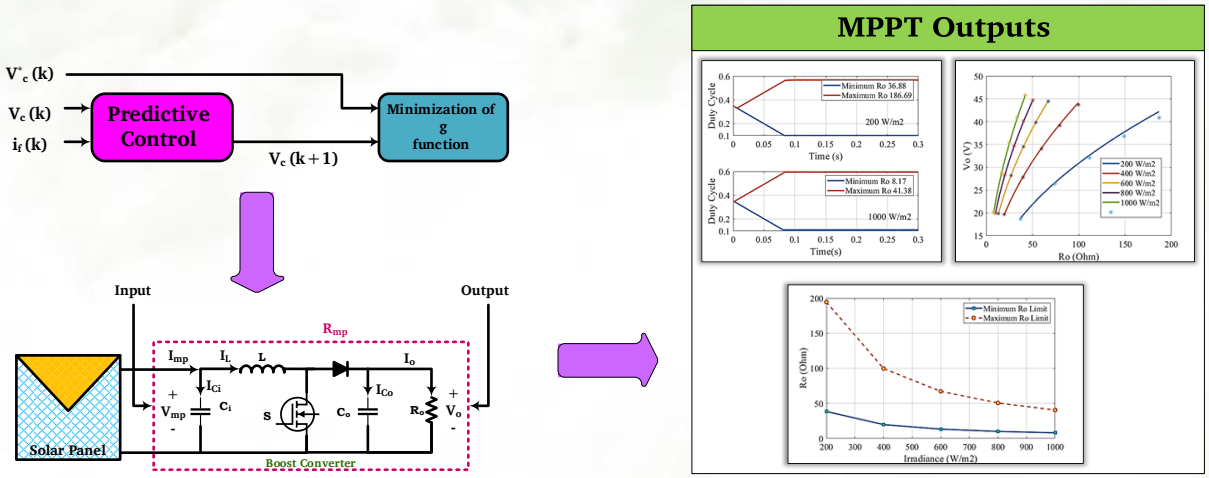

Use your device to scan and read the article online

Citation

M. Mohseni, A. Niknam Kumleh, M. Alibakhshi, and M. Sheikhi Abou Masoudi, "Improving the Maximum Power Point Tracking in a Photovoltaic System Based on the Resistance-Predictive Method," *Journal of Green Energy Research and Innovation*, vol. 1, no. 2, pp. 81-102, 2024.

https://doi.org/10.61186/jgeri.1.2.81

JGERI Journal of Green Energy Research and Innovation

Online ISSN: 3041-9018

Journal of Green Energy Research and Innovation

Journal Homepage: www.jgeri.araku.ac.ir

Improving the Maximum Power Point Tracking in a Photovoltaic System Based on the Resistance-Predictive Method

Moaiad Mohseni [1]*, Alireza Niknam Kumleh [2], Mehdi Alibakhshi [3], Mona Sheikhi Abou Masoudi [4]

[1] *Khuzestan Regional Electric Company, Ahvaz, Iran.*
[2] *Faculty of Electrical Engineering, Amirkabir University of Technology (Tehran polytechnic), Tehran, Iran.*
[3] *Department of Electrical Engineering, Islamic Azad University of Tehran, Tehran, Iran.*
[3] *Department of Electrical Engineering, Naghshejahan Institute of Higher Education, Baharestan, Isfahan, Iran.*

* *Corresponding Author: moaiadmohsenii@gmail.com*

ARTICLE INFO

Keywords:
Boost converter,
Enhancement of MPPT,
Predictive method,
PV system,
Resistance method.

Article history:
Received: 27 January 2024;
Revised: 27 February 2024;
Accepted: 01 March 2024;

Article type:
Research Article

ABSTRACT

An established technique to maximize the output power of photovoltaic (PV) systems, thereby raising the efficiency of renewable energy systems, is maximum power point tracking (MPPT). This paper focuses on designing and controlling a boost converter for MPPT in a PV system to calculate the appropriate range of output resistance, minimum inductance, input capacitor, and output capacitor for the boost converter so that the maximum PV output is achieved and the decision speed of MOSFET switching is obtained by adopting the combined resistance-predictive method. The simulation results demonstrate the efficacy of the proposed method in attaining these objectives. The suggested technique can effectively track the maximum power point (MPP) within a broad spectrum of solar radiation while ensuring that the duty cycle remains within its permissible range.

1. Introduction

1.1. Research Motivation

Solar power will remain a renewable and sustainable energy source because of its superior environmental friendliness and abundant availability. Maximum power point tracking (MPPT) is a technique employed in solar power systems to optimize the extraction of electricity from photovoltaic (PV) modules, which is achieved by closely monitoring the operational state of the modules. To optimize the electricity output from a solar panel, it is essential to use MPPT, particularly in situations where the weather conditions are uncertain [1]. In order to mitigate global warming, it is imperative to substitute hydrocarbon deposit systems with renewable energy sources, such as the sun and wind [2]. To enhance the efficiency of renewable energy systems, PV systems are equipped with an MPPT algorithm to ensure that each module operates at its optimal power point [3]. PV cells exhibit a voltage-current curve that accurately represents their operational state. The maximum power point (MPP) of this curve occurs when the cell generates the highest amount of power to be delivered to a load. The cellular function is

diminished when it is not operational. This paper focuses on the layout and manipulation of a boost converter for MPPT in a PV device. The intention is to calculate the best variety of output resistance, minimal inductance, input capacitor, and output capacitor for the boost converter so that the maximum PV output is achieved and the decision pace of MOSFET switching is obtained by adopting the combined resistance-predictive approach.

1.2. Literature review

There are straightforward techniques to achieve optimal power output in both conventional and dynamic shading scenarios. The MPPT method has been designed to optimize the power output of a solar panel system in the presence of partial shadowing [4]. The topics of discussion in [5] included energy storage, solar production, and optimization of production system dimensioning with storage. Grid-connected PV systems are sized according to the selection of modules, DC/AC inverters, and auxiliary equipment [5]. Reference [6] presents the application of particle swarm optimization (PSO) to maximize the highest power output of PV systems. It also aims to identify the most effective design variable for penalizing the step size of two conventional methods. The authors in [7] propose a bionic two-stage MPPT control method to enhance the precision and speed of the MPPT process. The strategy consists of a fast-positioning stage and a precise determination step, which optimize the duty cycle of the DC-DC converter. The authors in [8] propose a new method to maximize the power output of a PV system by using the Horse Herd Optimization (HHO) algorithm in various weather circumstances. Fault analysis and protection of distributed generations, such as PVs and wind turbines, are also a concern of academia and have been addressed in [9] even though there is a research gap concerning comprehensive work on the protection of PV cells [10].

References [11] and [12] have carefully analyzed the reactions and the electricity production process, accounting for most reasons for changing the behavior of solar panels against weather fluctuations based on the amount of received photon energy and describing the amount of energy gap between the p and n junctions of the semiconductors inside the panel. The most basic model of a PV that has a diode is obtained from these references. The simplest configuration of a PV system incorporating a diode can be derived from these sources. Reference [13] introduces a sophisticated software package that efficiently determines the ideal capacity of PV systems for the electrification of remote and rural areas. The software addresses the challenge of minimizing transportation, electrification, and maintenance expenses. Reference [14] presents a model aimed at optimizing smart homes to enhance the efficiency and reduce energy consumption of electricity generated by PV systems. The outputs of this model will include establishing the composition of walls and windows, calculating the ideal size of panels, and identifying the most suitable location for them. The researchers in [15] developed systems with numerous PVs exhibiting distinct characteristic curves. The primary objective was to ascertain the precise elevation, angle of inclination towards solar radiation, and the most favorable placement for each panel. The full-bridge cascade converter is an inverter widely used in PV systems. It was specifically designed in [16] to

be more robust than its previous versions, offering increased reliability, reduced switching losses, improved efficiency, enhanced short-circuit fault capability, and greater stability in the face of extreme weather fluctuations. Boost converters are extensively employed in PV systems and have seen the development and implementation of multiple structures. The structure described in [17] utilizes a parallel input (parallel input inductors)-series output (series output capacitors) configuration, which has demonstrated excellent efficacy in mitigating current ripple. In addition, the converter proposed in [18] does not require a transformer and possesses the inherent capability to evenly distribute the power obtained from PV arrays. This converter operates with an input voltage of 24 V and outputs a voltage of 100 V at a frequency of 100 kHz. It is specifically built to handle a nominal power of 60 W. Reference [19] presents the design and construction of a multi-level inverter that connects PV arrays to the grid. This inverter has a modular and extendable structure and allows for adding a stabilizer to each panel. The PV units with numerous panels are typically categorized into two types of equivalent circuits: a) single-unit models and b) multi-unit models. In the former type, all panels are treated as a complete unit connected to the grid via a single transformer and impedance. This approach necessitates a few computations and has garnered recommendations from numerous international standard organizations. However, when the panels are situated in significantly distinct geographical locations, this technique exhibits a pretty substantial margin of error, rendering it not advisable [20]. The concept of categorizing PV panels into various clusters is introduced in multi-unit models. Each cluster is represented by an equivalent PV unit, which consists of a complete panel, an equivalent impedance, and a comprehensive transformer. In this approach, the PVs in each cluster are assumed to be almost identical, with any minor variations being disregarded. Given the exceptional precision of multi-unit models, this approach is widely employed in numerous simulation studies and analyses of grid-connected solar power facilities. The single-unit model is a distinct type of multi-unit model [21].

Typically, three models have been proposed for solar cells, including the single-diode, two-diode, and multi-diode models. The single-diode model has the fewest physical parameters. As a result, it has widely been employed in numerous studies to depict the voltage-current characteristics of cells using only four or five parameters. This model is highly cost-effective in terms of mathematical and computational resources, but its precision is contingent upon the specific solar cell technology employed. Several studies indicate that this model exhibits a slight bias towards optimism when predicting the behavior of the cell, as it incorporates a higher proportion of solar energy from the sun in its calculations. However, the actual output of the solar cell is lower than the values obtained from these calculations [22]. The two-diode model is a modified version of the single-diode model that distinguishes between two distinct operating modes of the solar cell: the high-voltage mode and the low-voltage mode. The high-voltage mode of this model is identical to the single-diode mode. However, the low-voltage mode is simulated using a separate diode, and the impact of recombination within the solar cell is considered. The two-diode approach is highly appropriate for situations characterized by low levels

of solar radiation or low ambient temperatures. Consequently, it yields more precise outcomes regarding the performance of the solar cell under low radiation situations [23]. The multi-diode model has superior accuracy compared to alternative models, effectively capturing the solar cell's performance throughout varying temperature conditions and radiation levels. This model requires access to diverse facts that must be precisely characterized by measurement under varied conditions, and these items are not readily accessible in several information sheets. This model exhibits a significant computational burden and is not time-efficient, but it has yielded highly favorable outcomes in numerous solar cells [24].

The peak power and voltage levels are not constant and vary in response to temperature and the angle of sun exposure. By monitoring the power output, the PV system can achieve its highest level of efficiency, resulting in reduced operational costs. There exist numerous variations of MPPT methods, typically categorized into two groups: conventional approaches and novel methods relying on computational algorithms [25]. The soft computing-based methods are novel MPPT approaches that encompass the following techniques: a) fuzzy logic control, b) artificial neural network method, c) adaptive neural fuzzy methods, and d) metaheuristic algorithms, such as genetics and differential evolution [26]. Multiple concerns have been identified in the design of the MPP tracker converter. A subject discussed is the investigation of the link between the equivalent resistance of the PV cell, the output resistance of the converter, and its duty cycle. This analysis, referenced as [27], aims to identify the most efficient converter for connecting the solar cell to the load. The design of the MPP tracker converter, as described in reference [28], represents the power electronic converter as a variable resistance. However, the equivalent impedance of the power electronic converter does not include an inductor or capacitor. The MPP tracker converter has traditionally been designed using conventional methods for DC-DC converters connected to voltage sources [29]. However, it is important to note that the solar cell, being fundamentally nonlinear, cannot be regarded as a linear power supply. Hence, this approach will not yield accurate outcomes. Another approach employed in the design of the MPP tracker converter involves the utilization of small-signal analysis [30]. Nonetheless, this analysis does not encompass the function of the inductor and capacitor in the converter. So, it is unfeasible to compute the inductor and capacitor of the converter using this approach. The calculations pertaining to the design of the inductor and capacitor for the MPP tracker converter are available in [31]. The operation mode of the boost converter has always taken into account continuous current, assuming optimum weather conditions. Reference [32] designed a maximum power tracker buck converter operated based on the predictive model control approach. The proposed power point tracking method is the internal inductance method, which is used as the reference signal of the predictive control model. This optimization technique, which is available online, predicts the current and future condition of the system. This strategy has the benefit of a fast transient response and the elimination of disturbances, in contrast to conventional methods.

The authors in [33] presented an MPP tracker boost converter with a maximum power detector. This converter utilizes a mix of perturbation and observation (P&O) method together with the predictive model control method. Simply put, the predictive control system utilizes the MPP as its reference signal. The impact of altering the step size of the tracking method has also been subjected to sensitivity analysis. This strategy offers the benefit of eliminating any instances of overshoots and undershoots that are associated with switching. Reference [34] discusses the incorporation of the P&O MPPT and the prediction model control methods. This method has been implemented in a boost converter that is coupled to a solar cell. The speed of this method in achieving the MPP has been enhanced, and its capacity to control voltage has been boosted as well. The impact of variations in irradiation and ambient temperature on the suggested method has been examined, and the method has been successfully deployed in real-time. References [35-37] introduce a resilient controller for accurately tracking the MPP of a single-phase multilevel inverter. This is achieved by the use of a predictive control model, resulting in enhanced P&O techniques. Previous methods have been surpassed in efficiency and speed of the control loop, resulting in reduced switching losses as well.

1.3. The significance of research

Given the expansion of PV technology, its efficient operation is crucial both technically and economically. Furthermore, it is crucial to develop models for converters with the objective of MPPT from a scientific and research perspective. The adoption of predictive control approaches also enables the industrialization of these techniques. This paper aims to enhance MPPT by designing and controlling the step-up converter of the PV system. The range of output resistance, minimum inductance, input capacitor, and output capacitor for the boost converter are calculated to ensure efficient MPPT. Predictive control is employed to enhance the speed of MOSFET switching decisions. The study introduces a novel approach to enhancing the MPPT in a PV system by implementing a resistive-predictive step-up converter control.

1.4. Novelty and main contributions

The novelty of the research lies in calculating the ideal range of output resistance, minimal inductance, input capacitor, and output capacitor for the boost converters so that the maximum PV output is executed and the selection speed of MOSFET switching is received by means of adopting a mixed resistance-predictive method.

The remaining of the paper is as follows. Section 2 describes the suggested model, while Section 3 provides a detailed explanation of the program execution algorithm and Section 4 provides the details of the implementation of simulations.

2. Materials and Approaches

This section first presents the equations related to the solar cell model, its technical specifications, and the topology of the MPP tracker converter. Then, the hill climbing (HC) tracking method is studied, and based on the concept of the predictive control model method, the combination of these two methods is implemented in MPPT.

2.1. PV cell model

As the primary source of energy production in PV systems, the solar cell is of particular importance. The importance of its modeling and the types of models available for it were briefly discussed. This study used the most common and simplest solar cell model, called the single-diode model. It should be noted that this model is mostly used in medium and acceptable levels of irradiation and is not very suitable for applications with poor irradiation. Therefore, a simplifying assumption is to consider the appropriate radiation in the studied time period. If more in-depth studies are needed, two-diode or multi-diode models are recommended to be considered. The equivalent circuit diagram of a single-diode solar cell is shown in Figure 1.

Currents I_{ph}, I_s, and I_{PV} represent the flow of photons, the dark saturation current, and the output current of the cell, respectively. Also, the series and shunt resistance of the cell are represented by R_s and R_{sh}, respectively. As is known, the relationship between the PV voltage and the current is not linear due to the presence of the diode. Using the KVL laws, the relationship between the voltage and current of the PV cell [31,38] is represented by Equation (1):

$$I_{PV} = I_{ph} - I_s\left(e^{\frac{(V_{PV}-I_{PV}R_s)}{AV_T}} - 1\right) - \frac{(V_{PV} - I_{PV}R_s)}{R_{sh}} \quad (1)$$

where V_T is the thermal voltage obtained based on Boltzmann's constant, the temperature of the p-n junction, and the electric charge of the electron according to Equation (2):

$$V_T = \frac{kT}{q} \quad (2)$$

For each voltage, Equation (3) must be solved to reach the current-voltage characteristic curve of a PV. In this equation, the photon current shows the dependence of the problem on solar radiation. The dark saturation current also shows the dependence of the equation on the ambient temperature. The MPP is usually obtained by adjusting two series and shunt resistors. The calculation of photon currents and dark saturation is obtained based on the information in the datasheet of each solar cell based on Equations (2) and (3) [21, 31]:

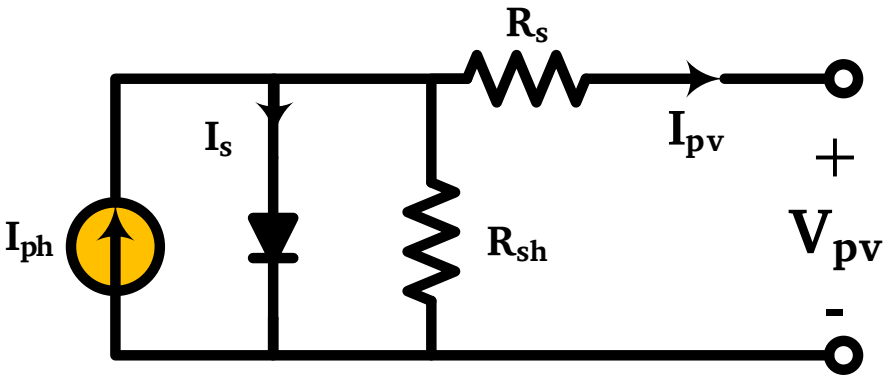

Figure 1. The single-diode model of a PV cell [21].

$$I_{ph} = \frac{G}{G_{stc}}(I_{stc} + K_i(T - T_{stc}) \quad (3)$$

$$I_s = \frac{I_{sc} + K_i(T - T_{stc})}{e\left(V_{oc} + \frac{k_v(T - T_{stc})}{AV_T}\right) - 1} \quad (4)$$

where G is the solar radiation, STC shows the standard test conditions, G_{stc} is the radiation in standard conditions, K_i denotes the temperature coefficient of short-circuit current, T_{stc} is the temperature in standard conditions, and k_v expresses the temperature coefficient in open-circuit voltage.

Based on the characteristic curve of solar cells, the voltage-to-current ratio of the cell can be observed at the operating point of maximum power, and by dividing the cell voltage by its current, the equivalent resistance of the circuit can be obtained from the point of view of the solar cell. If there is no change in the amount of solar radiation or temperature conditions, this value will remain almost constant. Therefore, the equivalent resistance from the PV point of view at the maximum power operating point will be given by Equation (5):

$$R_{mp} = \frac{V_{mp}}{I_{mp}} \quad (5)$$

Since it is possible to use PVs in different radiations and temperatures, the resistance equivalent of the MPP must be obtained over a range of radiations. Also, a range for the minimum and maximum values of resistance equivalent to MPP should be considered so that the design of the boost converter can have an acceptable efficiency.

2.2. Circuit analysis of an ideal boost converter for MPPT purposes

The circuit schematic of an MPP tracker boost converter is shown in Figure 2. As shown, the input side of the converter is connected to the solar cell, and the other side is connected to the load. If the boost converter is assumed to be ideal, i.e., no losses are considered for switching this converter, based on the law of energy conservation, it can be said that the input power of the converter is equal to its output power, so it can be written as Equation (6) [31]:

$$P_{input} = P_{output} \rightarrow \frac{V^2{}_{mp}}{R_{mp}} = \frac{V^2{}_o}{R_o} \quad (6)$$

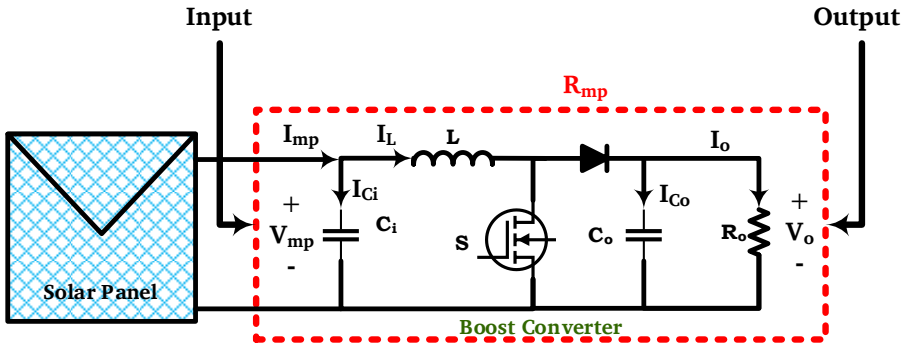

Figure 2. Circuit schematic of a boost converter for MPPT purposes [31].

Because the purpose is the operation and control of the boost converter in the continuous current area, a linear relationship is established between the input and output voltage of the boost converter based on the duty cycle, as given in Equation (7):

$$V_o = \frac{V_{mp}}{1 - D} \tag{7}$$

Therefore, by replacing Equation (7) in Equation (6), the relationship given in Equation (8) is obtained.

$$R_o = \frac{R_{mp}}{(1 - D)^2} \tag{8}$$

The required duty cycle of the boost converter control is provided in Equation (9).

$$R_o = \frac{R_{mp}}{(1 - D)^2} \tag{9}$$

Therefore, the duty cycle is somehow dependent on the relationship between the equivalent resistance of the solar cell and the output resistance of the boost converter and is determined based on its ratio.

2.2.1. Determining the range of output resistor

It is assumed that the radiation is at its lowest permissible limit. In other words, it is placed at the highest value of its permissible range. In such a situation, the duty cycle can also change from D_{min} to D_{max} as its allowed value. In this case, the minimum and maximum values of the output resistance are obtained nu Equations (10) and (11), respectively [34]:

$$R_o^{min} = \frac{R_{mp}^{max}}{(1 - D_{min})^2} \tag{10}$$

$$R_o^{max} = \frac{R_{mp}^{max}}{(1 - D_{max})^2} \tag{11}$$

On the other hand, assume that the solar radiation is at its maximum value; that is, R_{mp} is at the lowest value of its allowed range, i.e., R_{mp}^{min}. In such a situation, the duty cycle can also change from D_{min} to its allowed value of D_{max}. In this case, the minimum and maximum values of the output resistance are calculated by Equations (12) and (13), respectively:

$$R_o^{min} = \frac{R_{mp}^{min}}{(1 - D_{min})^2} \tag{12}$$

$$R_o^{max} = \frac{R_{mp}^{min}}{(1 - D_{max})^2} \tag{13}$$

2.2.2. Sizing the inductance

According to Figure 2, when the power switch is closed (when the switch is on), the inductor starts charging and the voltage of the two ends of the solar cell is placed in the

two ends of the inductor ($V_L = V_{mp}$). The turn-on duration of the switch is also $\Delta t = DT_s$s. Therefore, the current of the inductor starts to increase from its initial value, and the value of this increase based on the relationship between the voltage and current of the inductor (Faraday's law) will be equal to Equation (14):

$$V_L = L\frac{\Delta i_L}{\Delta t} \rightarrow \Delta i_L = \frac{DT_s}{L}V_{mp} = \frac{D}{f_s L}V_{mp} \tag{14}$$

Equation (14) determines the ripple value of the inductor current. On the other hand, since the average current passing through the capacitors is equal to zero, the average current of the inductor will be equal to the average current of the solar cell, so Equation (15) is established:

$$I_L = I_{mp} \tag{15}$$

The boundary between discrete and continuous operation is when the current ripple $\boldsymbol{\Delta i_L}$is equal to the average current of the inductor $\boldsymbol{I_L}$. So, Equation (16) is established as follows:

$$I_L = \Delta i_L \rightarrow I_{mp} = \frac{DT_s}{I_{mp}}V_{mp} \rightarrow L = \frac{DT_s}{I_{mp}}V_{mp} \rightarrow L = \frac{D}{f}\frac{V_{mp}}{I_{mp}} \tag{16}$$

As it is known, the value of the inductor in the critical state can be determined based on the voltage and current of the maximum power point of the cell. The ratio $\frac{\boldsymbol{V_{mp}}}{\boldsymbol{I_{mp}}}$ is the same equivalent resistance ($\boldsymbol{R_{mp}}$) of the solar cell. Therefore, we can have [33]:

$$L = \frac{D}{f_s}R_{mp} \rightarrow L = \left(1 - \sqrt{\frac{R_{mp}}{R_o}}\right)\left(\frac{R_{mp}}{f_s}\right) \tag{17}$$

According to Equation (17), it can be said that determining the inductor value is a function of three parameters: solar cell resistance, switching frequency, output resistance, and duty cycle. To better understand, Figure 3 shows the depiction of the two equations given in Equation (17).

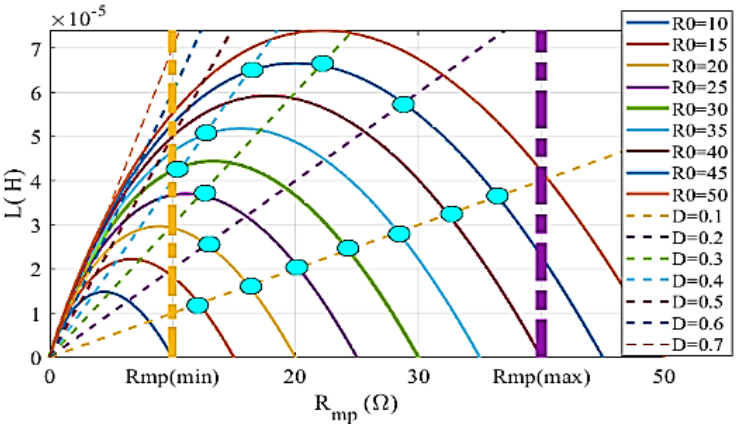

Figure 3. Inductance value based on solar cell resistance, output resistance, and duty cycle [33].

Figure 3 shows the relationship between the inductor and the resistance of the solar cell in different output resistances, and the lines with constant slopes represent the same relationship but in different duty cycles. From the intersection of these curves, the required inductor values of the boost converter are determined. The lowest allowed value for L is when the resistance of the solar cell and the diode cycle are at their minimum. So, we will have Equation (18):

$$L_{min} = \frac{D_{min}}{f_s} R_{mp}^{min} = \left(1 - \sqrt{\frac{R_{mp}}{R_o}}\right) \frac{R_{mp}}{f_s} \tag{18}$$

The peak point of the curves in Figure 3 can be obtained by differentiation of Equation (17). If it is assumed that R_o is constant, then by differentiating Equation (17) with respect to the variable R_{mp} and setting it to zero, we will have Equation (19):

$$\frac{dL}{dR_{mp}} = \frac{d}{dR_{mp}}\left(1 - \sqrt{\frac{R_{mp}}{R_o}}\right)\frac{R_{mp}}{f_s} + \left(1 - \sqrt{\frac{R_{mp}}{R_o}}\right)\frac{d}{dR_{mp}}\left(\frac{R_{mp}}{f_s}\right) \tag{19}$$

By applying derivation and simplifying the results, Equation (20) is obtained:

$$\left(-\frac{1}{2}\sqrt{\frac{1}{R_o R_{mp}}}\right)\frac{R_{mp}}{f_s} + \left(1 - \sqrt{\frac{R_{mp}}{R_o}}\right)\frac{1}{f_s} = 0 \rightarrow 1 - \frac{3}{2}\sqrt{\frac{R_{mp}}{R_o}} = 0 \tag{20}$$

Therefore, by solving Equation (20) and replacing it in Equation (17), Equation (21) is obtained as follows:

$$\frac{R_{mp}}{R_o} = \frac{4}{9} \rightarrow L = \frac{1}{3}\frac{R_{mp}}{f_s} \tag{21}$$

2.2.3. Determining the duty cycle

The permissible duty cycle range is determined by assuming that the output voltage of the boost converter is constant and its current is continuous as given in Equation (22):

$$D = 1 - \frac{V_{mp}}{V_o} \rightarrow D_{min} = 1 - \frac{V_{mp}^{max}}{V_o}, D_{max} = 1 - \frac{V_{mp}^{min}}{V_o} \tag{22}$$

2.2.4. Sizing the input capacitor

The input capacitor is used to reduce the input fluctuations of the boost converter. This capacitor is placed in parallel with the solar cell. If the capacitor is not present, the current passing through the cell changes greatly with a small change in the cell voltage based on the characteristic curve, and the cell may be far away from the MPP [39]. If the voltage of the solar cell changes, the electric charge changes in the capacitor, and an opposite current is generated in the capacitor, which is obtained from Equation (23):

$$\Delta I_c = C_i \frac{\Delta V_{mp}}{\Delta t} \tag{23}$$

Hence, the size of the input capacitor is provided by Equation (24) [39]:

$$C_i = \frac{-\Delta I_L \Delta t}{\Delta V_{mp}} = -\left(\frac{D V_{mp}}{f_s L}\frac{\Delta t_1}{\Delta V_{mp}} + \frac{(1-D)(V_{mp} - V_o)}{f_s L}\frac{\Delta t_2}{\Delta V_{mp}}\right) \tag{24}$$

The current passing through the capacitor changes during two-time intervals of $\boldsymbol{\Delta t_1 = \frac{D}{f_s}}$ and $\boldsymbol{\Delta t_1 = \frac{1-D}{f_s}}$, so we have:

$$C_i = \left(\frac{DV_{mp}}{f_s L}\frac{D}{f_s \Delta V_{mp}} + \frac{(1-D)}{f_s L}\frac{DV_{mp}}{1-D}\frac{(1-D)}{f_s \Delta V_{mp}}\right) = \frac{DV_{mp}}{f_s^2 L \Delta V_{mp}} \quad (25)$$

in which the value of the switching frequency is known, so the value of the input capacitor will be the function of the duty cycle, the inductance of the inductor, and the voltage ripple of the solar cell [39].

2.2.5. Sizing the output capacitor

The output capacitor is determined to adjust the output voltage ripple. Usually, when the power switch is ON, the current of the output capacitor is discharged in the resistance, and therefore its voltage changes according to Equation (26):

$$C_o = \frac{DV_o}{fR_o \Delta V_o} \quad (26)$$

2.3. Model prediction control method

The use of MPPT with predictive control is presented in this paper. This is due to the fast dynamic response suitable for controlling this type of system. It can be easily implemented and included in all types of systems, nonlinear constraints and situations, and multivariable cases for control and with easy implementation. The desired behavior of the system is formulated. In this control scheme, the open-loop model is used to predict and select the desired excitation, which provides a predictive horizon for control feedback. This means that only the first element of the optimized excitation sequence is applied and the entire optimization is recalculated at the sampling period. The block diagram of the proposed predictive control system for the system under study is shown in Figure 4.

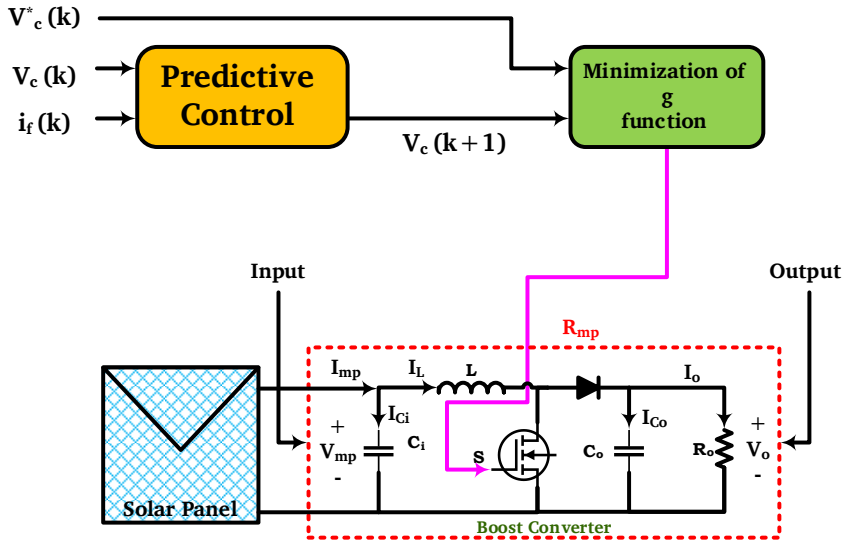

Figure 4. Block diagram of the prediction control [33].

The output voltage $v_c(k)$ and filter current $i_f(k)$ are measured for prediction by Equation (27) [33].

$$x(k+1) = A_q x(k) + B_q v_i(k) + B_{dq} i_o(k) \quad (27)$$

Where:

$$A_q = e^{AT_s}, B_q = \int_0^{Ts} e^{A\tau} B d\tau, and \quad B_{dq} = \int_0^{T_s} e^{A\tau} B_d d\tau. \quad (28)$$

The dynamic behavior of the output voltage can be stated as Equation (29):

$$C\frac{dv_c}{dt} = i_f - i_o \quad (29)$$

where C is the capacitor of the filter.

3. Case Study and Results

3.1. Case Study

The solar cell used in this study is a 50-W monocrystalline panel marketed under the brand name of MartSPM050-M. The specifications are presented in Table 1.

The maximum amount of irradiation in this study is 1000 W/m^2 and its minimum value is 200 W/m^2. Studies have been done with irradiances of 200, 400, 600, 800, and 1000 W/m^2.

3.2. Data of the boost converter

Some parameters are predetermined by the manufacturer or the standards before the design for designing the boost converter. These parameters play an important role in solving the problem. Table 2 presents the technical data required for designing the boost converter.

Table 1. The technical data of the studied PV cell [33].

Parameter	Symbol	Value	Dimension
Open-circuit voltage	V_{OC}	22.53	V
Short-circuit current	I_{SC}	2.97	A
MPP voltage	V_{mp}	18.68	V
MPP current	I_{mp}	2.77	A
Temperature coefficient of the open-circuit mode	K_v	-0.0789	Celsius/V
Temperature coefficient of the short-circuit mode	K_i	0.1485	Celsius/mA
Irradiance in standard conditions	G_{stc}	1000	W/m^2
Temperature in standard conditions	T_{stc}	25	Celsius degree
Boltzmann's constant	k	1.38×10^{-23}	Joule/Kelvin
Charge of an electron	q	1.6×10^{-19}	Coulomb

3.3. Simulation results

3.3.1. Extracting the characteristic curve of the PV cell

The characteristic curve of the solar cell is obtained by Equations (1) to (4) and according to the technical information mentioned in the datasheet of the solar cell (see Table 1). The current-voltage curve of the solar cell is shown in Figure 5. Also, Figure 6 depicts the voltage-power characteristic of the cell. The voltage-resistance characteristic of the solar cell is also depicted in Figure 7.

Table 2. The technical data required for designing the boost converter [33].

Parameter	Symbol	Value
Switching frequency of IGBT	f_s	20
Maximum ripple of the PV cell voltage	$\Delta V_{mp}/V_{mp}$	1
Maximum ripple of the converter output voltage	$\Delta V_o/V_o$	1
Maximum ripple of inductor current	$\Delta I_L/I_L$	15
Minimum allowable duty cycle	D_{min}	10
Maximum allowable duty cycle	D_{max}	60

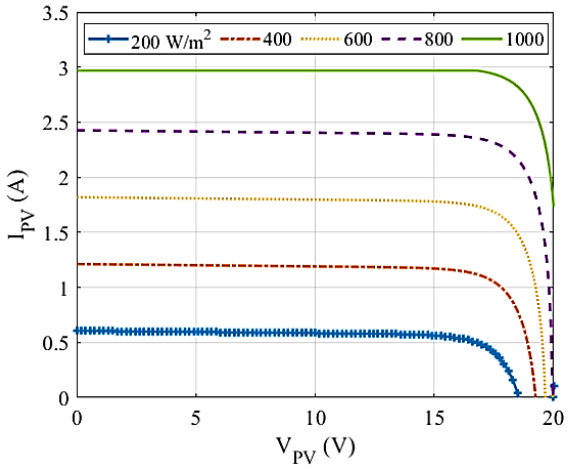

Figure 5. The V-I characteristic curve of the PV cell.

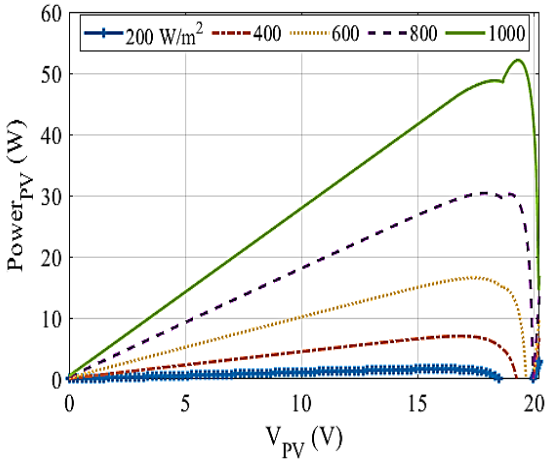

Figure 6. The V-P characteristic curve of the PV cell.

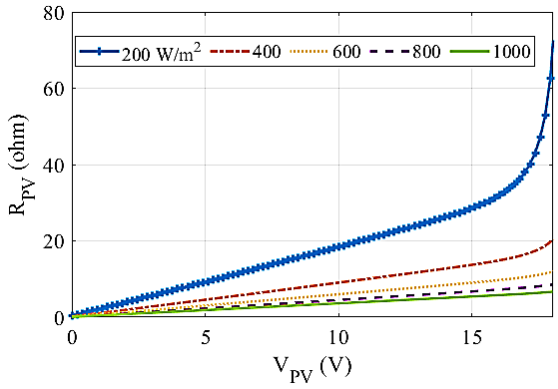

Figure 7. The V-R characteristic curve of the PV cell.

Figure 5 shows the dependence of PV behavior on irradiance. The graphs related to higher irradiation are placed on the top of the other graphs. This means that the higher the irradiation, the larger the short-circuit current. Also, the current corresponding to the MPP will increase. From the point of view of open-circuit voltage, irradiation does not greatly impact the results.

It is inferred from Figure 6 that with the increase of irradiation, the PV power curve is placed above the other graphs. This means that the ability to extract thermal energy has increased and it is possible to obtain more solar power. The voltage of the MPP does not express much changes, but the current supplied by PVs has increased due to irradiation, and as a result, the power has increased.

From the perspective of the equivalent resistance of the solar cell, it can be seen in Figure 7 that the increase in irradiation leads to a decrease in PV resistance, and the lowest amount of resistance belongs to the highest amount of solar radiation. Also, this resistance changes depending on the voltage at both ends of the panel and shows a strictly upward and exponential trend with respect to voltage changes. In order to transfer the maximum power to the load, the impedance must be adjusted and the PV operating point must be determined. These figures, especially Figure 7, give the minimum and maximum resistance values of the solar cell in different radiations. In this study, the minimum resistance of the solar cell is at the MPP, equal to $R_{mp}^{\min} = 6.62\Omega$, which belongs to the irradiation of 1000 W/m^2. The maximum resistance of a solar cell is $R_{mp}^{\max} = 29.87\Omega$, which belongs to the irradiation of 200 W/m^2.

Table 3. The results of designing the boost converter components under three different conditions.

Element	Constant R_o	Limitless R_o	R_o with a forced limit
Output resistance (Ω)	38.996	Rheostat from 8.1728 to 186.68	Rheostat from 8.1728 to 70
Output capacitor (μF)	75.39	111.90	111.90
Inductance (mH)	1.92	5.97	3.45
Input capacitor (μF)	9.54	3.14	3.14

3.3.2. Boost converter design using power control tracking

In this part of the simulation, the behavior of the designed converters is examined from two viewpoints, including:

Scenario 1: The constant output resistance, constant irradiation, and initial duty cycle value are set to 35%. By changing the constant-step duty cycle, the converter tries to track the power point using the HC method, without violating its allowed range.

Scenario 2: The output resistance is variable, the irradiation remains constant, and only the cell output voltage fluctuates by 10%, the constant-step duty cycle tries to adjust the output voltage of the boost converter.

To examine the above scenarios, it is necessary to implement them with MATLAB software. The Simulink toolbox was used to simulate this method. The circuit diagram of the implementation of this converter in MATLAB software is shown in Figure 8.

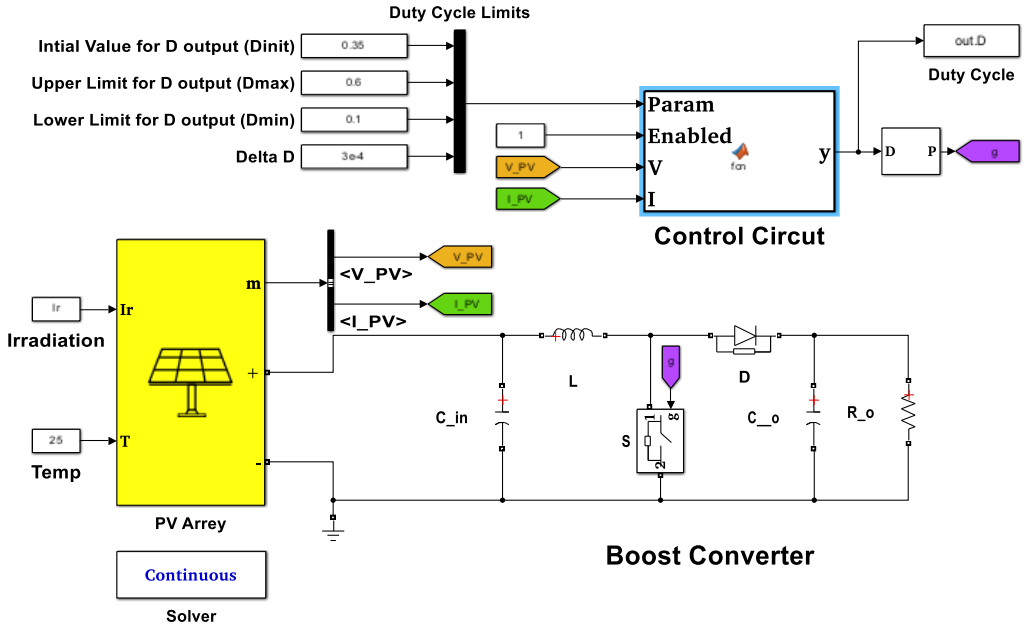

Figure 8. A schematic of the circuit implemented in the Simulink toolbox.

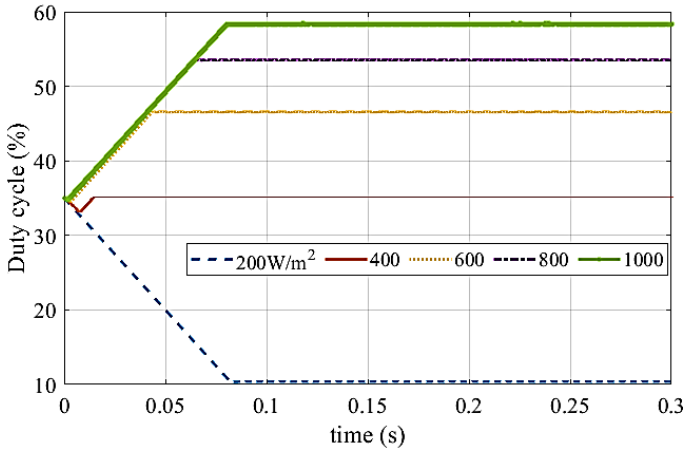

Figure 9. The performance of the power tracking system in achieving the MPP by adjusting the duty cycle at constant output resistance.

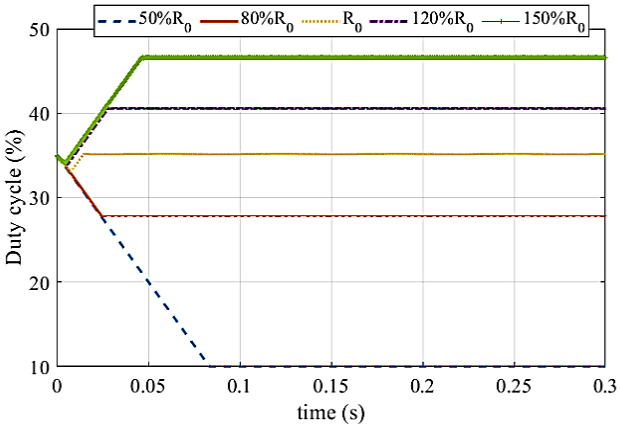

Figure 10. The effect of changing the output resistance (relative to the optimal value) for MPPT in the irradiation of 400 W/m^2.

The amount of radiation remains constant during each simulation, but the voltage of the solar cell and the current passing through it change, and the duty cycle must increase or decrease its value (with a constant step) based on the MPP. In the case that the resistance is constant, only the duty cycle can be effective in the results of the problem. Nonetheless, if the resistance is chosen as a rheostat, changing the resistance can also be used as an auxiliary solution.

Scenario 1 (constant output resistance): Figure 9 shows the performance of the power tracking system for different irradiations. The information about the inductor, capacitors, and output resistance is taken from the information in the first column of Table 3 and applied to the simulation.

Figure 10 illustrates well the result of the distance of the output resistance value from its optimal value. As is evident, the MPP is found faster in the selected optimal value than in other cases. As the distance from the optimal value increases, the time to reach the MPP also increases. The second remark is that changing the value of the output resistance has led to a change in the duty cycle. In the case of irradiation of 400 W/m^2, it can be seen that the duty cycle is not limited. Only if the output resistance is halved (striped blue), the tracking system reaches its limit and the solution will not be very acceptable. The third remark is that the less the irradiation, the higher the possibility of the system not being able to reach the duty cycle. The duty cycle limitation may lead to the lack of access to the correct solution. On the other hand, increasing the output resistance may cause the system to face a high duty cycle limit. Another factor indicating the correctness of the design of the proposed tracking system is examining the amount of input voltage ripple, inductor current ripple, and output voltage ripple in each of the MPPs obtained in the system, which is shown in Table 4.

Scenario 2 (variable output resistance): In this scenario, the output resistance is not constant and is designed based on the second column of Table 3 of circuit elements. The analysis of scenario 2 is also similar to scenario 1, with the difference that the results are not checked only in one output resistance but the justification of the system's behavior in a range of resistances from 8.17 to 186.68 Ω must be investigated. The ability of the system to find the MPP in different ranges of irradiation and output resistance is one of

the important issues. First of all, in the beginning, it should be determined what range of output resistance will be acceptable for each irradiation, and in that determined range, the tracking system can find the MPP suitably.

Table 4. Investigating the technical parameters of the MPP tracker converter in different irradiations (constant output resistance).

Irradiation (W/m²)	Resistance of solar cell	Input voltage ripple in the MPP (%)	Inductor current ripple in the MPP (%)	Output voltage ripple in the MPP (%)
200	32.38	0.2	10.0	0.2
400	16.61	0.63	14.88	0.63
600	11.18	0.79	13.93	0.79
800	8.40	0.93	11.95	0.93
1000	6.75	0.99	10.30	0.99

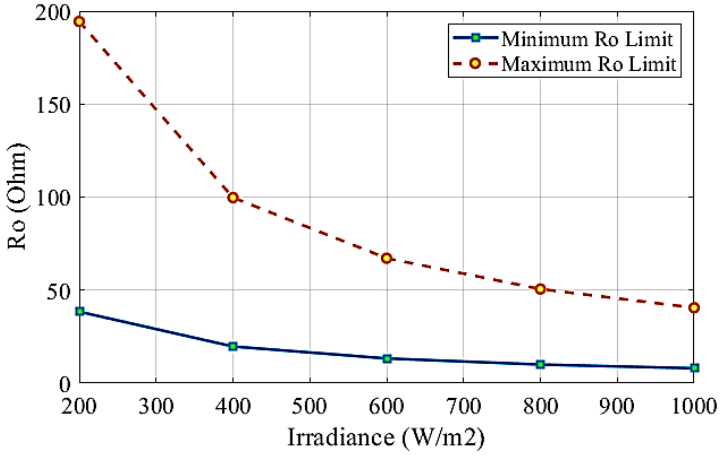

Figure 11. The permissible range of output resistance of the MPP tracker converter in different irradiations.

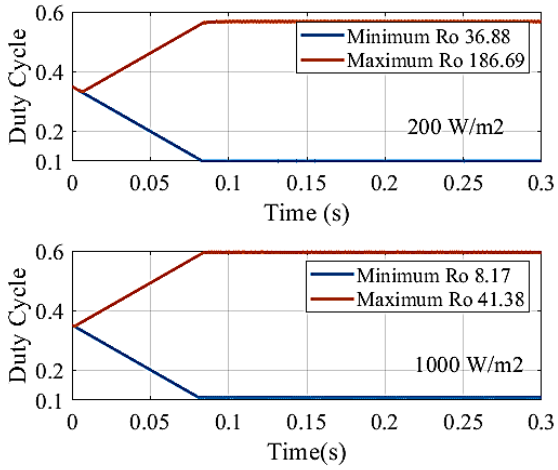

Figure 12. The duty cycle behavior in the upper and lower ranges of the output resistance for irradiations of (a) 200 W/m² and (b) 1000 W/m².

According to Figure 11, it can be concluded that firstly as the irradiation decreases, the minimum and maximum allowed value of the output resistance must increase and it will not be possible to reach the MPP in smaller resistances. The justification for this behavior is given in Equation (8). As it is clear in this equation, when the irradiation is low, the duty cycle needs to be higher to maintain the stability of the system, so the value of the output resistance will be larger. Secondly, the higher the radiation, the smaller the distance between the minimum and maximum allowed output resistance. In other words, the range of permissible variations of the output resistance will be lower. It is also possible to justify this according to Equations (10) to (13). It is clear in these relationships that with the increase in irradiation, the range of duty cycle variations decreases, so the range of output resistance variations becomes narrower. Another essential issue in Scenario 2 is specifying the range of duty cycle variations in each of the irradiations and output resistance limits determined in Figure 12, whose result is displayed in Figure 13.

The cycle should also be less than the allowed value, which will not be acceptable. Also, the higher the irradiation, the higher the duty cycle in a shorter period of time. Calculating the ripples of inductor current and input and output capacitor voltages is another important parameter in understanding the behavior of the power tracker converter, whose results are shown in Table 5. Analyzing the output voltage of the system in different irradiations and the resistance of different outputs is illustrated in Figure 13. According to Figure 11, larger resistances will bring the duty cycle closer to the maximum, and smaller resistances will bring the duty cycle closer to its lower limit.

Table 5. Variations in the ripple of the input voltage, output voltage, and inductor current for different resistances and irradiations.

Irradiation (W/m^2)	Output resistance	Input voltage ripple in the MPP (%)	Inductor current ripple in the MPP (%)	Output voltage ripple in the MPP (%)
200	37.300	0.182	0.529	0.113
	49.734	0.401	4.381	0.180
	73.890	0.558	8.269	0.215
	88.810	0.668	9.897	0.214
	105.151	0.829	11.232	0.191
	131.439	0.872	12.897	0.176
	150.266	0.921	13.811	0.165
	165.543	0.963	14.434	0.158
	8.171	0.215	0.470	0.681
1000	14.920	0.3765	2.001	1.001
	25.222	0.533	2.325	0.810
	38.011	0.803	3.547	0.672

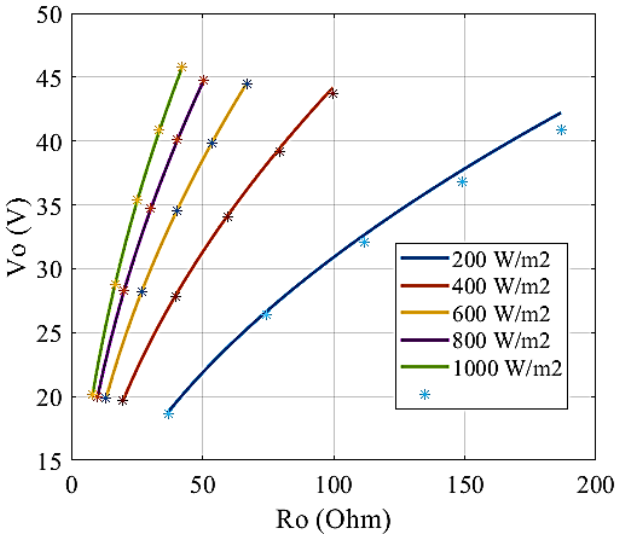

Figure 13. The behavior of the output voltage in different irradiations and output resistances.

4. Conclusions

It can be concluded that the proposed power tracker converter could find the MPP within the designed range of the output resistance so that the duty cycle did not violate its predetermined range. Also, the MPP was found to be highly dependent on the solar irradiance, and since the step related to tracking the power in this method was assumed to be constant, the system tracks the MPP very quickly around irradiation amounts of 400 to 600 W/m2. However, the time to reach the MPP will be longer as the irradiation value deviates further from this range. Moreover, the higher the output resistance, the greater the tendency of the tracking system to move towards larger duty cycles to track the MPP. As the resistance decreases from the optimal value, the duty cycle will move towards its minimum value. The designs showed that the proposed method would lead to maintaining the ripples in the input capacitor voltage, output capacitor voltage, and inductor current within their allowed range. The results demonstrated that the variable resistance method worked in a wider working range than the constant resistance method. Therefore, it would have a more comprehensive performance. Nevertheless, the computational burden of the constant resistance method was less. This method can be used as a simple method for PV energy management. The simulation effects demonstrated the efficacy of the proposed technique in attaining the objectives. The counseled technique can correctly song the MPP inside a vast spectrum of solar radiation while ensuring that the duty cycle remains inside its permissible variety.

References

[1] Z. Ishrat, A. K. Gupta, and S. Nayak, "A Comprehensive Review of MPPT Techniques Based on ML Applicable for Maximum Power in Solar Power Systems," *Journal of Renewable Energy and Environment*, vol. 11, no. 1, pp. 28-37, 2024.

[2] M. Abasi, M. F. Nezhadaneini, M. Karimi, and N. Yousefi, "A Novel Metaheuristic Approach to Solve Unit Commitment Problem in the Presence of Wind Farms," *Rev Roumaine des Sciences Techniques-Series Electrotechnique et Energetique*, vol. 60, no. 3, pp. 253-262, 2015.

[3] K. Fatima, A. F. Minai, and H. Malik, "Intelligent Approach-Based Maximum Power Point Tracking for Renewable Energy System: A Review," *Intelligent Data Analytics for Power and Energy Systems*, pp. 373-405, 2022.
[4] A. G. Abo-Khalil, I. I. El-Sharkawy, A. Radwan, and S. Memon, "Influence of a Hybrid MPPT Technique, SA-P&O, on PV System Performance Under Partial Shading Conditions," *Energies*, vol. 16, no. 2, p.577, 2023.
[5] A. G. Abo-Khalil, K. Sayed, A. Radwan, and I. A. El-Sharkawy, "Analysis of the PV System Sizing and Economic Feasibility Study in a Grid-Connected PV System," *Case Studies in Thermal Engineering*, vol. 45, 102903, 2023.
[6] M. H. Ibrahim, S. P. Ang, et al., "Optimizing Step-Size of Perturb & Observe and Incremental Conductance MPPT Techniques Using PSO for Grid-Tied PV System," *IEEE Access*, vol. 11, pp. 13079-13090, 2023.
[7] L. Gong, G. Hou, and C. Huang, "A Two-Stage Mppt Controller For Pv System Based on the Improved Artificial Bee Colony and Simultaneous Heat Transfer Search Algorithm," *ISA transactions*, vol. 132, pp. 428-443, 2023.
[8] A. Refaat, Q. A. Ali, et al., "Extraction of Maximum Power From PV System Based on Horse Herd Optimization MPPT Technique Under Various Weather Conditions," *Renewable Energy*, vol. 220, 119718, 2024.
[9] M. Sadeghi, and M. Abasi, "Optimal Placement and Sizing of Hybrid Superconducting Fault Current Limiter for Protection Coordination Restoration of the Distribution Networks in the Presence of Simultaneous Distributed Generation," *Electric Power Systems Research*, vol. 201, 107541, 2021.
[10] M. Abasi, M. Joorabian, A. Saffarian, and S.G. Seifossadat, "A Comprehensive Review of Various Fault Location Methods for Transmission Lines Compensated by FACTS Devices and Series Capacitors," *Journal of Operation and Automation in Power Engineering*, vol. 9, no. 3, pp. 213-225, 2021.
[11] F. Rebert, and W. Gerold, "*Modular Series on Solid State Devices*," Addison-Wesley Publishing Company, vol. I, 1983.
[12] G. N. Tiwari, and S. Dubey, *"Fundamentals of Photovoltaic Modules and Their Applications*," Royal Society of Chemistry, 2009.
[13] L. M. Carrasco, F. J. Martín-Campo, L. Narvarte, M. T. Ortuño, and B. Vitoriano, "Design of Maintenance Structures for Rural Electrification with Solar Home Systems. The Case of the Moroccan Program," *Energy*, vol. 117, pp. 47-57, 2016.
[14] Y. Fan and X. Xia, "A Multi-Objective Optimization Model for Energy-Efficiency Building Envelope Retrofitting Plan with Rooftop PV System Installation and Maintenance," *Applied Energy*, vol. 189, pp. 327-335, 2017.
[15] F. Spertino, and F. Corona, "Monitoring and Checking of Performance in Photovoltaic Plants: A Tool for Design, Installation and Maintenance of Grid-Connected Systems," *Renewable Energy*, vol. 60, pp. 722-732, 2013.
[16] Y. Yu, G. Konstantinou, B. Hredzak, and V. G. Agelidis, "Operation of Cascaded H-Bridge Multilevel Converters for Large-Scale Photovoltaic Power Plants Under Bridge Failures," *IEEE Transactions on Industrial Electronics*, vol. 62, no. 11, pp. 7228-7236, 2015.
[17] X. Hu, and C. Gong, "A High Gain Input-Parallel Output-Series DC/DC Converter with Dual Coupled Inductors," *IEEE Transactions on Power Electronics*, vol. 30, no. 3, pp. 1306-1317, 2014.
[18] M. S. Bhaskar, S. Padmanaban, and F. Blaabjerg, "A Multistage DC-DC Step-Up Self-Balanced and Magnetic Component-Free Converter for Photovoltaic Applications Hardware Implementation," *Energies*, vol. 10, no. 5, 2017.
[19] T. Duman, S. Marti, M. A. Moonem, A. A. R. Abdul Kader, and H. Krishnaswami, "A Modular Multilevel Converter with Power Mismatch Control for Grid-Connected Photovoltaic Systems," *Energies*, vol. 10, no. 5, 2017.
[20] D. Zhao, M. Qian, J. Ma, and K. Yamashita, "Photovoltaic generator model for power system dynamic studies," *Solar Energy*, vol. 210, pp. 101-114, 2020.
[21] H. Meng, X. Ye, et al., "Equivalent Modeling and Simulation for PV System on Dynamic Clustering Equivalent Strategy," *IECON 2017-43rd Annual Conference of the IEEE Industrial Electronics Society*, pp. 5779-5784, 2017.

[22] S. M. MacAlpine, "Characterization and Capture of Photovoltaic System Losses Due to Nonuniform Conditions," Doctoral dissertation, University of Colorado at Boulder, 2014.
[23] M. Hejri, H. Mokhtari, M. R. Azizian, M. Ghandhari, and L. Söder, "On the Parameter Extraction of a Five-Parameter Double-Diode Model of Photovoltaic Cells and Modules," *IEEE Journal of Photovoltaics*, vol. 4, no. 3, pp. 915-923, 2014.
[24] D. L. King, J. A. Kratochvil, and W. E. Boyson, "Photovoltaic Array Performance Model," United States. Department of Energy, 2004, Vol. 8, pp. 1-19.
[25] A. Y. Abdelaziz, and Y. Almoataz, *Modern Maximum Power Point Tracking Techniques for Photovoltaic Energy Systems*. Springer Nature Switzerland AG, 2020.
[26] K. Ishaque, and Z. Salam, "A Review of Maximum Power Point Tracking Techniques of PV System for Uniform Insolation and Partial Shading Condition," *Renewable and Sustainable Energy Reviews*, vol. 19, pp. 475-488, 2013.
[27] B. Nayak, A. Mohapatra, and K. B. Mohanty, "Selection Criteria of DC-DC Converter and Control Variable for MPPT of PV System Utilized in Heating and Cooking Applications," *Cogent Engineering*, vol. 4, no. 1, p. 1363357, 2017.
[28] J. M. Enrique, E. Duran, M. Sidrach-de-Cardona, and J. M. Andujar, "Theoretical Assessment of the Maximum Power Point Tracking Efficiency of Photovoltaic Facilities with Different Converter Topologies," *Solar Energy*, vol. 81, no. 1, pp. 31-38, 2007.
[29] K. Dubey, and M. T. Shah, "Design and Simulation of Solar PV System," *2016 International Conference on Automatic Control and Dynamic Optimization Techniques (ICACDOT)*, pp. 568-573, IEEE, 2016.
[30] N. Chatrenour, H. Razmi, and H. Doagou-Mojarrad, "Improved Double Integral Sliding Mode MPPT Controller-Based Parameter Estimation for a Stand-Alone Photovoltaic System," *Energy Conversion and Management*, vol. 139, pp. 97-109, 2017.
[31] R. Ayop, and C. W. Tan, "Design of Boost Converter Based on Maximum Power Point Resistance for Photovoltaic Applications," *Solar Energy*, vol. 160, pp. 322-335, 2018.
[32] A. Dehghanzadeh, G. Farahani, H. Vahedi, and K. Al-Haddad, "Model Predictive Control Design for DC-DC Converters Applied to a Photovoltaic System," *International Journal of Electrical Power & Energy Systems*, vol. 103, pp. 537-544, 2018.
[33] E. Irmak, and N. Güler, "A Model Predictive Control-Based Hybrid MPPT Method for Boost Converters," *International Journal of Electronics*, vol. 107, no. 1, pp. 1-16, 2019.
[34] M. Mosa, H. A. Rub, M. E. Ahmed, and J. Rodriguez, "Modified MPPT with Using Model Predictive Control for Multilevel Boost Converter," *IECON 2012-38th Annual Conference on IEEE Industrial Electronics Society*, IEEE, pp. 5080-5085, 2012.
[35] M. Metry, S. Bayhan, M. B. Shadmand, R. S. Balog, and H. A. Rub, "Sensorless Current Model Predictive Control for Maximum Power Point Tracking of Single-Phase Submultilevel Inverter for Photovoltaic Systems," *Energy Conversion Congress and Exposition (ECCE)*, pp. 1-8, IEEE, 2016.
[36] M. Abedini, R. Eskandari, J. Ebrahimi, M. H. Zeinali, and A. Alahyari, "Optimal Placement of Power Switches on Malayer Practical Feeder to Improve System Reliability Using Hybrid Particle Swarm Optimization with Sinusoidal and Cosine Acceleration Coefficients," *Computational Intelligence in Electrical Engineering*, vol. 11, no. 2, pp.73-86, 2020.
[37] E. Chegeni, M. Zandieh, and J. Ebrahimi, "Attitude Control of Satellite with Pulse-Width Pulse-Frequency (PWPF) Modulator Using Generalized Incremental Predictive Control," *Majlesi Journal of Electrical Engineering*, vol. 8, no. 3, pp. 25-31, 2014.
[38] H. Makvandi, M. Abasi, et al., "Design of an Optimal STATCOM Controller to Enhance Dynamic Stability of the Smart Grid," *27th International Electrical Power Distribution Networks Conference (EPDC)*, pp. 94-101, IEEE, 2023.
[39] H. Makvandi, M. Abasi, et al., "Design of New Intelligent Islanding Detection Scheme in Multi-Machine Power Systems to Prevent Wide-Area Blackouts," *12th Smart Grid Conference (SGC)*, pp. 1-7, IEEE, 2022.

Declaration of Competing Interest

The authors declare that they have no known competing financial interests or personal relationships that could have appeared to influence the work reported in this paper. The ethical issues, including plagiarism, informed consent, misconduct, data fabrication and/or falsification, double publication and/or submission, redundancy, have been completely observed by the authors.

Credit Authorship Contribution Statement

Moaiad Mohseni: Conceptualization, Formal analysis, Project administration, Supervision, Validation, Roles/Writing - original draft. **Alireza Niknam Kumleh:** Conceptualization, Investigation, Methodology, Resources, Visualization, Writing - review & editing. **Mehdi Alibakhshi**: Methodology, Resources, Software, Supervision, Validation. **Mona Sheikhi Abou Masoudi:** Funding acquisition, Investigation, Writing-review & editing.

Bibliography

Moaiad Mohseni was born in Kwait. He received his B.SC Degree in Electrical Engineering, Kazeroon Branch, Islamic Azad University, Kazeroon, Iran in 2001, and his M.S. and Ph.D. degrees in Electrical Engineering from Dezful Branch, Islamic Azad University, Dezful, Iran, in 2011and 2021, respectively. His Research Include Power Market and Smart Grid and renewable energy systems.

Alireza Niknam Kumleh was born in Tehran. He received his B.SC Degree in Electrical Engineering, Faculty of Electrical Engineering, Amirkabir University of Technology (Tehran polytechnic), Tehran, Iran in 2012, and his M.S. degrees in Electrical Engineering from Faculty of Electrical Engineering, Amirkabir University of Technology (Tehran polytechnic), Tehran, Iran in 2015, respectively. His Research Include Power Market, Smart Grid, renewable energy systems.

Mehdi Alibakhshi was born in Iran in 1985. He received his Master degree in control engineering from south Tehran Branch, Islamic Azad University, Tehran, Iran, in 2011. He currently works as a researcher. Also, he has taught for ten years at Borujerd Islamic Azad University. he has published one research papers, one conference papers. His research interests include power electronic, predictive control, and microgrids.

Mona Sheikhi Abou Masoudi was born in Iran in 1986. She received his Master degree in Electronic Engineering from Oloom Tahghighat Branch, Islamic Azad University, Tehran, Iran, in 2011. She currently works as a teacher in Naghshe Jahan institute. Also, she has taught for ten years at Sepahan and Safahan and Kharazmi university. She has published two research papers, one conference papers. Her research interests include power electronic, control, and microgrids.